

MICROCOPY RESOLUTION TEST CHART
NATIONAL BUREAU OF STANDARDS-1963-A

12

DTIC FILE COPY

DNA-TR-86-309

FLOW-FIELD INSTRUMENTATION DEVELOPMENT

AD-A182 620

A. A. Burns
SRI International
333 Ravenswood Avenue
Menlo Park, CA 94025-3434

30 August 1986

Technical Report

CONTRACT No. DNA 001-84-C-0439

Approved for public release;
distribution is unlimited.

THIS WORK WAS SPONSORED BY THE DEFENSE NUCLEAR AGENCY
UNDER RDT&E RMSS CODE X342084469 Q93QMXAG00038 H2590D.

Prepared for
Director
DEFENSE NUCLEAR AGENCY
Washington, DC 20305-1000

DTIC
ELECTE
JUL 07 1987
S E D

Destroy this report when it is no longer needed. Do not return to sender.

PLEASE NOTIFY THE DEFENSE NUCLEAR AGENCY
ATTN: TITL, WASHINGTON, DC 20305 1000, IF YOUR
ADDRESS IS INCORRECT, IF YOU WISH IT DELETED
FROM THE DISTRIBUTION LIST, OR IF THE ADDRESSEE
IS NO LONGER EMPLOYED BY YOUR ORGANIZATION.



UNCLASSIFIED

AD-A182620

SECURITY CLASSIFICATION OF THIS PAGE

REPORT DOCUMENTATION PAGE

1a. REPORT SECURITY CLASSIFICATION UNCLASSIFIED		1b. RESTRICTIVE MARKINGS	
2a. SECURITY CLASSIFICATION AUTHORITY N/A since UNCLASSIFIED		3. DISTRIBUTION/AVAILABILITY OF REPORT Approved for public release; distribution is unlimited.	
2b. DECLASSIFICATION/DOWNGRADING SCHEDULE N/A since UNCLASSIFIED			
4. PERFORMING ORGANIZATION REPORT NUMBER(S) SRI Project 7933		5. MONITORING ORGANIZATION REPORT NUMBER(S) DNA-TR-86-309	
6a. NAME OF PERFORMING ORGANIZATION SRI International	6b. OFFICE SYMBOL <i>(if applicable)</i>	7a. NAME OF MONITORING ORGANIZATION Director Defense Nuclear Agency	
6c. ADDRESS (City, State, and ZIP Code) 333 Ravenswood Avenue Menlo Park, CA 94025-3434		7b. ADDRESS (City, State, and ZIP Code) Washington, DC 20305-1000	
8a. NAME OF FUNDING/SPONSORING ORGANIZATION	8b. OFFICE SYMBOL <i>(if applicable)</i> SPAS/Rohr	9. PROCUREMENT INSTRUMENT IDENTIFICATION NUMBER DNA 001-84-C-0439	
8c. ADDRESS (City, State, and ZIP Code)		10. SOURCE OF FUNDING NUMBERS	
		PROGRAM ELEMENT NO. 62715H	PROJECT NO. Q93QMXA
		TASK NO. G	WORK UNIT ACCESSION NO. DH251235
11. TITLE (Include Security Classification) FLOW-FIELD INSTRUMENTATION DEVELOPMENT			
12. PERSONAL AUTHOR(S) Burns, Alan A.			
13a. TYPE OF REPORT Technical	13b. TIME COVERED FROM 840926 TO 860830	14. DATE OF REPORT (Year Month, Day) 860830	15. PAGE COUNT 142
16. SUPPLEMENTARY NOTATION This work was sponsored by the Defense Nuclear Agency under RDT&E RMSS Code X342084469 Q93QMXAG00038 H2590D.			
17. COSATI CODES			18. SUBJECT TERMS (Continue on reverse if necessary and identify by block number) Shock-Wave Phenomenology Millimeter-Wave rf Measurements
FIELD	GROUP	SUB-GROUP	
14	2		
18	3		
19. ABSTRACT (Continue on reverse if necessary and identify by block number) Equipment was assembled to make two new types of measurements of quantities important for describing shock-wave effects in a dusty environment. The first of these employs a novel technique combining millimeter-wave (mmW) rf phase shift and X-ray absorption measurements to obtain fluctuations in air and dust densities in the shock wave. Use of either an X-ray or rf technique above leads only to a weighted sum of air and dust densities. The second new technique uses the reflection of microwave signals from the bottom-side of the soil surface to measure surface recession because of shock-wave passage. This technique exploits the phenomenon of total internal reflection at a material interface. Two short series of equipment shakedown tests were performed in the CERF/NMERI 6-ft shock tube. This report describes the techniques, the equipment, calibration, test results, problems encountered, and corrective actions. Results from the installation of the mmW/X-ray equipment at MINOR SCALE are described			
20. DISTRIBUTION/AVAILABILITY OF ABSTRACT <input type="checkbox"/> UNCLASSIFIED/UNLIMITED <input checked="" type="checkbox"/> SAME AS RPT <input type="checkbox"/> DTIC USERS		21. ABSTRACT SECURITY CLASSIFICATION UNCLASSIFIED	
22a. NAME OF RESPONSIBLE INDIVIDUAL Sandra E. Young		22b. TELEPHONE (Include Area Code) (202) 325-7042	22c. OFFICE SYMBOL DNA/CSTI

DD FORM 1473, 84 MAR

83 APR edition may be used until exhausted
All other editions are obsolete

SECURITY CLASSIFICATION OF THIS PAGE

UNCLASSIFIED

UNCLASSIFIED

SECURITY CLASSIFICATION OF THIS PAGE

18. SUBJECT TERMS (Continued)

X-ray Absorption Measurements
Surface Recession Microwave Measurements
Shock-Tube Phenomenology
Air- and Dust-Density Fluctuations

19. ABSTRACT (Continued)

in an Appendix; these are believed to be the first reported simultaneous measurements of air- and dust-density in a shock front.

SECURITY CLASSIFICATION OF THIS PAGE

UNCLASSIFIED

PREFACE

The instrumentation development and analytical research described in this report would not have been possible without the cooperation of the Civil Engineering Research Facility/New Mexico Engineering Research Institute (CERF/NMERI) personnel at their shock-tube facility at Kirtland Air Force Base. In particular, we gratefully acknowledge the generous and diligent support from the following people: Leo Stockham, for overall managerial organization; Daniel Becker, for efficient test operations; and James Nicholson and his crew, for cheerfully helping us solve a variety of problems on a daily basis.

Accession For	
NTIS CRA&I	<input checked="" type="checkbox"/>
DTIC TAB	<input type="checkbox"/>
Unannounced	<input type="checkbox"/>
Justification	
By _____	
Distribution/	
Availability Codes	
Dist	Avail and/or Special
A-1	



TABLE OF CONTENTS

Section	Page
PREFACE.	111
LIST OF ILLUSTRATIONS.	vi
LIST OF TABLES	ix
1. INTRODUCTION	1
1.1 OBJECTIVES.	1
1.2 BACKGROUND.	2
1.2.1 Historical Background.	2
1.2.2 Current Picture of Dust-Loaded Complex Mach Structure	5
1.2.3 Background on Diagnostics.	6
1.2.3.1 Air and Dust Densities	6
1.2.3.2 Microwave Surface Recession.	7
2. X-RAY/mmW AVERAGE AIR- AND DUST-DENSITY MEASUREMENTS . .	9
2.1 DESCRIPTION	9
2.2 MEASUREMENT BASIS	9
2.2.1 X-Ray Absorption.	9
2.2.2 mmW Phase Shift.	17
2.2.2.1 Gas (Air) Contribution	19
2.2.2.2 Dust Contribution.	21
2.3 COMBINED MEASUREMENTS	22
2.4 SOURCES OF EXPERIMENTAL ERROR	24
2.5 CALIBRATION	29
2.5.1 mmW Phase Shift Caused by Air (f).	30
2.5.2 mmW Phase Shift Caused by Dust (g)	30
2.5.3 X-Ray Absorption by Air.	32
2.5.4 X-Ray Absorption by Soil	36
2.5.5 Calibration and Accuracy Requirements.	37

Section	Page
3. MICROWAVE SURFACE-RECESSION MEASUREMENT.	42
3.1 INTRODUCTION.	42
3.2 BASIS	42
3.2.1 Total Internal Reflection.	42
3.2.2 Refractive Reflection from a Density Gradient	45
4. DESCRIPTION OF EQUIPMENT	50
4.1 X-RAY/mmW SYSTEM.	50
4.2 SURFACE-RECESSION SYSTEM.	53
4.3 DATA-ACQUISITION SYSTEM	53
5. FIELD TESTS AT THE 6-FT SHOCK TUBE	56
5.1 EQUIPMENT INSTALLATION.	56
5.2 EQUIPMENT AND EXPERIMENT PROBLEMS	62
5.3 TEST SUMMARIES.	64
5.4 EXAMPLES OF DATA.	67
5.4.1 X-Ray/mmW.	67
5.4.1.1 No Helium (Precursor) Layer Tests.	67
5.4.1.2 Tests with a Helium Layer (Precursed).	80
5.4.1.3 Late-Time Behavior	85
5.4.1.4 Air- and Dust-Density Estimation	85
5.4.2 Surface Recession.	91
6. CONCLUSIONS AND RECOMMENDATIONS.	101
7. LIST OF REFERENCES	104
 Appendices	
A True-Height Analysis.	105
B MINOR SCALE Fielding.	109

LIST OF ILLUSTRATIONS

Figure		Page
1	Schematic representation of dust-loaded complex Mach structure.	4
2	Mass absorption coefficient vs X-ray energy for silicon dioxide and air	10
3	The continuous X-ray spectrum from a tungsten target showing the dependence of the short wavelength limit on the voltage across the tube.	12
4	X-ray photon energy at peak emission for tungsten vs tube voltage.	13
5	Spectra of 45-keV tungsten X-ray photons after penetrating air	14
6	Photon counting rate vs thickness	16
7	Refraction effect	26
8	Example of refractive binding	27
9	X-ray calibration results for air	33
10	Mass absorption coefficient vs photon energy for air.	35
11	X-ray soil calibration.	36
12	X-ray absorption vs mmW phase compared to the theoretical slope $G/(kg)$	40
13	Total internal reflection surface recession measurement	43
14	Total internal reflection parameters.	44
15	Refractive reflection with a density gradient	45
16	Incidence angle vs density to satisfy reflection condition	47
17	Block diagram of X-ray/mmW-density-measurement system.	51
18	SRI International mm-band rf diagram.	52
19	Block diagram of microwave surface recession system	54
20	mmW/X-ray installation in a 6-ft shock tube	57
21	External view of the X-ray/mmW experiment installation.	58
22	View from inside the shock tube of the X-ray/mmW ports and installation.	59

Figure		Page
23	Cross section of surface-recessive installation in the 6-ft shock tube.	61
24	X-ray digitizer output vs time for HST 142.	68
25	X-ray digitizer output vs time after T_0 for HST 142	69
26	Processed X-ray data (absorption) vs time after T_0 for HST 142	70
27	mmW phase and amplitude vs time after T_0 for HST 142	71
28	X-ray digitizer output vs time for HST 131.	72
29	X-ray absorption and mmW phase vs time after T_0 HST 131	73
30	X-ray digitizer output vs time for HST 144.	74
31	X-ray absorption and mmW phase vs time after T_0 for HST 144	75
32	Receiver accelerometer data for HST 142	76
33	Doubly integrated accelerometer data from HST 142	77
34	Phase vs time for HST 142	78
35	HST 142 receiver antenna displacement computed from accelerator data.	79
36	X-ray digitizer output vs time for HST 141.	80
37	X-ray absorption and mmW phase vs time for HST 141.	81
38	X-ray digitizer output vs time for HST 143.	82
39	X-ray absorption and mmW phase vs time after T_0 for HST 143	83
40	Late-time X-ray absorption for HST 142.	86
41	Late-time X-ray absorption for HST 143.	87
42	Relative estimates of air and dust densities for HST 142	88
43	Static overpressure measured at HST 142	89
44	Sum of relative estimates of air and dust densities for HST 142	90
45	HST 143 amplitude and pulse records	92
46	HST 144 amplitude and phase records	95
47	HST 144 Path 1 phase and amplitude records.	98

Figure		Page
48	mmW/X-ray transmission experiment for MINOR SCALE . . .	111
49	MINOR SCALE mmW phase and amplitude records	113
50	Long-term mmW phase and amplitude records	115
51	X-ray detector output	119
52	Regression analysis of phase vs amplitude	122
53	Dust and relative air-density estimates	123

LIST OF TABLES

Table		Page
1	Atmospheric quantities and mmW calibration factor. . . .	31
2	Summary of dielectric measurements of shock-tube samples.	32
3	mmW and X-ray calibration factors.	38
4	Antenna positions and specular reflection angles	62
5	Analysis of pre- to post-shot X-ray absorption changes for tests with a helium precursor.	84

SECTION 1

INTRODUCTION

1.1 OBJECTIVES.

The objectives of this work were to develop two types of diagnostic instrumentation for measuring mean (i.e., spatially averaged) air and dust densities, and for measuring surface recession and mass scouring during shock-wave passage in precursed and unprecursed dusty flows. The approach used in the first type of measurement is a combination of X-ray absorption/millimeter-wavelength (mmW) rf phase-shift techniques. This combination exploits the differences between air and dust sensitivities of X-ray absorption and mmW phase shift to separate air and dust fluctuations. A single measurement of either X-ray absorption or mmW phase shift will produce an ambiguous result because air and dust sensitivities are of similar magnitude. That is, with a single type of measurement alone, we cannot be sure whether observed changes are produced by variations in dust density, air density, or some combination of the two.

The surface recession technique is based upon total internal reflection of microwave (X-band) signals propagating for short distances underground and reflecting from the underside of the surface. Because no part of the equipment used in the experiment protrudes through the surface, this technique avoids any problems caused by intrusive techniques in which the presence of a vertical structure passing through the surface can affect soil response at that boundary. In addition, because the phases of the rf signals reflected from the underside of the soil surface are measured, it is theoretically possible to separate mass loss from mere compression of the surface.

Under this contract (DNA 001-84-C-0439), equipment was assembled and then tested during a pair of short series of shots at the CERF/NMERI 6-ft shock tube at Kirtland Air Force Base, New Mexico. [The X-ray/mmW equipment was also fielded for the MINOR SCALE HE test under a separate contract (DNA 001-85-C-0301) during this time.] In this report, we describe the physical bases for the measurement techniques, the equipment assembled, calibration, and the results of the initial testing. This testing revealed that a small amount of further development is needed to eliminate several mechanical problems.

1.2 BACKGROUND.

This section contains a description of the historical development of the understanding of the complex Mach structure and dust pedestal. This is followed by a short description of the precursed, complex Mach structure.

1.2.1 Historical Background.

In the early 1950s, atmospheric nuclear tests at the Nevada Test Site (NTS) revealed the production of the dust pedestal following height-of-burst (HOB) detonations. Although a simple Mach stem had been predicted even before the TRINITY event in 1944, the dust pedestal clearly required more complex flows than could be expected from a simple Mach stem. Thermal radiation interacted with the ground surface to produce a thin layer of heated air adjacent to the ground. Its existence was revealed through the development of a "precursor" wave--a diagonal shock wave extending forward of the vertical Mach stem. Overpressure and dynamic-pressure measurements also revealed that these could be severely altered in the presence of a heavy dust pedestal.

The GRABLE event [UPSHOT KNOTHOLE-#10-1953-15 KT at a scaled height of burst (SHOB) of $205 \text{ ft/KT}^{1/3}$] revealed that a smoke screen shielding the desert surface from thermal radiation would prevent the production of a thermal precursor--and heavy dusting. It became clear then that heavy dusting and concomitant important changes in

overpressure and dynamic pressure required that (1) dust be available for lofting outward from the point where a Mach stem forms, and (2) that nuclear thermal radiation produce the surface layer of heated air in which the precursor wave travels.

Further tests were made on the MET event. The MET detonation [TEAPOT #12-1955-22 KT at a SHOB of $138 \text{ ft/KT}^{1/3}$] was instrumented using GREG and SNOB gauges along three prepared-surface radials. These were a desert radial, a water radial (probably uncontrolled water here, mud there), and an asphalt-covered radial. Observations along these radials revealed that shock arrival times were 16 percent earlier over the asphalt surface than over a desert radial, indicating a slower velocity across the desert surface. Pressure-wave measurements along the asphalt surface showed a strong precursor because the bomb's thermal energy heated the asphalt, which in turn heated the boundary layer air. The overpressure and dynamic pressures were nearly normal.

The dusty radial (normal desert surface) showed decreases in overpressure and increases in and complex behavior of the dynamic pressure. The behavior over the water/mud surface was more nearly like that expected for an ideal surface. Measurements of the characteristics of the thermal layer were made using acoustic propagation and thermal couplers. Surprisingly high air temperatures were measured, supporting the concept of a low, thermal layer being responsible for the observed precursor.

Dust density was measured on event MET by Baumeister and Shelton of Sandia and Gordon of the Army Chemical Center. Although they derived somewhat different answers, the measurements implied very high dust densities--perhaps several times the density of ambient air.

Considerable data on overpressure and dynamic pressure versus time and distance from 21 NTS and 4 PPG tests were obtained. These showed a number of different forms. Because atmospheric testing ceased in 1962, these data have been extensively studied. A rather elaborate system of classification of them was developed.

The 1981 MIGHTY MACH HE experiments in Canada involved HOB tests using 100-lb HE detonations; excellent overpressure and photographic diagnostics revealed the complexity of the Mach stem structure. The tests showed that addition of dust (glass beads in this experiment) further complicated the structure and supported conjectures concerning the data from the full-scale nuclear tests. The realization now is that a reverse vortex develops as a result of the precursor and complex Mach structure; this vortex flows outward with the shock structure. Figure 1 is a schematic representation copied from a 1981 figure by Dr. George Ullrich (personal communication^{1*}) of DNA.

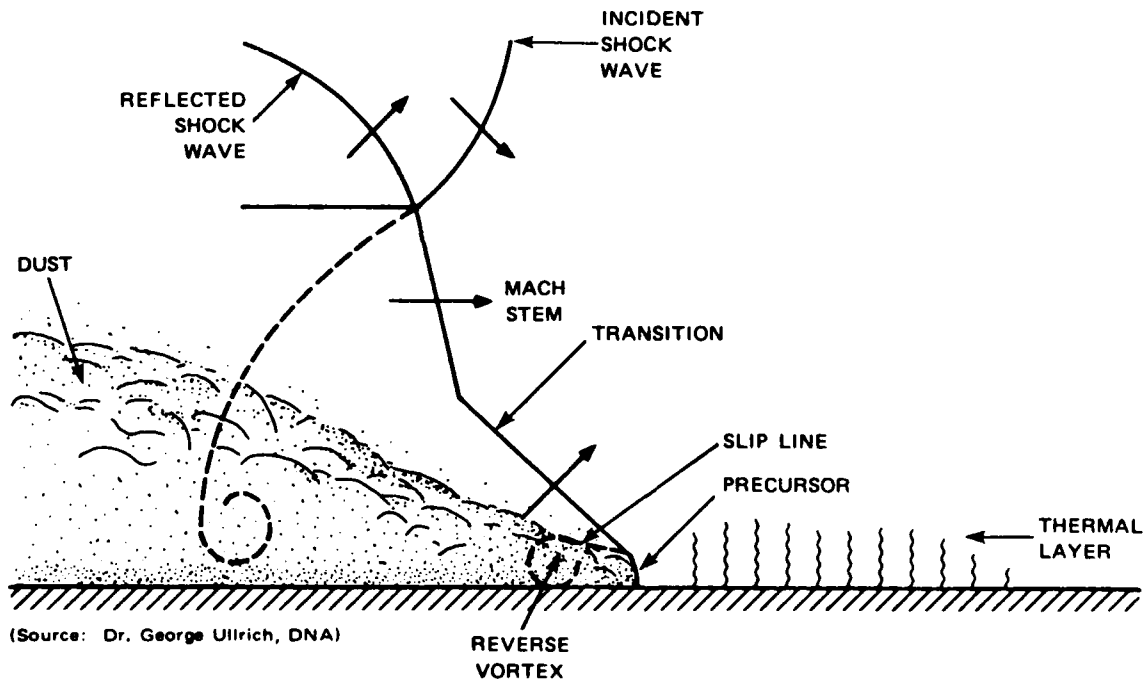


Figure 1. Schematic representation of dust-loaded complex Mach structure. Vorticity produced by slip lines behind precursor provides a means for vertical transport of dust scoured from surface.

* References are listed at the end of this report.

The importance of these revelations was threefold. First, the diagnostics showed that the presence of heavy dust loading was accompanied by an extreme increase in complexity of shock structure and supported the various classification concepts from nuclear tests in the 1950s. The observations supported the supposition that the change in dynamic pressure and the production of multiple peaks and fluctuating temporal components were due to the introduction of additional mass into the flow.

Second, the reverse vortex meant that the surface flow responsible for dust scouring was not "subsonic," estimated earlier by the Rankine-Hugoniot relations, as might be naively (now) believed. Rather, the boundary layer flow was nearly twice that of the local Mach stem velocity which is, at times, extremely supersonic. Because surface scouring is proportional to a high power of velocity, a mechanism is available that can plausibly explain the very high dust densities inferred from NTS data from the 1950s.

Surface scouring, saltation, "popcorning," and reverse percolation ("pore air ejection") have all been candidates to explain ejection of dust upwards from the earth's surface. It had been assumed that further rise in the dust pedestal resulted from turbulent diffusion. However, the reverse-vortex not only leads to extreme scouring, negating the need for dependence on the other phenomena, but the vortex itself provides a larger scale, coherent, hydrodynamic flow pattern that lofts the dust upwards very rapidly. This is the third revelation of this recent DNA work. This result is consistent with the nature and magnitude of dust rise velocity as measured from the Event GRABLE dust pedestal as reported in a presentation by Dr. W. G. Chesnut in a July 1981 DNA Effects Symposium.

1.2.2 Current Picture of Dust-Loaded Complex Mach Structure.

Figure 1 only portrays the dust-loaded, precursed, complex Mach structure schematically. The diagram shows the simple Mach stem resulting from the coalescence of the incident and reflected shock

waves. Not shown in our diagram is an example of the complex array of shock waves behind the triple point (stem and shock-wave intersections)--principally, because we do not have an appropriate example. In front of the moving Mach structure is a portrayal of the thermal layer in which the precursor travels--that may be simulated by a trapped, helium layer in the HML tests. This thermal layer is currently modeled for use in the Hull code as though the air is heated by thermal conduction from the intensely hot ground surface. The precursed shock wave, traveling next to the surface, connects to the Mach stem by a transition shock as shown in the diagram. Two slip lines are shown producing reverse vortices. Schematic representation of dust rise is shown.

Photographs obtained overhead using the SRI aircraft on the recent DIRECT COURSE HOB-HE test reveal that the dust pedestal is a ring of lofted dust around ground zero, not a "table" as our diagram implies.² This photographic result confirms inferences drawn from the photographs of MIGHTY MACH (1000-lb HOB-HE tests mentioned earlier) and GRABLE (HOB-Nuclear).

1.2.3 Background on Diagnostics.

1.2.3.1 Air and Dust Densities--rf phase measurements as a diagnostic of dust density were first made on the 1976 DICE THROW event.³ Measurements were made at frequencies between 400 MHz over many different paths. The data permitted estimating integrated dielectric changes along a propagation path that could be due to dust, hot air, or high-explosive products. The data have also been used to simulate radar tracking problems should monopulse radars immersed in a dust pedestal need to track reentry vehicles (the LOADS, 1981 problem). Subsequently, dust density was measured on the MISERS BLUFF, MILL RACE, and DIRECT COURSE experiments.⁴ In these experiments, which were intended to address intermediate-to-late-term dust issues, the air density along the propagation paths was known (i.e., had returned to ambient) so that

inferring dust density from the measurement was not particularly ambiguous.

The characteristics of the shock structure in the HML test simulator requires measurements of dust density and air density. The rf phase diagnostic permits determining of integrated phase path variations, be they due to dust or air, or a combination of variations in either. In order to measure the two separately, we need to employ a second diagnostic. It needs to be sensitive to air or the dust or to the two combined in a different manner than is rf phase. In combination with the rf phase measurement, the two diagnostics allow separation of the two separate densities.

Low-energy X rays in the range of 20 to 80 keV hold the promise of being the adjunct, simultaneous other diagnostic. X-ray absorption measurements respond to air and dust differently than do rf phase changes. Thus, measurements of both rf and X rays propagated along a common or contiguous path, in principle, permit the simultaneous but separate determination of air and dust density.

TRW has made innovative dusty-flow field measurements using X rays alone that provide vertical profiles of absorption. These profiles have been interpreted in terms of variations in dust density by assuming that air-density fluctuations produce negligible changes in X-ray absorption. The X-ray/mmW measurements approach described here differs from the TRW approach in two important respects:

- (1) Air and dust density are estimated separately
- (2) Longer path lengths are used to obtain spatially averaged values for air and dust densities along the shock front.

The two types of measurement, therefore, complement one another.

1.2.3.2 Microwave Surface Recession--To our knowledge, this is the first attempt to measure surface changes using microwave energy propagating through the soil and undergoing total internal reflection from the bottom side of the surface. Previously, photographic methods

were used to record the surface response viewed through vertical windows penetrating the surface.

SECTION 2

X-RAY/mmW AVERAGE AIR- AND DUST-DENSITY MEASUREMENTS

2.1 DESCRIPTION.

This is a path-integrated measurement that involves transmitting X rays and a mmW rf signal between two stations separated along a line normal to the direction of the shock wave. One station contains the X-ray source and a horn antenna, and the other station has the X-ray detector plus another horn antenna.

Although the direction of propagation of the mmW signal is irrelevant for that part of the measurement, it was convenient in our implementation to put the transmitting antenna with the X-ray source. The respective antennas were installed as closely as possible to the X-ray source and detector in order to minimize differences because of effects in the paths. In addition, one antenna was installed ahead of the associated X-ray port, and the other behind, so that the X-ray and mmW propagation paths would intersect. The X-ray ports and the antennas were all at the same height above the surface. For testing in the 6-ft shock tube this height was 4 in.

2.2 MEASUREMENT BASIS.

2.2.1 X-Ray Absorption.

X rays traversing air laden with dust will suffer attenuation. For monochromatic X rays, the total absorption coefficient depends linearly upon the mean air density and upon the mean dust density along the propagation path. Figure 2 presents the logarithm of the mass absorption coefficient versus logarithm of X-ray photon energy for air and for silicon dioxide. X-ray absorption coefficients over the illustrated energy region are dominated by two interaction processes:

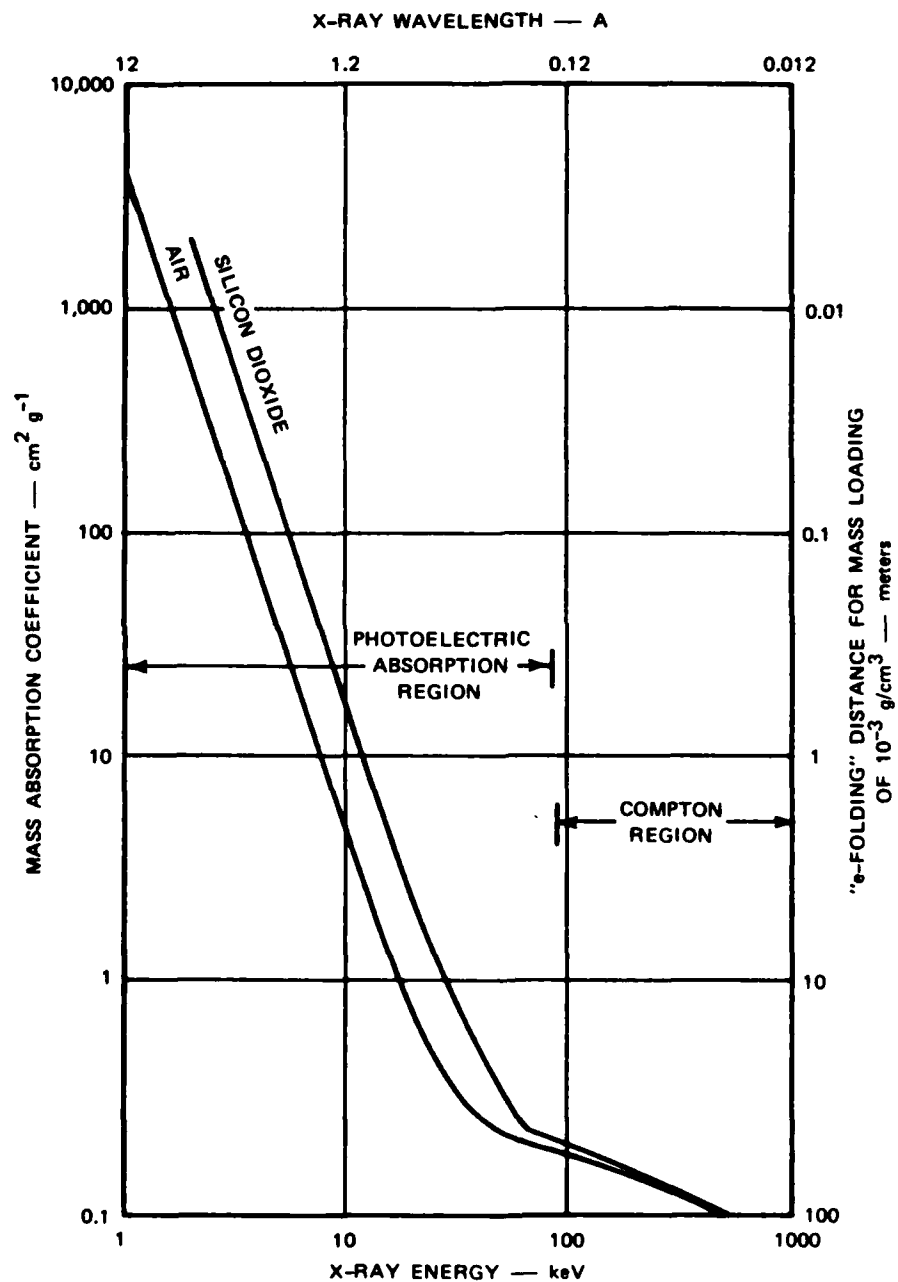


Figure 2. Mass absorption coefficient vs X-ray energy for silicon dioxide and air.

(1) Compton scattering at higher energies and (2) photoelectric absorption at lower energies. These regions are delineated in the figure. The division between the regions is on the order of 80 keV. For low Z materials, the mass absorption coefficient in the Compton region is nearly independent of the material composition. This region is not of interest in this experiment.

In the photoelectric region, the absorption coefficient can be very different for the different materials, e.g., silicon dioxide and air. For this example, in the photoelectric region, the mass absorption coefficient for silicon dioxide is nearly four times that for air. The photoelectric absorption coefficient for almost all soil materials depends upon the inverse cube of the photon energy.

A beam of monochromatic X rays passing through a region of variable air and dust density will produce a flux of photons at the detector given by

$$I = I_0 \exp - \{ [F(\rho_a - \rho_{a0}) + G \rho_d] l \} \quad (1)$$

where

- I = instantaneous X-ray flux rate at detector, photon/s
- I_0 = flux rate when undisturbed air is present, photon/s
- l = path length
- F = mass absorption coefficient for X rays in air, cm^2/g
- ρ_a = instantaneous air density, g/cm^3
- ρ_{a0} = ambient air density, g/cm^3
- G = mass absorption coefficient for X rays in dust, cm^2/g
- ρ_d = instantaneous dust density, g/cm^3 .

To achieve a sufficiently high continuous X-ray flux for this measurement it is necessary to use the continuum (Bremsstrahlung) spectrum from conventional X-ray tubes. Figure 3 presents examples of the spectra from a tungsten-target tube. At 60-kV accelerating voltage, the peak of the Bremsstrahlung radiation spectrum occurs at a photon

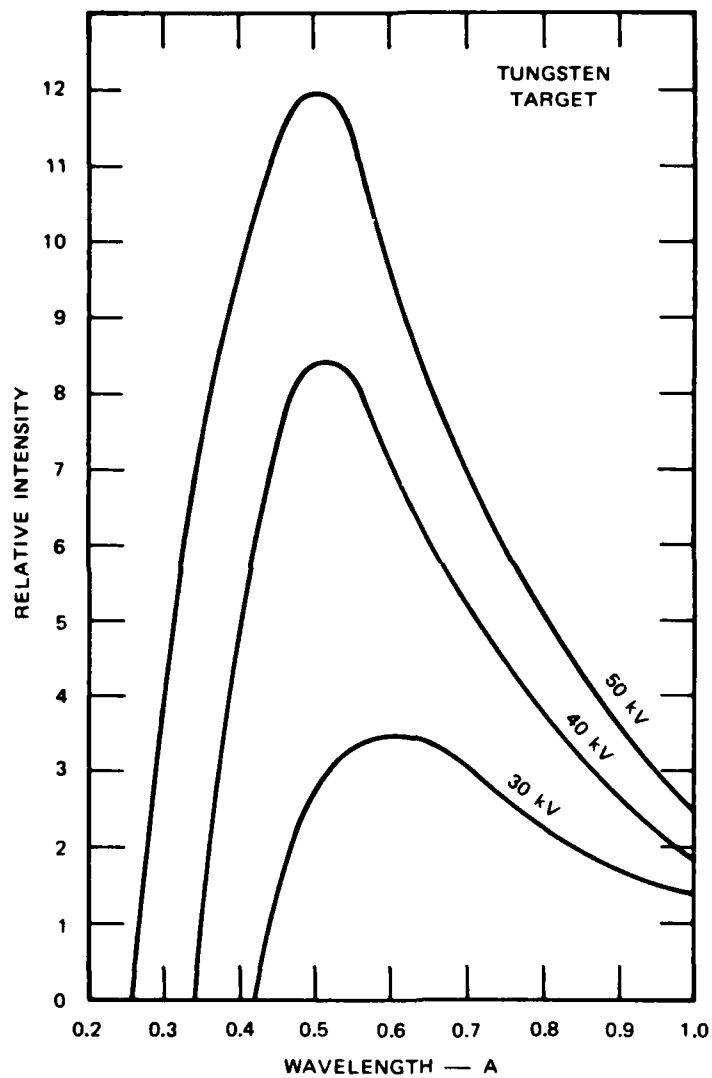


Figure 3. The continuous X-ray spectrum from a tungsten target showing the dependence of the short wavelength limit on the voltage across the tube.

energy roughly half of the maximum energy, which corresponds to the tube voltage. Figure 4 shows a plot of the photon energy at peak emission as a function of accelerating voltage. Although the narrow K-, L-, and M-recombination lines of the X-ray spectra appear at higher voltages, the total energy in them is small to the Bremsstrahlung continuum and will not affect these measurements.

It is evident from Figures 2 and 3 that the X-ray spectrum will be altered by passage through matter. The lower-energy photons are more readily absorbed, so the spectrum narrows and the mean energy increases (i.e., the spectrum is said to "harden"). Figure 5 presents

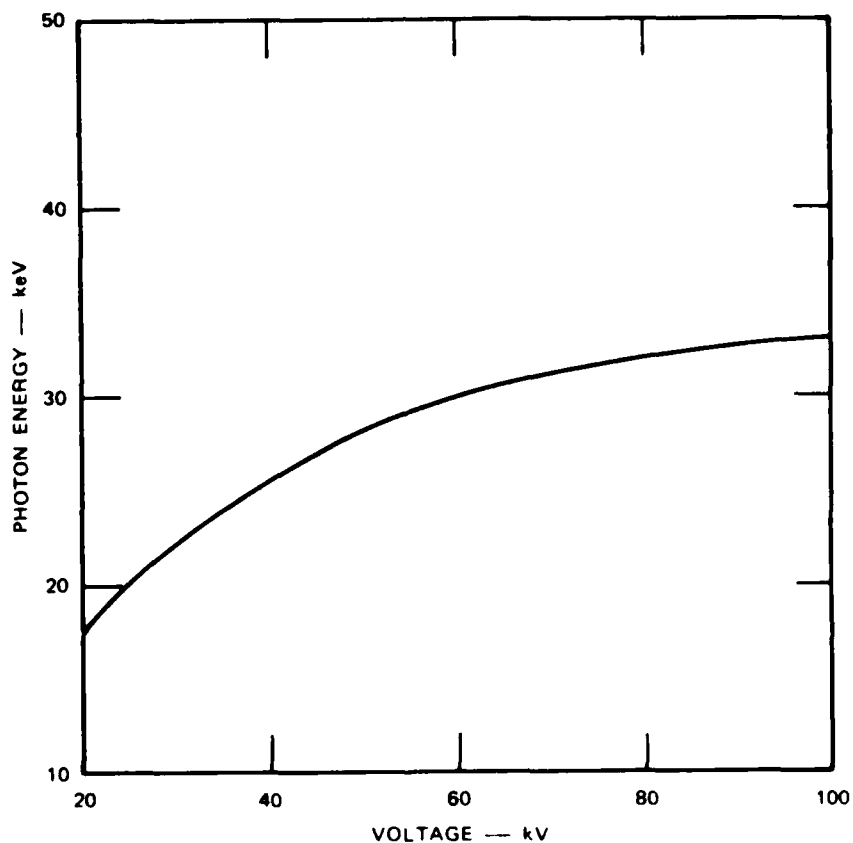


Figure 4. X-ray photon energy at peak emission for tungsten vs tube voltage.

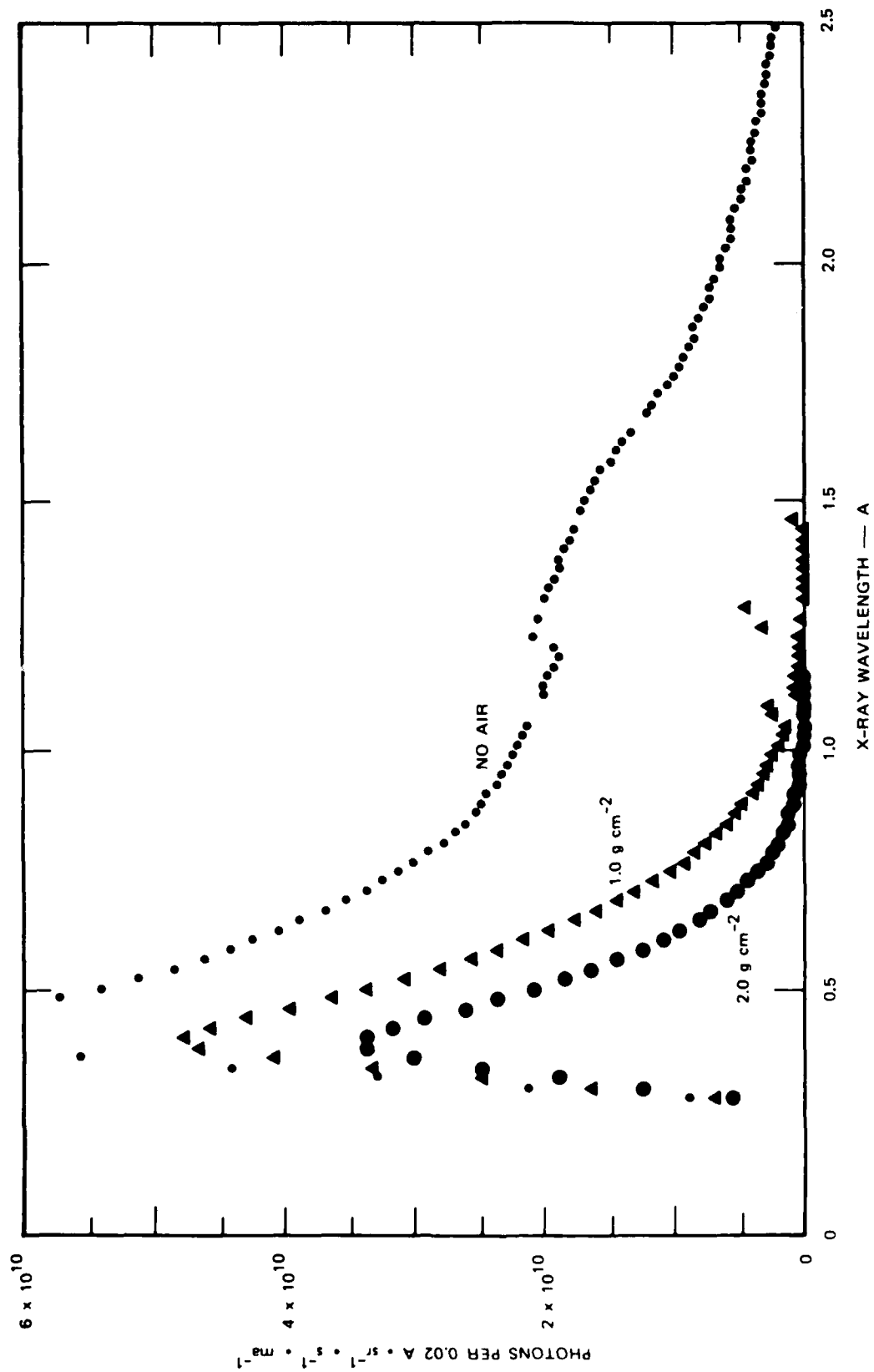


Figure 5. Spectra of 45-keV tungsten X-ray photons after penetrating air.

the results of calculations of the initial Bremsstrahlung spectrum from a 45-kV tungsten-target X-ray source and the spectra after passing through 1 and 2 g/cm² of air. The effect of this spectral hardening is to change the simple exponential relationship implied by Eq. (1).^{*} Figure 6 shows the calculated photon counting rate for different thicknesses of air, SiO₂, and CaSO₄. Only after passage through about 0.5 to 1 g/cm² of material does the spectrum become sufficiently monochromatic to provide a reasonable approximation to Eq. (1).

Experimentally, from the calibration runs (X-ray calibration data are discussed below), we found that Eq. (1) generally applied quite accurately. Evidently, the X-ray spectrum was hardened by the various thicknesses of materials in the windows of the ports into the shock tube and used to protect the detector. The total amount of material added up to about 2.5- to 3-g/cm² thickness. Thus, the X-ray spectrum used for measurements was reasonably monochromatic.

We are thus justified in applying Eq. (1) to approximate the situation for a continuum spectrum. Taking the logarithm, Eq. (1) becomes

$$-\ln \left(\frac{I}{I_0} \right) = F(\rho_a - \rho_{a0}) \ell + G\rho_d \quad . \quad (3)$$

Values for F and G need to be obtained by means of direct calibration. The best way to accomplish this is to insert various thicknesses of material into the beam using the actual experimental setup, to account for the particular configuration of window materials. This could be done easily for dust using various thicknesses of soil

^{*} Equation 1 is replaced by

$$I = \int_{\lambda} I_b(\lambda) \exp - \{ [F(\lambda)\rho_a + G(\lambda)\rho_d] \ell \} d\lambda \quad (2)$$

where λ = X-ray wavelength.

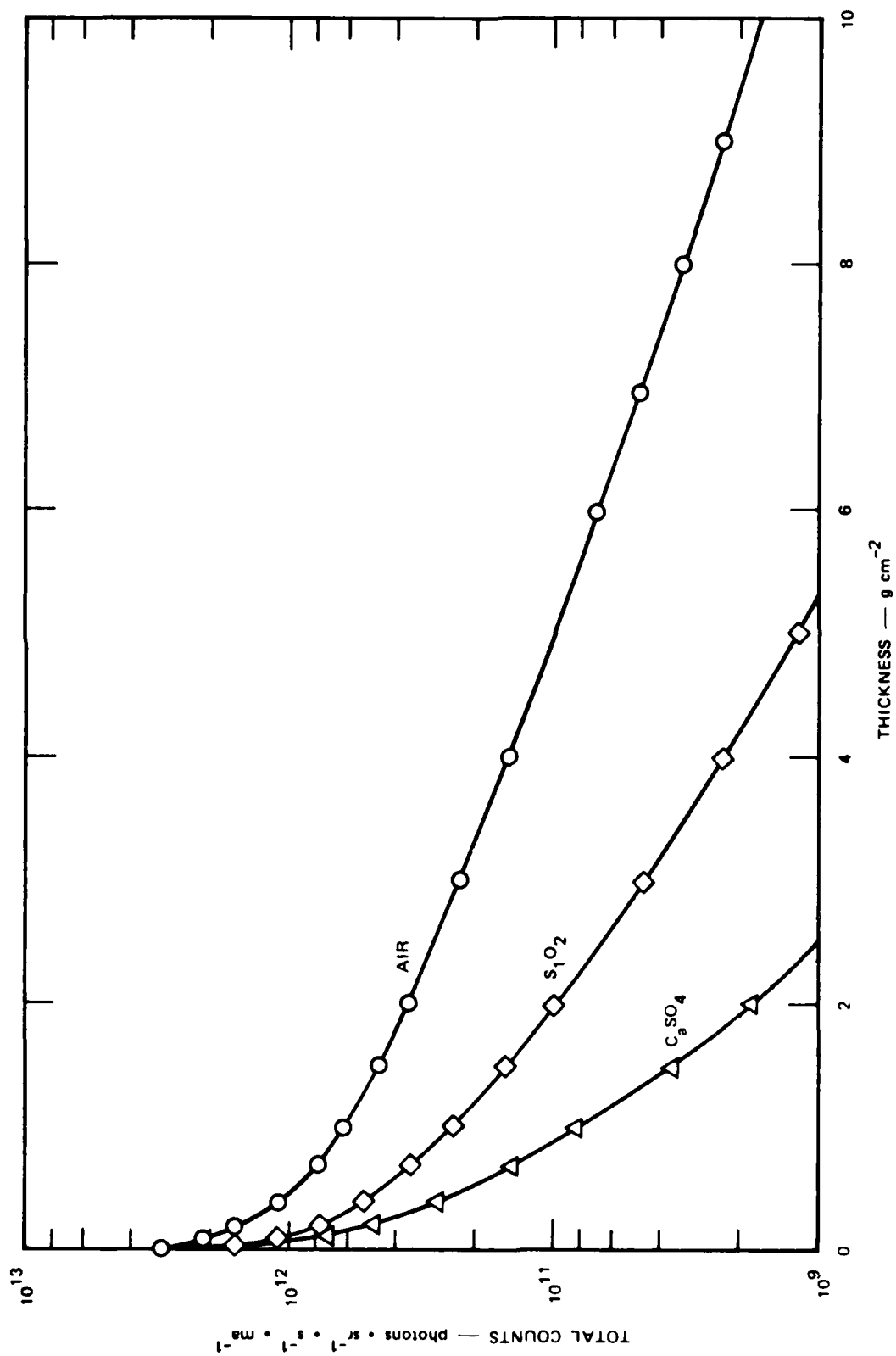


Figure 6. Photon counting rate vs thickness.

samples (it was found that aluminum was a good substitute because it had the same absorption coefficient as the soil and was far easier to handle). Unfortunately, the same window materials could not be used for the air calibration because it required using a long pressurized pipe to change the air density in the beam. For safety reasons, stronger windows were required at the ends of the pressurized pipe.

2.2.2 mmW Phase Shift.

The other half of the measurement employs the rf phase-shift method. This involves placing a transmitting antenna at one station and a receiving antenna at the other then sending a continuous-wave (CW) signal between them. The arrangement is analogous to a Mach-Zender interferometer. The equipment is arranged to measure the rf phase difference between the signal passed along one arm through the dusty flow between the antennas and another arm (a cable) unaffected by the flow. In principle, it is also possible to increase rf attenuation, but that quantity is very difficult to calibrate and is small for the short path lengths used. Millimeter-wavelength signals were chosen to maximize the sensitivity of the measurement and its spatial resolution.

Variations in dust loading and air density produce changes in mmW phase shift governed by an expression similar to Eq. (3):

$$\Delta\phi = [f(\rho_a - \rho_{oa}) + g(\rho_d)]kl \quad (4)$$

where

$\Delta\phi$ = change in phase shift, radians

k = rf wave number, radians/m

f = air refraction coefficient, cm^3/g

g = dust refraction coefficient, cm^3/g .

This expression is strictly valid for propagation through a homogeneous medium, although the degree of approximation is quite good unless severe diffraction effects occur because of strong gradients or changes in

refraction. Because significant diffraction will produce amplitude perturbations as well, its presence can be readily detected.

A related issue is that of spatial resolution, which is determined by diffraction rather than by the antenna beamwidths. An effect of diffraction by a medium of variable refractivity is the filtering of contributions to the received signal that arise from spatial variations of structure lateral to the propagation path.⁵ Because of filtering, structure smaller than the Fresnel zone is about half as effective as large-scale structure at affecting the observed phase, although all scale sizes contribute. Amplitude variations predominately arise from structure smaller than the Fresnel zone.

The Fresnel zone reaches its maximum value at the center of the path between transmitting and receiving antennas. Its maximum value is given by

$$F = \sqrt{\lambda l / 2} \quad , \quad (5)$$

and the critical spatial wavenumber is

$$k = \sqrt{2\pi / F} = \sqrt{4\pi / \lambda l} \quad . \quad (6)$$

For the shock-tube tests, $\lambda = 0.9$ cm and $l \approx 1.8$ m, so $F = 9$ cm and $k = 0.3$ cm⁻¹. Note that any structure flowing through the beam at faster than sonic velocities has temporal durations shorter than $F/c = (0.09)/(300) = 0.3$ ms, which is about the time resolution of the equipment; thus, the spatial resolution in the flow direction is matched to the temporal resolution specified for the measurements.

The total rf plane shift also depends on the free-space path length between the antennas:

$$\phi_t = kl + \Delta\phi \quad . \quad (7)$$

Because it is desired to measure $\Delta\phi$ to a few electrical degrees, and $k = 7.024 \text{ cm}^{-1}$, care must be taken to ensure that path length changes produced by the detonation are less than about $\Delta l = 0.05/k = 0.04 \text{ mm}$. This is approximately the magnitude of the diametrical expansion of the shock tube under a 30-psi static load.

2.2.2.1 Gas (Air) Contribution--The quantity "f" in Eq. (4) is related to the radio refractivity of air, which has been studied for several decades and has a well-established value. This is given by

$$N_a = 77.6 \frac{P}{T} - 71.6 \frac{e}{T} + 3.75 \times 10^5 \frac{e^2}{T^2} \quad (8)$$

where

P = dry air partial pressure in mbar

e = water vapor partial pressure in mbar

T = absolute temperature in K.

In terms of refractivity, the phase change is

$$\Delta\phi = N \times 10^{-6} k l \quad (9)$$

Comparing Eq. (4) with Eq. (9) and applying the gas laws for dry air and vapor, we obtain

$$\Delta\phi = \left[0.223 \rho_d + 1.72 \times 10^3 \frac{\rho_v}{T} \right] k l \quad (10)$$

where

ρ_d = dry air density in g/cm^3

ρ_v = vapor density in g/cm^3 .

Assuming that the mixture of gases does not change with time,

$$\rho_v = w \rho_d \quad (11)$$

and

$$\rho_a = (1 + w)\rho_d \quad . \quad (12)$$

Further, assume that changes occur adiabatically, so that

$$\frac{\rho_v}{T} = \frac{\rho_v^{2-\gamma}}{T_o \rho_{ov}^{1-\gamma}} \quad (13)$$

where

γ = ratio of specific heats (= 4/3 for H₂O)

T_o = ambient temperature.

Then, after inserting Eq. (13) into Eq. (10) and retaining the leading terms of a Taylor series expansion, we obtain

$$f = 0.223 \left(\frac{1 + 5.14 \times 10^3 w \gamma / T_o}{1 + w} \right) \quad . \quad (14)$$

This expression is the basis for "calibrating" the air density contribution to mmW phase shift. Because $T \approx 300$ K and w ranged up to 7 percent, the water vapor correction could be as great as about 15 percent.

Most of the common gases, including helium and those produced as products of the detonation of the shock-tube driver, have molar refractivities similar to that of air. The refractivity of helium is

$$N_{he} = 1.98 \times 10^5 \rho_{he} \quad .$$

which differs from that of dry air by 11 percent at the same mass density. Thus only a small error will be incurred by using the value for air refractivity to estimate the density of mixtures of helium and air. Although combustion products will not be present in the shock front, which is the region of primary interest, we will make the assumption that the refractivity of an air/combustion product mixture is also that of air when considering conditions after the positive phase.

2.2.2.2 Dust Contribution--The effects of dust on the rf propagation can be described by the Rayleigh mixing law,

$$\frac{1}{\rho_s} \left(\frac{\epsilon_s - 1}{\epsilon_s + 2} \right) = \frac{1}{\rho_d} \left(\frac{\epsilon_d - 1}{\epsilon_d + 2} \right) \quad (15)$$

where

ϵ_s = (complex) relative dielectric constant of solid soil material

ρ_s = mass density of solid material

ϵ_d = relative dielectric constant of dust-laden volume

ρ_d = dust mass density.

Although Eq. (15) strictly applies (theoretically) only when all of the particles are in the Rayleigh regime (circumference smaller than the rf wavelength), it is accurate when the lofted dust mass is dominated by the small-particle end of the dust size distribution. Solving Eq. (15) under the condition that $\rho_d \ll 1$, we obtain an expression for the excess phase shift produced by the dust,

$$\Delta\phi = \frac{3}{2} \left(\frac{\rho_d}{\rho_s} \right) \left(\frac{\epsilon_s - 1}{\epsilon_s + 2} \right) k l \quad \text{radians} \quad (16)$$

so

$$g = \frac{3}{2} \left(\frac{\epsilon_s - 1}{\epsilon_s + 2} \right) \rho_s^{-1} \quad (17)$$

Actual values for g must be obtained by measurement, which is done by packing soil in a test fixture and measuring the density and relative dielectric constant. Because of the impracticality of creating a truly solid mass of the soil material, we assume that Eq. (15) applies for the material in the test fixture, so that the s subscript for ρ_s and ϵ_s indicates sample. This is equivalent to asserting that the Rayleigh mixing law applies for all densities, for which there is experimental existence.⁶

An expansion similar to Eq. (16) holds for the attenuation of the rf signal because of absorption by the dust particles:

$$a = 39.1 \left(\frac{\rho_d}{\rho_s} \right) \left(\frac{\epsilon_s \tan \delta_s}{\epsilon_s + 2} \right) \text{ kl dB} \quad (18)$$

where $\tan \delta_s =$ loss tangent of solid material. Because $\tan \delta_s$ is very sensitive to moisture content (i.e., water molecules absorbed on the particles), it is impossible to obtain a value for a with laboratory measurements that will apply accurately for an in situ test. However, ϵ_s turns out to be rather insensitive to moisture content, and the mathematical form of Eq. (17) makes g rather insensitive to changes in ϵ_s .

2.3 COMBINED MEASUREMENTS.

The experimental arrangement was such as to maximize the overlap of the X-ray beam and the mmW signal path. This was accomplished by installing the mmW antennas as close as practical to the X-ray source and detection, and to place one antenna upstream and the other downstream of the associated X-ray equipment so that the paths crossed in the measurement region. To the accuracy of the assumptions and approximations discussed above, the measured phase shift and X-ray absorption because of changes in dust and air density are given by Eq. (3) and Eq. (4).

Solving these simultaneous linear equations, we obtain expressions from which fluctuations in air and dust density can be computed from the measured quantities:

$$(\rho_a - \rho_{a0}) = \frac{1}{D} \left[G \left(\frac{\Delta\phi}{k\ell} \right) + g \left(\frac{1}{\ell} \ln \frac{I}{I_0} \right) \right] \quad (19a)$$

$$\rho_d = \frac{1}{D} \left[-F \left(\frac{\Delta\phi}{k\ell} \right) - f \left(\frac{1}{\ell} \ln \frac{I}{I_0} \right) \right] \quad (19b)$$

where

$$D = (fG - gF)$$

or

$$\Delta\rho_a = u_1 \Delta\phi - v_1 \left(- \ln \frac{I}{I_0} \right) \quad (20a)$$

$$\rho_d = -u_2 \Delta\phi + v_2 \left(- \ln \frac{I}{I_0} \right) \quad (20b)$$

Equations (20) can be rewritten as

$$\Delta\rho_a = \frac{G}{k\ell D} \left[\Delta\phi - \left(\frac{kf}{G} \right) \left(- \ln \frac{I}{I_0} \right) \right] \quad (21a)$$

and

$$\rho_d = \frac{F}{k\ell D} \left[-\Delta\phi + \left(\frac{kf}{F} \right) \left(- \ln \frac{I}{I_0} \right) \right] \quad (21b)$$

The accuracies of the separation of mmW phase and X-ray absorption into estimates of air and dust densities depends, respectively, on the ratios of the factors relating to dust effects and those relating to air effects on mmW propagation and X-ray absorption. This point will be discussed below (Section 2.5.5).

2.4 SOURCES OF EXPERIMENTAL ERROR.

There are a number of sources of potentially important experimental problems, some of which have been introduced above. The following is a list of actual and potential sources of error:

- (1) Calibration error
- (2) Mechanical disruption of X-ray and mmW electronic equipment
- (3) mmW antenna motion
- (4) Electronic noise and interference
- (5) Gain and baseline level drifts and instability
- (6) Multipath reflection of rf signals within shock tube
- (7) Refraction of mmW signals
- (8) Mismatch between mmW and X-ray beams
- (9) Significant structure in shock wave smaller than the beams
- (10) Extinction of the X-ray beam.

Calibration will be discussed below. Shocks that reached equipment located outside the tube caused mechanical disruption. This was manifested by noise transients induced in the X-ray detection signal on all tests, losses of mmW equipment phase lock on most tests, and impulses on the X-ray tube voltage and current (which were monitored quantities) on some of the tests. Considerable effort was expended to reduce these effects, but we were not able to eliminate them entirely by the end of the testing phase, partly because much of the equipment could not be sufficiently physically protected from the environment around the shock tube.

Accelerometers were installed on the support plates near the mmW antennas in an attempt to measure any motion. It was noted above that the calculated diametrical expansion of the shock tube under 30-psi static overpressure was about 0.04 mm, a value too small to affect the measurement. However, test results do not support this calculation.

Noise and interference did not appear to be a significant problem. Signal-to-noise ratios for the mmW measurements exceeded 40 dB. There was considerable ripple at twice the line frequency on the X-ray detector output, which was reduced, but not eliminated, by adding a secondary filter to the X-ray high-voltage power supply. The remaining 120-Hz ripple could be dealt with adequately in the data processing.

Because the quantity potentially most sensitive to long-term drift was the X-ray detector zero level, it was measured as closely as possible in time before and after each test. Long-term drifts in the mmW phase because of ambient condition changes, such as temperature, occurred too slowly to affect the measurements. No gain drifts at all were observed. However, there apparently were some baseline changes in the mmW phase shift associated with mechanical disruptions. It was not possible to determine their exact cause or to repair the problem during the limited tests that were run (we believe that they were caused by a temperature-sensitive phase-locked loop that could exhibit multiple lock points). On occasion, baseline shifts in the X-ray output were noted, which were probably due to a blast effect that slightly altered the regulator setting of the nearby generator used to supply its power or that slightly changed the setting of the X-ray power supply.

Circularly polarized mmW signals were used to suppress specular reflections inside the tube, the most important of which was expected to be from the surface of the soil. Reflection from smooth metallic surfaces and from dielectric surfaces near grazing incidence reverses the sense of circular polarization, so 20 to 30 dB of suppression can be available readily, depending on the characteristics of the antenna used. An even number of such reflections is required to restore the original polarization. Diffuse reflection, such as from edges, rough surfaces, and the like, exhibits little polarization effect, but because diffuse reflection is much weaker than the specular type, it is not expected to be a problem. It was not possible to characterize the multipath environment within the shock tube because of its complexity. However, any significant multipath would be expected to produce amplitude

fluctuations because of interference between multipath signals experiencing different dust loadings along their respective paths. Because no amplitude fluctuations were observed on some tests, even though large swings in phase occurred, we conclude that multipath was insignificant in general.

The presence of this observation also indicates that there was no appreciable structure smaller than the beamwidth, at least on some of the tests, because the resultant diffractive effects include fluctuations in amplitude. In those instances, any mismatch between mmW and X-ray beams should be negligible as well.

Density gradients in the shock wave will cause rays connecting the transmitter and receiver to follow slightly curved paths as depicted in Figure 7. This refraction will increase the geometrical path length and

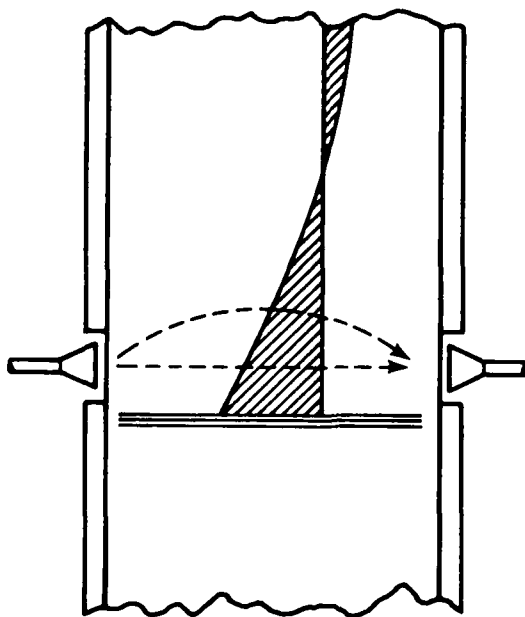


Figure 7. Refraction effect. Rays between the antennas will follow curved rather than straight paths if there is a density gradient.

thus introduce a phase shift in the same direction as an increase of density. Because changes in the refractive index across the shock front are on the order of 10^{-3} , this effect was expected to be small.

A simple model may be used to estimate the additional path length because of refraction from a density gradient. Figure 8 depicts this

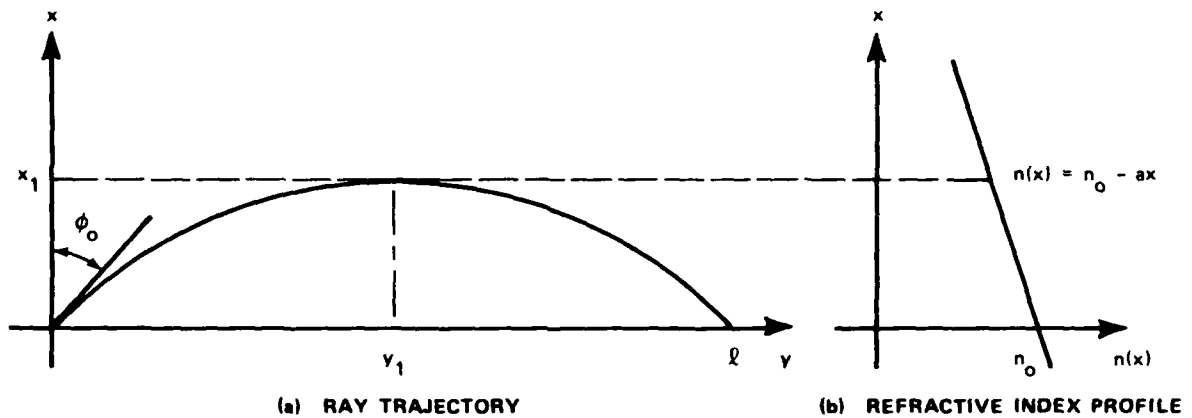


Figure 8. Example of refractive bending.

model, which consists of a linearly decreasing refractive index. Snell's Law describes the ray trajectory:

$$n(x) \sin \phi(x) = n_0 \sin \phi_0 \quad (22)$$

where $n(x) = n_0 - ax$. The point of "reflection" occurs at

$$x_1 = \frac{n_0}{a} (1 - \sin \phi_0) \quad (23a)$$

$$y_1 = l/2 \quad (23b)$$

By integrating $dy = \tan \phi \, dx$, we obtain

$$\begin{aligned}
l &= 2 \int_0^a \frac{n_0 (1 - \sin \phi_0)}{[n^2 - n_0^2 \sin^2 \phi_0]^{1/2}} dx \\
&= 2 \frac{n_0 \sin \phi_0}{a} \ln \left(\frac{1 + \cos \phi_0}{\sin \phi_0} \right) .
\end{aligned} \tag{24}$$

For situations of interest here, $\phi_0 \cong 90^\circ$ and $n_0 \cong 1$, so

$$\cos \phi_0 \cong \frac{al}{2n_0} , \tag{25a}$$

and

$$x_1 \cong \frac{n_0 a l^2}{8} . \tag{25b}$$

As an extreme example, suppose $n_0 = 1.002$ ($N_0 = 2000$ N - units) and $a = 2 \times 10^{-3}$ (scale length = 1 m). Then, for $l = 2$ m, $\cos \phi_0 \cong 2 \times 10^{-3}$, $\phi_0 \cong 89.889^\circ$, and $x_1 \cong 1$ mm. The lateral deviation is very small, as expected.

The change in electrical path length along the ray from the no-gradient situation is given by

$$\delta l = 2 s - n_0 l \tag{26}$$

where

$$s = \int_0^{x_1} n \sec \phi dx$$

$$\begin{aligned}
& \frac{n_0}{2} (1 - \sin \phi_0) \\
& = \int_0^a \frac{n^2 dx}{\left[n^2 - n_0^2 \sin^2 \phi_0 \right]^{1/2}} \\
& = \frac{n_0^2}{2a} \left[\cos \phi_0 + \sin^2 \phi_0 \ln \left(\frac{1 + \cos \phi_0}{\sin \phi_0} \right) \right]. \quad (27)
\end{aligned}$$

Using the numerical values from the example above, we find that $\delta l = 2.6 \times 10^{-6}$ m. Apparently, refractive effects are totally negligible.

Extinction of the X-ray beam occurred during the two tests (HST 143 and HST 144) when 40 kV was applied to the tube. By this, we mean that the X-ray signal was absorbed sufficiently so that it fell into the noise level (i.e., ran out of dynamic range). This produces a large error in the estimated X-ray absorption and should be avoided in general. It did not occur at 80-kV accelerating voltage.

Most of these potential sources of error were negligible, could be avoided, or were not manifested in the data. In the latter category are the issues of structure comparable to the beamwidth and of rf multipath. Motion of the mmW antennas and blast-related electronic effects turned out to be the largest sources of error in these first series of shakedown tests. They can be overcome with further refinement of the equipment.

2.5 CALIBRATION.

It is necessary to obtain values for the Factors F, G, f, and g used in Eqs. (3) and (4) in order to perform the computations of (21a) and (21b) required to interpret X-ray absorption and mmW phase shift in terms of average air and dust density.

2.5.1 mmW Phase Shift Caused by Air (f).

This parameter is defined by Eq. (14). All that is necessary is to obtain the proper values for w and T_o . These were obtained from the noontime records of the Albuquerque weather service; observations were taken at the Albuquerque airport, which is several miles from the shock tube. (A better procedure would be to have measured them at the actual time and place of the shots.) Table 1 lists the weather observations and f for the various test days. These values for the MINOR SCALE test are included as well. In this table, e_s is the saturation vapor pressure, which is computed according to

$$e_s = 10^{(9.40 - 2353/T)} \text{ mb} \quad (28)$$

and $e = re_s$, where r = relative humidity.

2.5.2 mmW Phase Shift Caused by Dust (g).

A value for g was obtained as described in Section 2.1.2.2. Soil samples from the shock tube were packed into a microwave test fixture and their dielectric properties and densities were measured. Table 2 summarizes these measurements. These samples were collected from the loose material at the soil surface during the first series of tests (21 and 22 August 1985), placed in sealed containers to avoid any change in moisture content, and returned to SRI headquarters for measurement. Some of the soil was dried by gently heating it in a vacuum, and samples of the dried material were also analyzed. Those data are also included in Table 2. (The weights of two of the Soil Samples (3) and (6) in their test fixtures were apparently either misread or misrecorded in the most significant digit and have been adjusted as indicated to make them consistent with the other results.)

Removing the moisture from the samples reduced the value of soil refractivity by about 10 percent. We will use the value for the as-is samples, or $g = 0.44$.

Table 1. Atmospheric quantities and mmW calibration factor.

Date	Event/Shot	P_t (mb)	T_o (° k)	e_g (mb)	r (%)	e (mb)	ρ_d (kgm ⁻³)	ρ_v (kgm ⁻³)	ω	f (cm ³ g ⁻¹)
6/27/86	MINOR SCALE	857.9	298.0	31.8	32	10.2	1.00	0.0074	0.0074	0.250
8/21/86	HST130/131	842.5	298.8	33.5	49	16.4	0.98	0.012	0.0122	0.266
8/22/86	HST132/133	841.7	302.1	40.8	33	13.5	0.97	0.0097	0.0100	0.258
9/25/86	HST141/142	838.6	293.2	23.7	26	6.2	0.99	0.0046	0.0046	0.240
9/26/86	HST143/144	840.9	289.9	19.2	43	8.3	1.01	0.0062	0.0062	0.246

Table 2. Summary of dielectric measurements of shock tube samples.

Sample	Condition	ρ_s (g/cm ⁻³)	ϵ_s	g (cm ³ /g)
1	As-is	1.33	2.9	0.437
2	As-is	1.40	3.1	0.442
3	As-is	1.40*	3.1	0.442
4	Dried	1.39	2.9	0.418
5	Dried	1.45	2.8	0.388
6	Dried	1.44†	2.9	0.404
Average of as-is samples		1.38	3.03	0.440
Average of dried samples		1.43	2.87	0.403
Overall average		1.40	2.95	0.422

* Recorded sample weight raised from 6.11 to 8.11 g

† Recorded sample weight raised from 7.28 to 8.28 g

2.5.3 X-Ray Absorption by Air.

Values for F at 40 and 80 kV were obtained by sending X rays through a 10-ft-long pipe which could be pressurized. For safety reasons, aluminum end plates thinner than 3/16 in. could not be used. This is somewhat unsatisfactory, particularly at 40 kV, because the amount of spectral hardening is probably different from that of the actual measurements. The difference between the calibration measurements and the shock-tube setup is that 1/8-in. Lexan windows rather than 3/16-in. aluminum were in the beam. A better (although more costly) procedure would be to use beryllium windows in the pipe or a beryllium/Lexan sandwich.

The results of the X-ray/air-density calibration runs are summarized in Figure 9. There is considerably more scatter in the 40-kV data because the observed absolute X-ray detector signal is a factor of

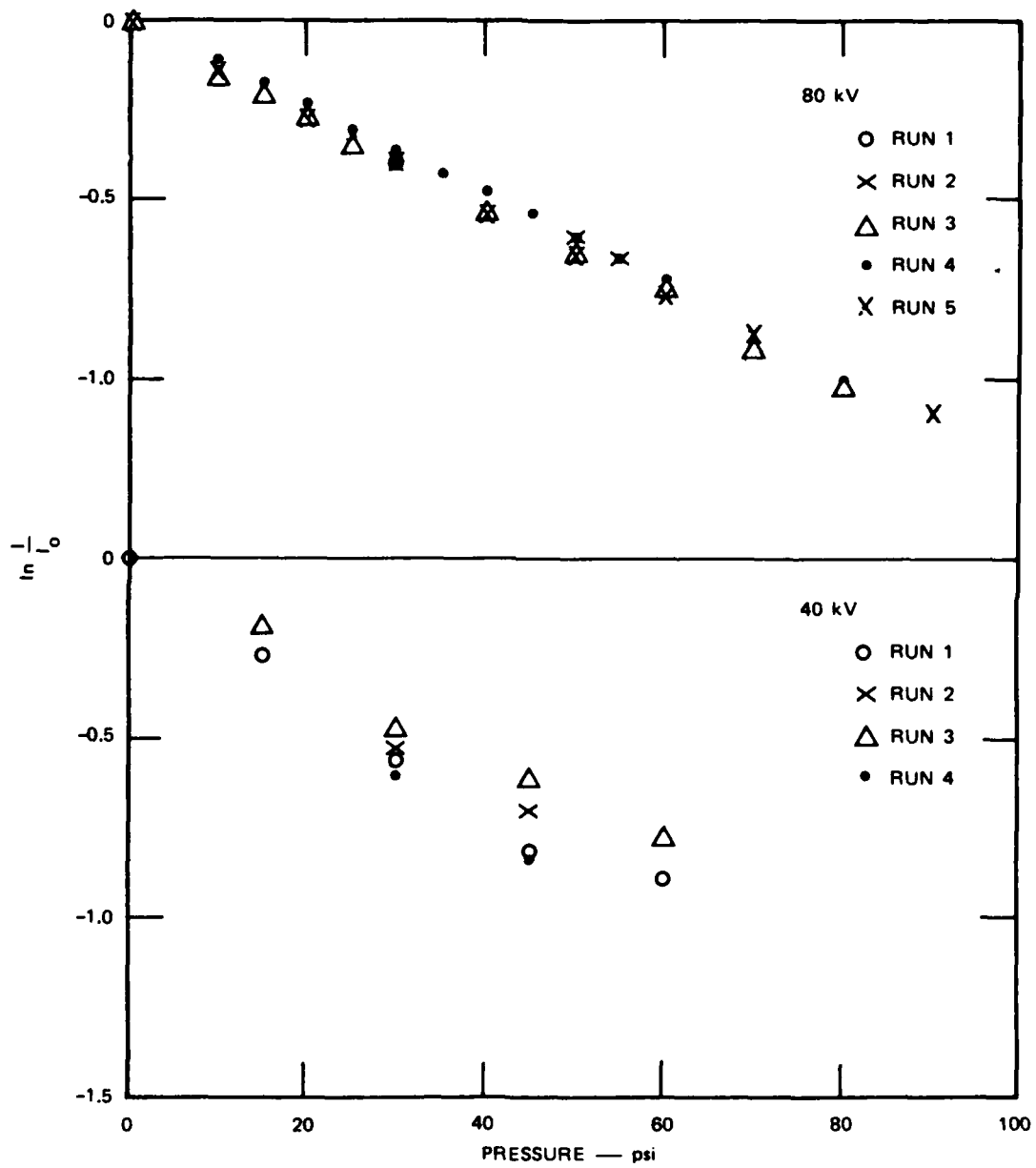


Figure 9. X-ray calibration results for air.

9 weaker at 40 kV than at 80 kV.* Drifts in the power supply voltage also contributed to the greater variation at 40 kV; the power supply appeared to be less stable at the lower voltage. Excellent repeatability was attained for the 80-kV measurements.

Regression analysis of the data shown in Figure 9 produced the following values for F:

X-Ray Voltage (kV)	F (cm ² /g)
40	0.36
80	0.25

The conversion from pressure to density is based on application of the gas law for air at the measured room temperature of 25.8° C. This regression was done by first averaging all the data points for a given pressure reading. The accuracy of an individual pressure reading is estimated to be ±2 psi.

Figure 10 compares these measured values for F to that computed in our analysis of X-ray data. At 80 kV, the measured absorption corresponds to that for 40-kV photons, which is consistent with the expectations of spectral hardening. A comparison of these results with Figure 4 shows that the spectra at both 80 and 40 kV are quite monochromatic. Note that the absorption rises very rapidly with decreasing photon energy below 40 kV, a feature that makes use of softer X rays less attractive.

It appeared that Teflon (...C₂F₄...) might be a good substitute for air for calibration purposes because its calculated absorption coefficient based on its atomic composition is close to that

* Most of this difference is due to the lower sensitivity of the detector for less energetic X-ray photons.

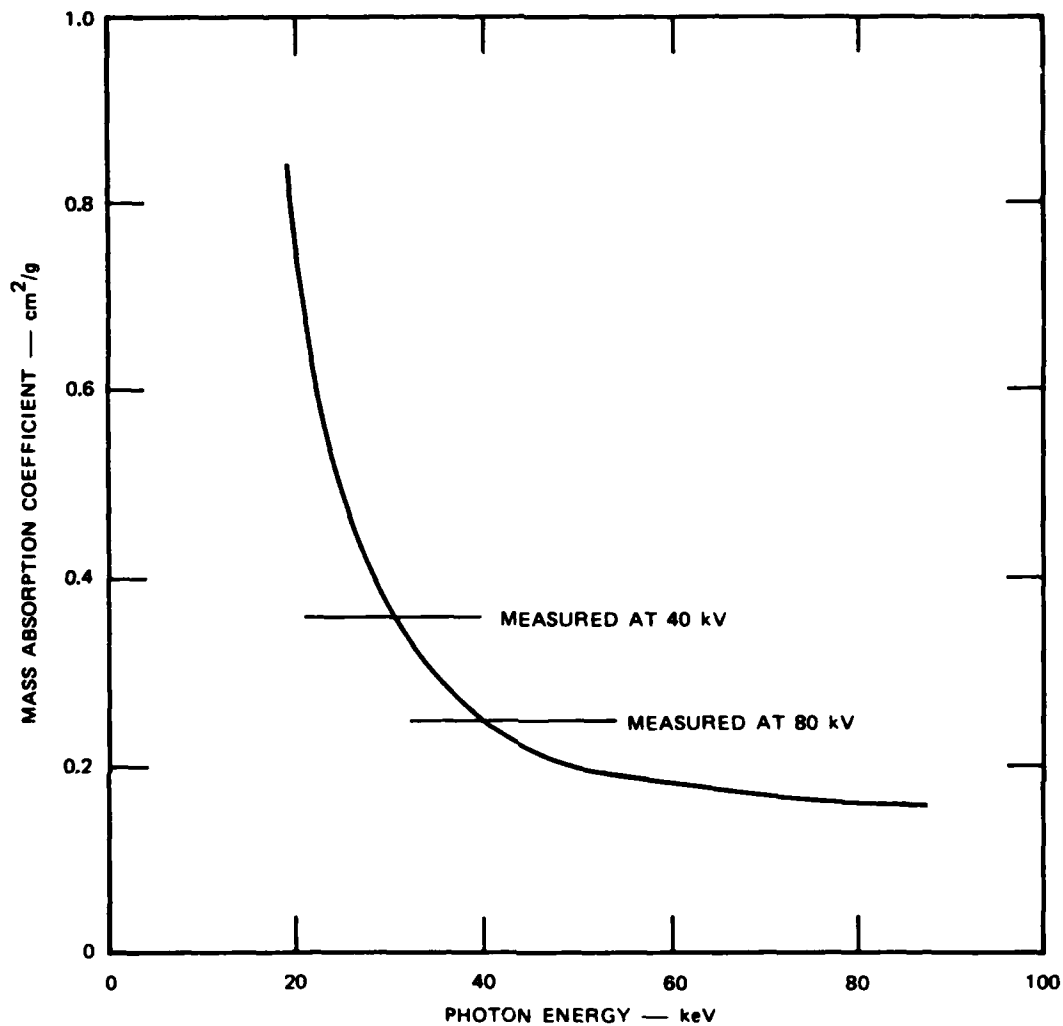


Figure 10. Mass absorption coefficient vs photon energy for air.

of air, and Teflon is an easy material to handle. However, calibration runs using various thicknesses of Teflon produced inconsistent results that also indicated more absorption than air of the same integrated density. We subsequently learned that manufacturers of Teflon add lubricants, especially those based on molybdenum compounds, to enhance its slipperiness. These additives apparently produced the anomalous results.

2.5.4 X-Ray Absorption by Soil.

Values for G were obtained by placing this section of soil samples in the X-ray beam. Figure 11 summarizes the results of a number

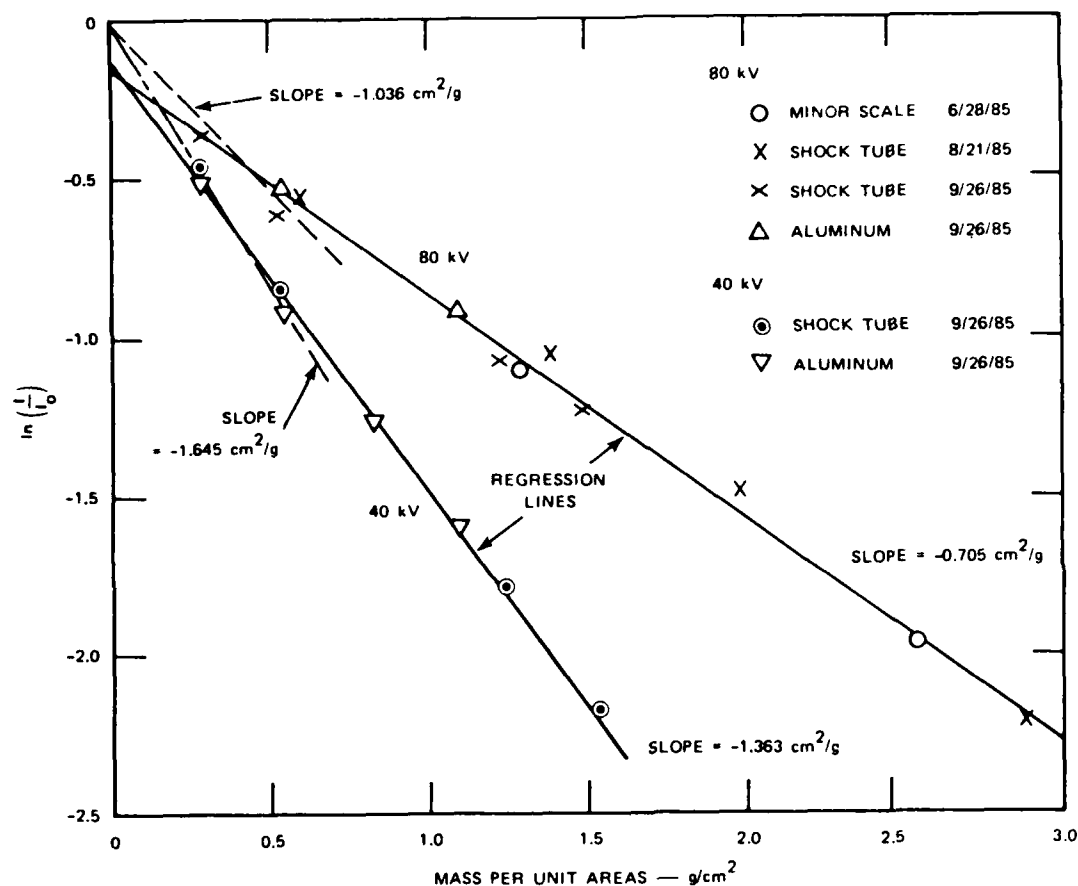


Figure 11. X-ray soil calibration.

of these calibration runs using soil samples collected from both the shock tube and from the MINOR SCALE precursed radial. There is evidently no significant difference between the mass absorption coefficients for these soils. Also shown in Figure 11 are the mass absorption coefficients for aluminum, which is a good simulant for these soils.

It is noteworthy that the MINOR SCALE calibrations were run using a 20-ft separation between the X-ray source and detector as opposed to about a 6-ft spacing for the shock tube. The consistency of results between these different geometries is evidence that off-axis multiple scattering of X rays by air molecules (and dust particles) was insignificant. First-order scattering of X rays was observed; this was particularly intense near the beam exit from the tube.

Regression analyses were made of the data shown in Figure 11. These produced the following values for G:

X-Ray Voltage (kV)	G (cm ² /g)
40	1.36
80	0.705

Both regression lines should pass through the origin in Figure 11. The discrepancy at the origin may be due to spectral hardening.

2.5.5 Calibration and Accuracy Requirements.

Table 3 summarizes the values obtained for four parameters needed to convert the mmW phase and X-ray absorption into mean air- and dust-density estimates. The value for f is an average shown for comparison; for density calculations the value appropriate for the day of the test is used (Table 1). The f and g factors need to be multiplied by the rf wave number ($= 7.024 \text{ cm}^{-1}$) to convert them to the same units as F and G. Note that the air absorption coefficient is significant compared to that for dust. This means that ignoring changes in air density would lead to a fairly large error in estimating fluctuations in dust density in the shock wave. At lower X-ray energies the ratio of air to soil absorption coefficients should remain nearly constant, as shown in Figure 2.

Table 3. mmW and X-ray calibration factors.

X-Ray Voltage (kV)	f (cm ³ /g)	g (cm ³ /g)	F (cm ² /g)	G (cm ² /g)
40	0.25	0.44	0.36	1.36
80	0.25	0.44	0.25	0.705

Separating mmW phase and X-ray absorption data to estimate air and dust density requires taking the difference between weighted measured quantities of comparable magnitude. For example, with $\Delta\rho_a = \rho_d = 10^{-3} \text{ g/cm}^3$ and using the nominal values for f, g, etc., as given in Table 3, $\Delta\phi = 0.79 \text{ rad}$ and $-\ln(I/I_0) = 0.156$. Putting these values back into Eq. (21) with $t = 163$ leads to

$$\Delta\rho_a = (7.37 - 6.37) \times 10^{-3} \text{ g/cm}^3 \quad (29a)$$

$$\rho_d = (-2.61 + 3.61) \times 10^{-3} \text{ g/cm}^3 \quad (29b)$$

Suppose that the accuracy specification on $\Delta\rho_a$ and ρ_d is $\pm 10^{-4} \text{ g/cm}^3$ (i.e., ± 10 percent of ambient air density). Then an analysis shows that the ratios (f/F) and (g/G) need to be known to about ± 1.5 percent and ± 3 percent, respectively. The calibration factors themselves need only be known to within about ± 15 and ± 30 percent. However, the phase shifts and X-ray absorptions have to be measured to the stricter accuracy standard.*

Note that estimating the changes in air density requires good knowledge of dust-calibration factors (i.e., g/G); the reverse is true for the dust-density case. Thus, the most stringent accuracy requirement is on the ratio (g/G), which is composed of the most difficult to measure and likely to be the least repeatable (from test to test) factors.

The late-time data from the shock tube tests provide both a check on the accuracy of the soil calibrations and a better estimate of

(g/G). At later times, the air density should have nearly reached its ambient level, so variations in mmW phase and X-ray absorption should be due mainly to dust alone. Thus, the ratio $G/(gk)$ can be compared to the data, as shown in Figure 12. (These data points were obtained from the results to be presented in Figure 40 in Section 5.4.1.4.) The theoretical behavior computed from the calibration results is in reasonably good agreement with the late-time data, which support the general accuracy of the soil calibrations for both mmW phase shift and X-ray absorption.

However, for the HST 142 (80-kV) test, it is clear that the observed shape differs sufficiently from the expected one that the required accuracy for (g/G) is probably not achieved. The slope of the HST 142 regression line is 0.335, which is 47 percent greater than expected from the calibration data (0.228). On the other hand, the HST 143 (40-kV) regression line agrees with the calibration data to three significant figures. Both of these regressions appear to be statistically valid with coefficients of correlation of 0.967 and 0.977.

Because the same soil was used for these two tests, it appears that the discrepancy in the HST 142 data is traceable to the 80-kV X-ray absorption calibration. Those calibration data appear in Figure 11. If the value for G of $0.705 \text{ cm}^2/\text{g}$ is increased by the ratio $(0.335/0.228)$, $G = 1.036 \text{ cm}^2/\text{g}$. This is plotted as the dashed line in Figure 11. It may be significant that this curve passes through the cluster of data points at 0.5 g/cm^2 . All of the test results produced X-ray absorptions that correspond to integrated densities in the 0- to 0.5-g/cm^2 range, which are equivalent to mean densities in the 0- to $3 \times 10^{-3}\text{-g/cm}^3$ range.

* Use of the corrected values for G presented below relaxes the accuracy requirements on the ratios by a factor of 2.

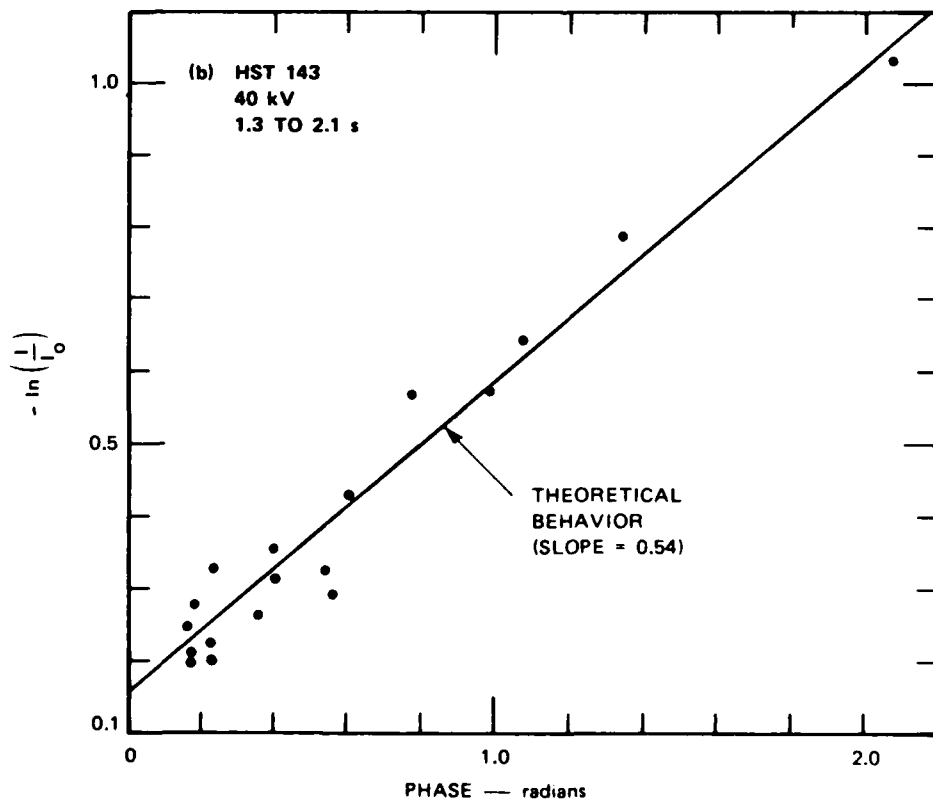
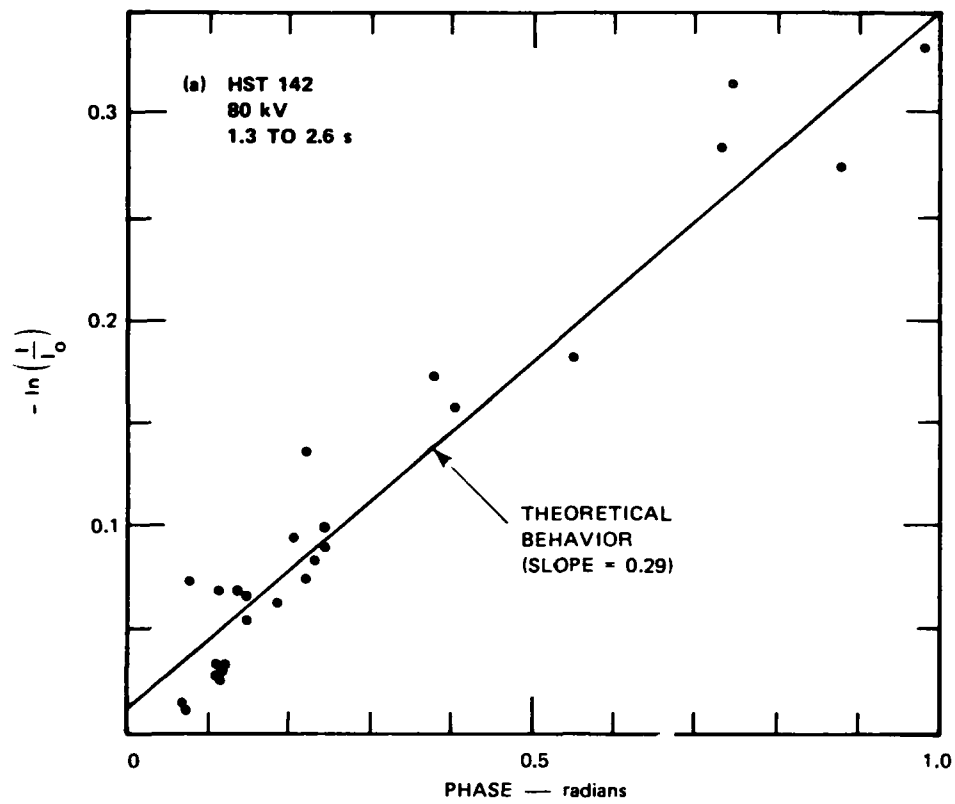


Figure 12. X-ray absorption vs mmW phase compared to the theoretical slope $G/(kg)$.

The interrupted line in Figure 11 was obtained from similar considerations. This is a manual fit through the origin and the two closest clusters of data points [a regression line through these points and the origin has a slope of $-1.618 \text{ cm}^2/\text{g}$ and an intercept at $\ln(I/I_0) = -0.012$]. Following Figure 2, we would expect a somewhat smaller ratio of X-ray absorption by soil to that for air at 80 kV than at 40 kV. At 80 kV, this ratio is $(1.036/0.25) = 4.14$ versus $(1.645/0.36) = 4.57$, which is consistent with this expectation.

These results point out the need for careful calibration. More X-ray calibration points are needed, especially for values of mass/area less than 0.5 g/cm^2 . Thin layers of aluminum must be used in this range because of the difficulty of making thin, uniform soil samples. In addition, harder, more monochromatic X-ray spectra should be employed, which can be obtained by using thicker (aluminum) filters. The same filters should be used for air and soil absorption calibration factor measurements, and both calibrations should be done using the test setup conditions.

SECTION 3

MICROWAVE SURFACE-RECESSION MEASUREMENT

3.1 INTRODUCTION.

The goal of this measurement is to determine how the surface responds to shock-wave passage. The most important objective is to measure the rate of surface mass loss, \dot{m}_d , with high time resolution. Additional objectives are to measure the compression of the surface and determine the vertical positions of constant-density surface as functions of time. Our final objective is to determine if a distinct surface exists throughout shock-wave passage or if a gradual density gradient occurs at some time.

This technique involves reflecting microwave signals obliquely below the surface (Figure 13). Those signals will experience a propagation delay (the soil is nondispersive, so the group and phase velocities are the same) that depends on the geometric path and the soil density along that path. By observing the changes in the delay time as the surface moves vertically and the soil is compressed and expanded, we can determine the amounts of motion and compression. Figure 13 shows how two paths change if the surface turns from an abrupt, distinct density interface to a gradual vertical gradient, as might happen during part of shock-wave passage. Because both the transmitting and receiving antennas will be buried below the surface, no part of the experimental equipment can disturb the flow and affect the measurements.

3.2 BASIS.

3.2.1 Total Internal Reflection.

It is well known that an electromagnetic signal propagating through a region of high refractive index toward one of lower dielectric

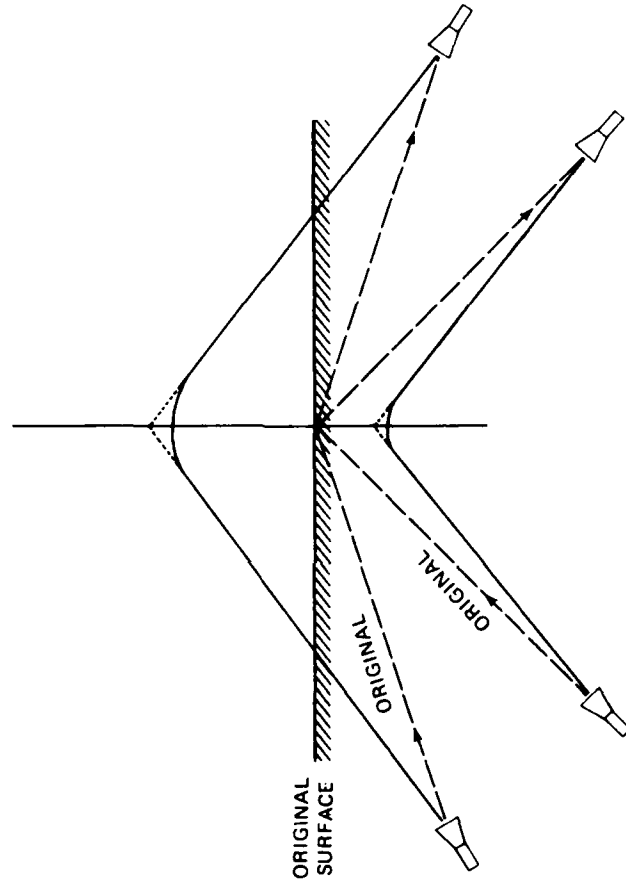
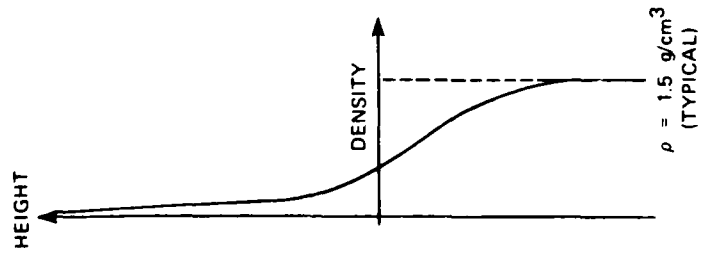


Figure 13. Total internal reflection surface recession measurement.

constant will be strongly reflected from the interface if the angle of incidence is smaller than a certain critical value. For a soil-to-air interface, the critical angle is a sensitive and well-defined function of soil density. The condition for total internal reflection is given by

$$\theta > \theta_c = \sin^{-1} \left(\frac{1}{n} \right) \quad (30)$$

Figure 14 contains plots of the relative dielectric constant, ϵ_r ,

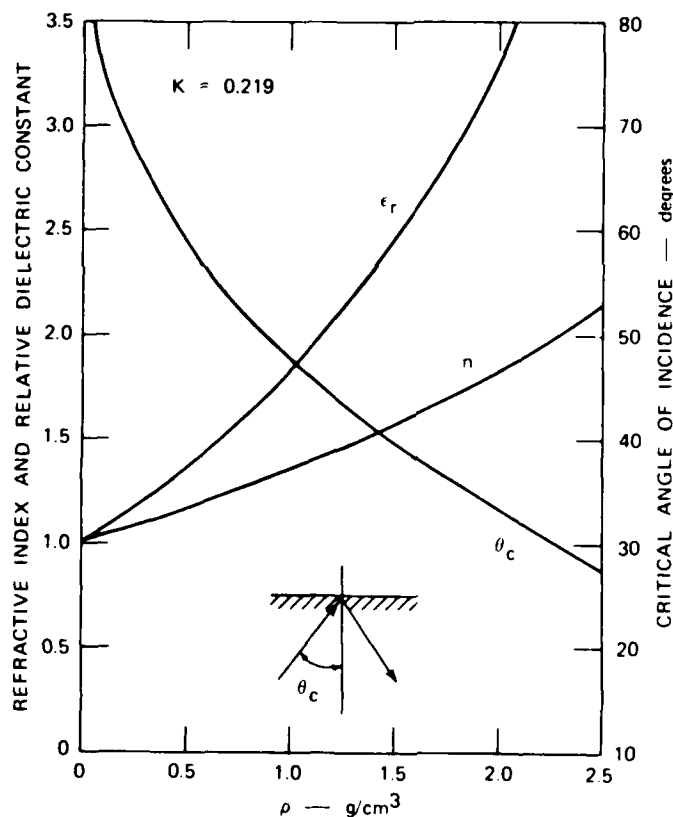


Figure 14. Total internal reflection parameters.

refractive index, n , and critical angles, θ_c , for total internal reflection as functions of density computed for the sample of surface sand collected at WSMR during the DICE THROW test. It is apparent that

the critical angle takes on quite practical values from an experimental point of view.

Use of an incidence angle larger than the critical one is essential to ensure a strong reflected signal; the power reflection coefficient drops rapidly from a value of unity under total reflection conditions towards that for the interface at normal incidence, which is about 4 percent for the WSMR sand at $\rho = 1.59 \text{ g/cm}^3$. The incident angle, of course, is established by the location of the antennas with respect to the surface and will vary slightly as the surface moves.

3.2.2 Refractive Reflection from a Density Gradient.

For the normal situation in which a true surface with an abrupt density change exists, the signals for any angle of incidence will reflect from the underside of the surface. However, if there is a gradual decrease in density with height, the rays will be refracted as shown in Figure 15, if $\theta > \theta_c$ and "reflection" occurs at the soil

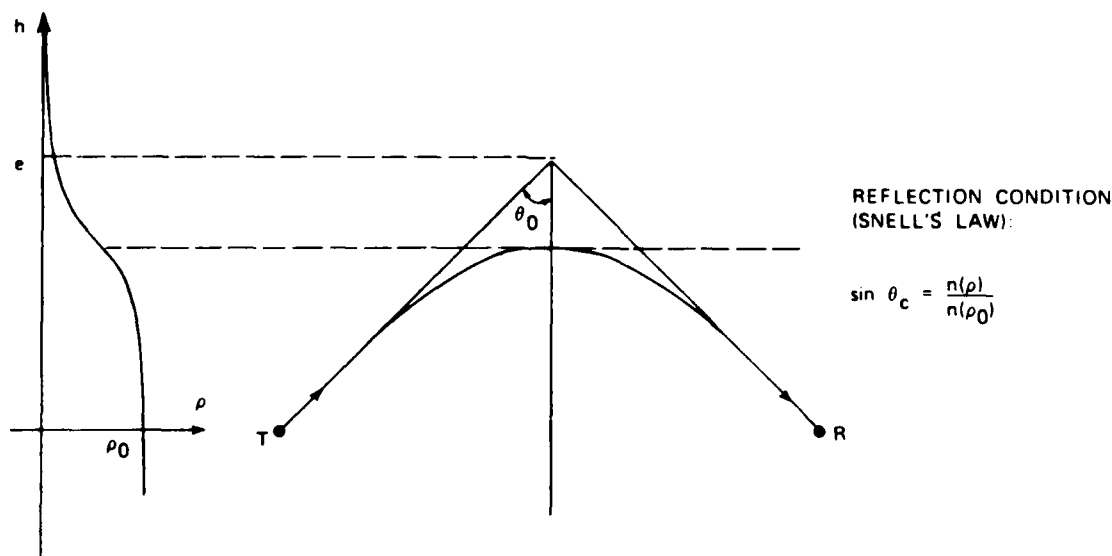


Figure 15. Refractive reflection with a density gradient.

density that just satisfies the relation

$$\sin \theta = \frac{n(\rho)}{n_0(\rho_0)} \quad (31)$$

where n_0 is the refractive index deep within the soil. Thus, by choosing the geometrical relationship, in principle it is possible to measure the location of the surface of any desired soil density. In practice, this cannot be done perfectly because there will be some variation in θ as the surface moves up and down. Also, there is a practical limit imposed by the need to avoid grazing angles of incidence. As seen in Figure 16, which plots θ as given by Eq. (31) for two values of ρ_0 , the largest value for ρ/ρ_0 that can be reasonably used is in the range 85 to 90 percent, or 75 .

It is not necessary for the density to decrease monotonically with height as shown in the various figures here. In fact, we expect the density for at least part of the duration of shock-wave passage to be greater near the surface than below. Under this circumstance, the wave will be refracted toward the vertical and then either reflect from the surface or be bent back when Eq. (31) is satisfied. Because the refractive index of the soil cannot be increased by compression by a large ratio with respect to n_0 and because θ_0 is of moderate value, the amount of refraction toward the vertical will not be large.

The electrical path length between the transmitter and receiver is

$$P_e = \frac{\phi}{2\pi\lambda} = \int_{\text{path}} n(\rho) ds \quad . \quad (32)$$

P_e is affected by both changes in the ray path and by the refractive index along the path. Values for the changes in P_e for the several paths have to be deconvolved in order to deduce the time-varying density profiles. The rate of mass loss below the highest density contour followed is estimated by integrating vertically across the density profile. The time rate of change of this quantity, which is the

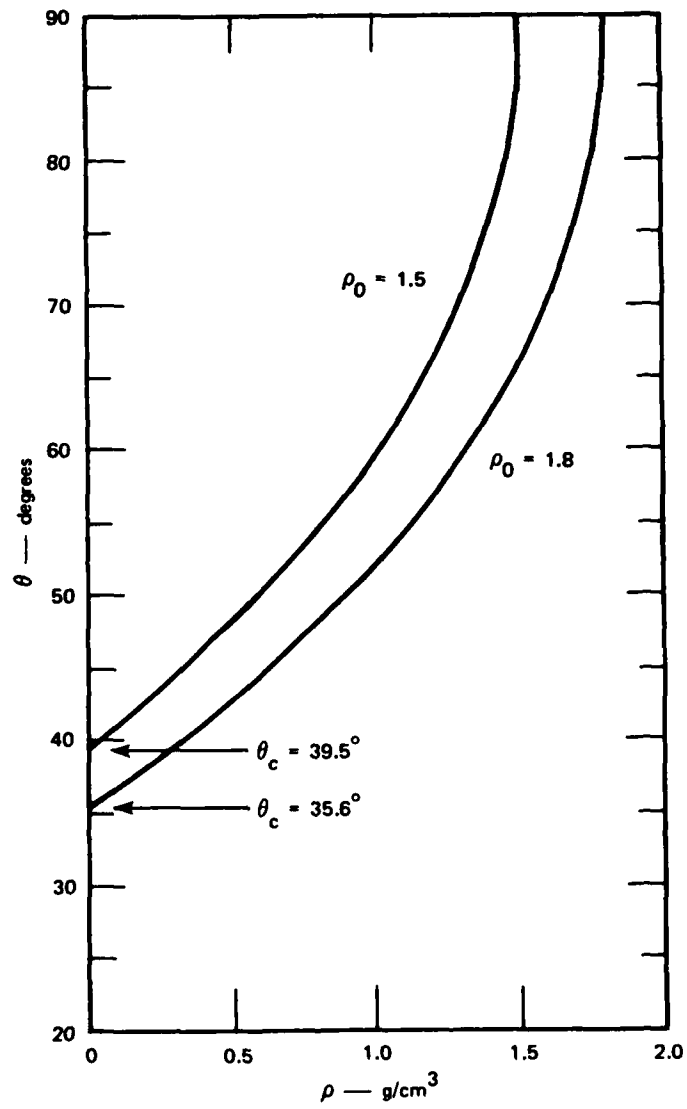


Figure 16. Incidence angle vs density to satisfy reflection condition.

columnar mass content in such units as g/cm^2 , is \dot{m}_d if a distinct surface is present. The interpretation becomes less meaningful if there is no distinct surface. However, there will be a distinct surface before and after the shock wave, and the overall change in mass content can be determined.

Implicit in this total internal reflection experimental concept is that plane waves are incident on the surface. This is an approximation for these measurements that is strictly correct when the antennas are far from the surface. Because of space restrictions in the shock tube and the high attenuation of microwave signals through soil, the antennas need to be placed relatively near the surface. The limited space within the shock tube also precluded using antennas of sufficient aperture to provide directional gain and locally, approximately plane waves. We assume that the plane-wave reflection conditions apply to these measurements.

A simple expression between phase shift and surface height change may be obtained under assumptions of negligible changes in angle of incidence and soil refractive index with height change. For a height change Δh with refractive index n_s at angle of incidence θ , the phase change is

$$\Delta\phi = 2n_s k \Delta h \cos \theta \quad . \quad (33)$$

Application of this expression is adequate for data analysis under most circumstances, such as with simple compression and rebound of a distinct surface. For more complex situations (such as refractive reflection when there is a strong gradient in refractive index, which would be associated with an indistinct surface), a more elaborate type of analysis is called for. This is described in Appendix A.

Conversion of soil refractive index to density requires application of a mixing law, such as the Rayleigh mixing law (Eq. 15) discussed above. Although the Rayleigh mixing law theoretically applies only for disperse mixtures, i.e., a dust cloud where the distances

between particles are large compared to their sizes, there is experimental evidence that it holds for dense mixtures or powders of natural materials as well.⁶ It was found that other mixing laws^{7,8} which had been proposed to account for the dense situation, did not fit as well as the Rayleigh law.⁶ These conclusions were based on measurements made on powders obtained by grinding up samples of various types of rocks--including granites, basalts, serpentine, and the like. The Rayleigh mixing law will be adopted here.

SECTION 4

DESCRIPTION OF EQUIPMENT

4.1 X-RAY/mmW SYSTEM.

Figure 17 presents a block diagram of the X-ray/mmW system. The X-ray system basically consists of a Phillips PW-2184-00 tungsten-target X-ray tube, a modified Universal Voltronics BAL-130-14 high-voltage power supply, and a scintillometer X-ray detector consisting of a 2-in. plastic scintillator, a 1-in. blue-enhanced PIN photodiode, and a battery-powered preamplifier/line driver. Modifications of the power supply were

- (1) Adding a motor drive to the voltage control variac and control circuitry to permit automatic remote operation.
- (2) Adding an additional R-C filter section to reduce ac ripple at the output.
- (3) Adding a high-voltage filament transformer.

The first of these modifications was necessary to permit raising the X-ray tube voltage slowly. The last was required because the X-ray tube had a grounded anode, which was water cooled.

A block diagram of the mmW system is shown in Figure 18. Phase-locked Gunn diode oscillators are used for both the receiver local oscillator and for the transmitter. The measurement frequency is 33.5 GHz, which is derived ultimately from a crystal oscillator. Through a series of down conversions, the mmW signal is brought down to a 50-kHz IF, where it is coherently detected. The detector outputs are the so-called "I-Q" quadrature signals, from which the amplitude and phase can be obtained according to

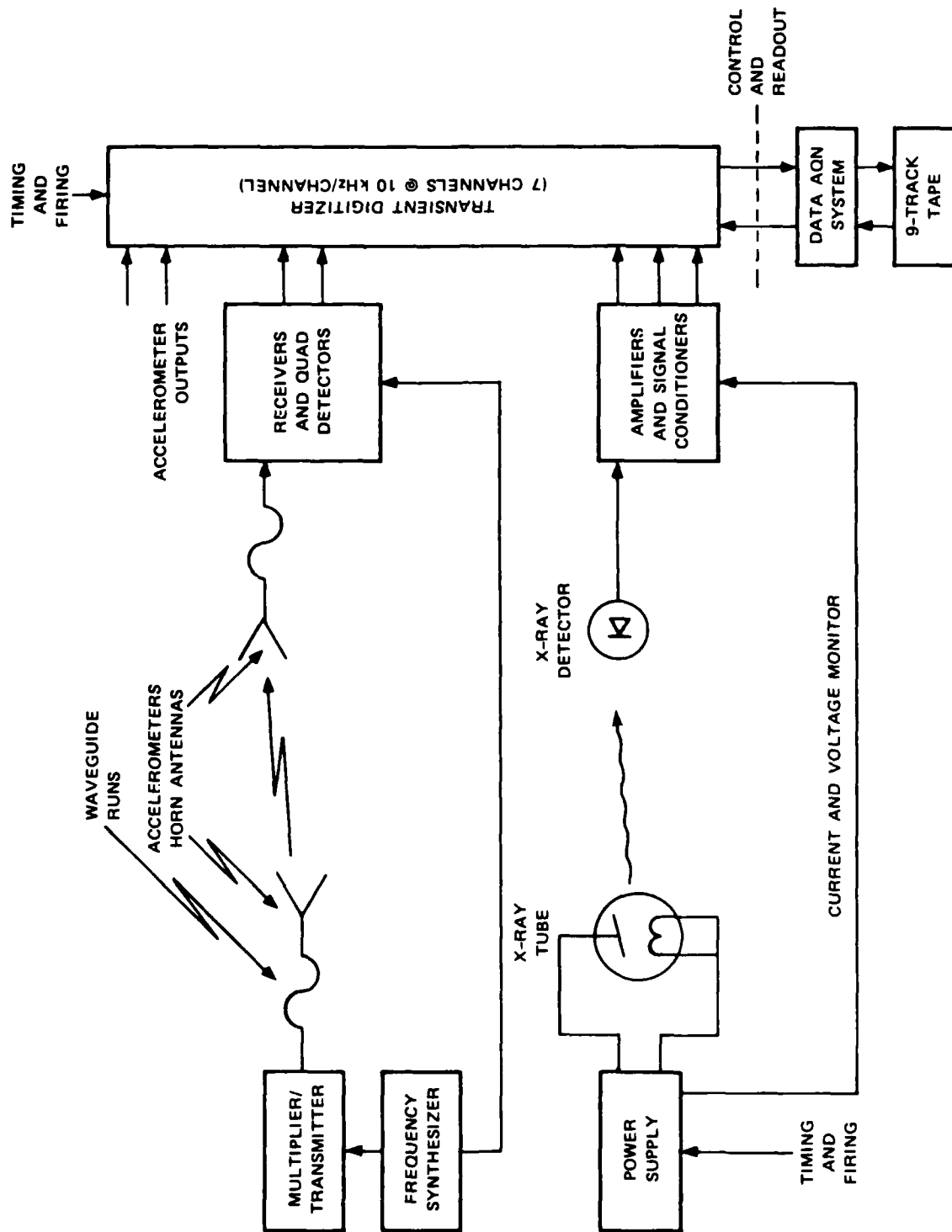


Figure 17. Block diagram of X-ray/mmW density-measurement system.

$$A = (I^2 + Q^2)^{1/2} \quad (34a)$$

and

$$\phi = \tan^{-1} (Q/I) \quad (34b)$$

This system is, in effect, a Mach-Zender interferometer; changes in the medium along the 33.5-GHz interferometer arm produce phase and amplitude changes that are recovered by the quadrature detectors.

4.2 SURFACE-RECESSION SYSTEM.

This system uses the same principle as the mmW system and is quite similar to it. Figure 19 shows a block diagram of the surface-recession system. Two transmitters and six receivers are used. The X-band frequencies used were 9.086 and 9.912 GHz. Each receiver produces an I-Q pair, from which the amplitude and phase can be computed according to Eqs. (34a) and (34b).

4.3 DATA-ACQUISITION SYSTEM.

An essentially independent CAMAC standard transient digitizer was used for the X-ray/mmW and the microwave surface-recession systems. Each digitizer consisted of a LeCroy 8212A/32 simultaneous sampling data logger capable of digitizing 16 channels of data at a 10-kHz rate with 12-bit dynamic range. Twelve memory modules for each digitizer provided enough memory (393,216 words) to store 4.92 s of X-ray/mmW and 2.46 s of surface-recession data. The X-ray/mmW measurement required 8 channels, and the surface recession needed 13 channels.

A DEC LSI-1123 controlled the digitizing system and was used to transfer the data to tape, which could either be 9-track or cartridge. This computer was also used for quick-look data analysis. The data transfer was programmed to occur immediately after the digitization interval was over in order to protect the data from loss because of power failure and the like. Once this data transfer was accomplished

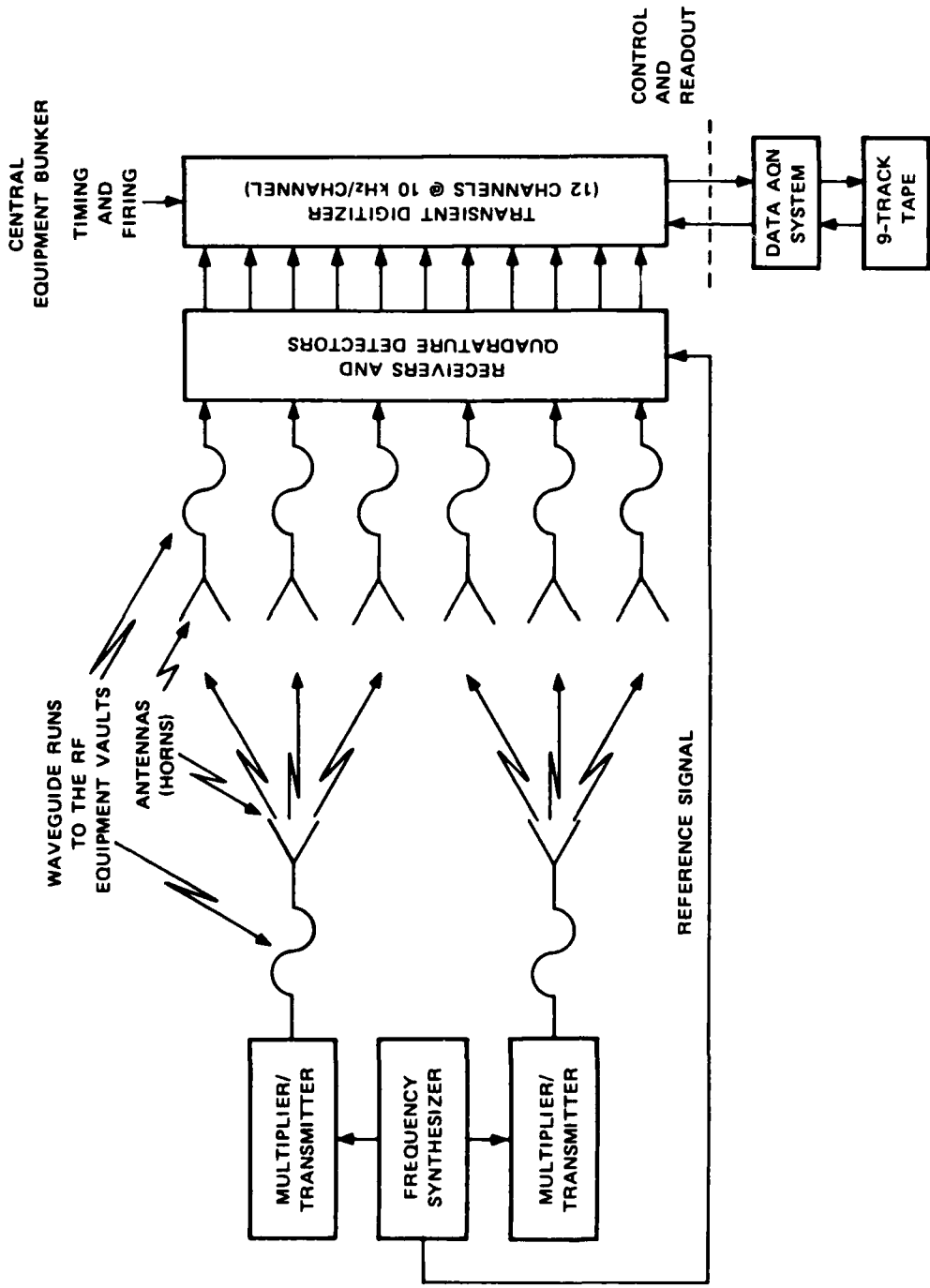


Figure 19. Block diagram of microwave surface recession system.

the system automatically reset itself and would execute another acquisition cycle if another trigger were received.

SECTION 5

FIELD TESTS AT THE 6-ft SHOCK TUBE

5.1 EQUIPMENT INSTALLATION.

All of the experimental equipment was installed on the outside of the 6-ft shock tube. Access for the mmW and X-ray beams to the interior of the tube was provided by ports cut into the tube. These ports had 0.125-in. Lexan windows nearly flush with the inside surface of the tube. Figure 20 shows a cross section of the installation, which was at roughly a 30-psi overpressure station. The path length between the center lines of the Lexan windows was 163 cm. Figures 21 and 22 are photographs of the installation.

Because the rf phase measurement is sensitive to changes in the physical path length between the antennas, it is essential to minimize any possible relative motion of the antennas. To accomplish this we decided to attach the antennas rigidly to the shock tube on plates bolted to the mounting flanges. The calculated diametrical expansion of the shock tubes under a 30-psi static load is less than 0.05 mm, which corresponds to a negligible rf phase shift of 2 deg. The dynamic expansion of the tube was also expected to be small. To first order any bulging of the Lexan windows would produce no effect because the amount of matter along the mmW and X-ray beams remains constant.

A block diagram of the overall system was presented in Figure 17 above. Although the system was constructed to permit measurements along two paths, only a single path measurement was implemented for shock-tube testing. This was done because it would simplify testing and because we believed that there would be little additional useful information from a second path in the shock tube. The X-ray power supply and part of the mmW equipment were set up near the shock tube. The remainder of the mmW

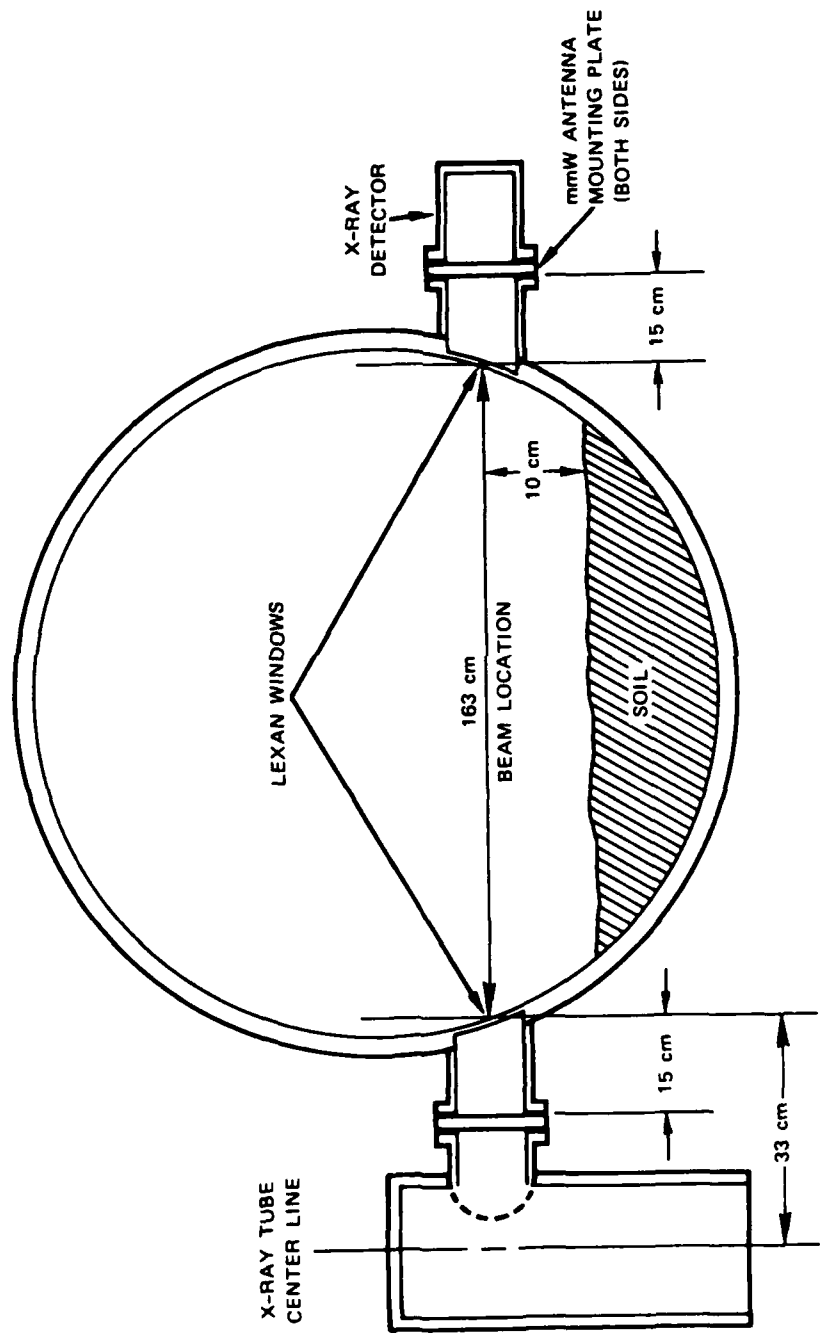


Figure 20. mmW/X-ray installation in a 6-ft shock tube.

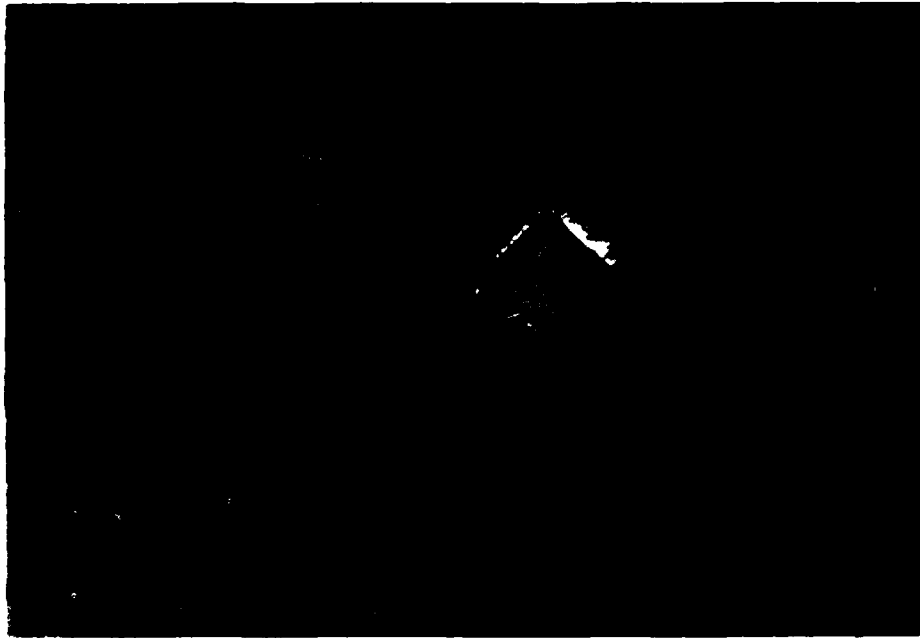


(a) TRANSMITTER SIDE. The X-ray tube was shock-mounted vertically in the 12-in. pipe for mechanical and radiation protection.

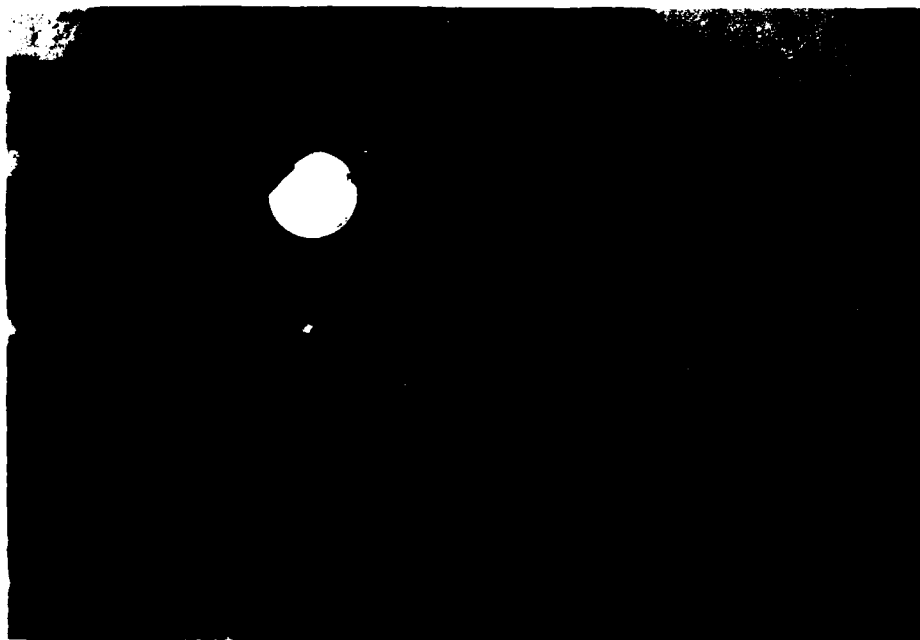


(b) RECEIVER SIDE. The X-ray detector had been removed at the time of this photograph.

Figure 21. External view of the X-ray/mmW experiment installation.



(a) TRANSMITTER SIDE. The X-ray tube is visible to the left of the mmW transmitter antenna.



(b) RECEIVER SIDE. The X-ray detector mounts in the circular hole to the left of the mmW receiver antenna.

Figure 22. View from inside the shock tube of the X-ray/mmW ports and installation.

equipment and the data-acquisition system were installed in a mobile home parked about 175 ft from the shock tube.

Because there was insufficient room within the soil layer, the surface-recession antennas were mounted on the outside of the shock tube so that they protruded through small (2-in. diameter) ports cut into the bottom of the tube. These antennas consisted of waveguide sections into which pyramidal dielectric (Teflon) matching sections had been placed, and, hence, were effectively nondirectional. In addition, it was only possible to install three receiving antennas instead of six because of restrictions on the number of closely spaced holes that can be cut into the shock tube. Each antenna fed two receivers, which provided for six signal paths, as shown in Figure 23. Table 4 lists the positions of the antennas and the nominal angles for specular reflection. Although the constraints on antenna placement produced a duplicate reflection angle, the range of angles spanned that expected for total internal reflection. That is, the high-incidence-angle signals should be significantly stronger than the low ones, and changes because of compression at the surface were expected to produce a transition to total integral reflection and a signal increase on some of the low-incidence-angle paths.

As discussed above, laboratory measurements of the dielectric properties of the soil used in the shock tube showed that this material was particularly lossy at X band. In order to reduce the signal attenuation to an acceptable level, some of the soil near the antennas and along the signal paths was replaced by sand, as shown in Figure 23. This sand intrusion was approximately 1-ft wide. As also shown in Figure 23, a screen of microwave absorbing material was embedded below the surface to screen any direct signals from the transmitting to receiving antennas.

The rf equipment for the surface recession measurements were built into two weatherproof boxes that were set on the ground near the shock tube. I-Q signal pairs were sent via cables to the data acquisition system, which was in the mobile home.

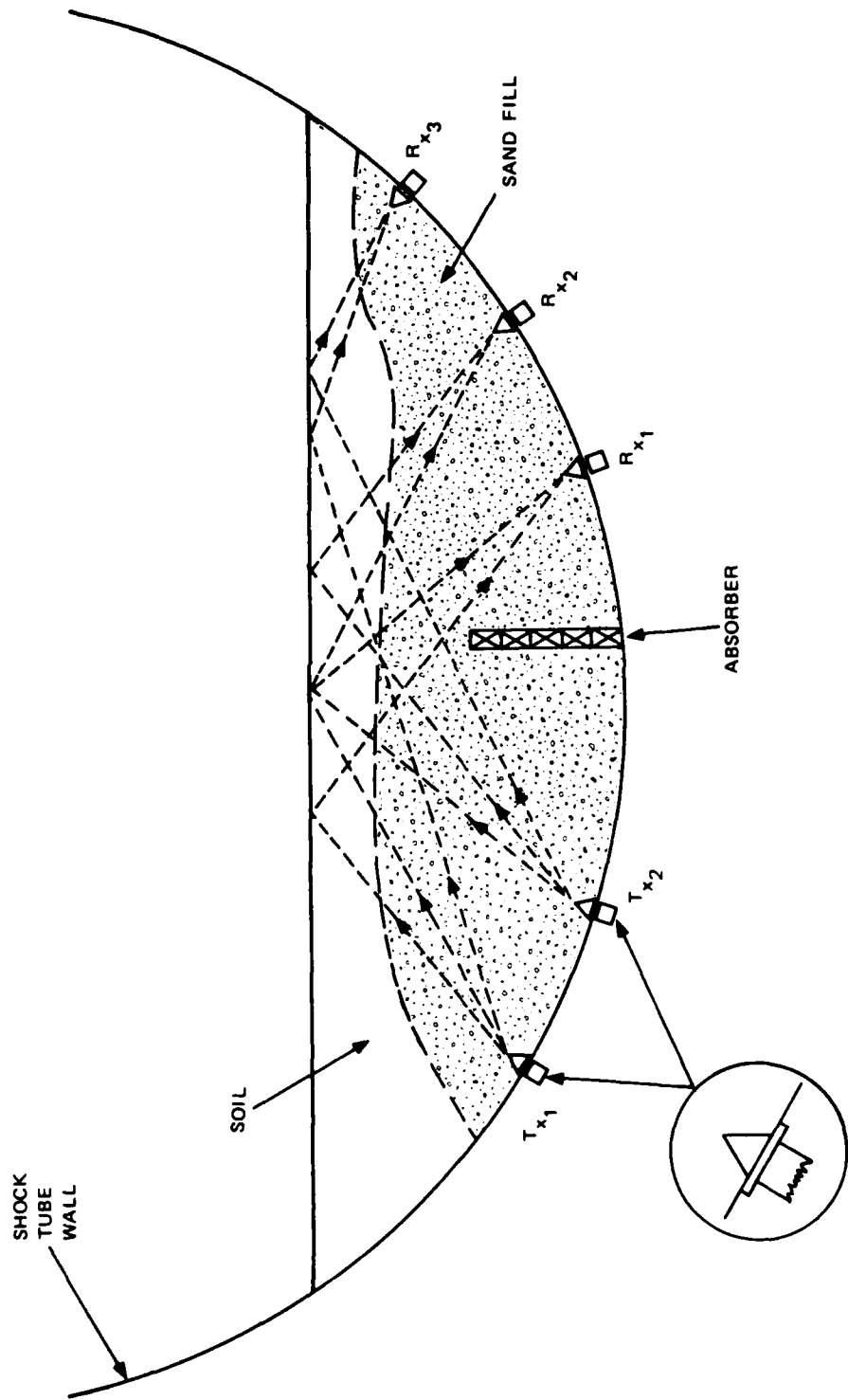


Figure 23. Cross section of surface-recessive installation in the 6-ft shock tube.

Table 4. Antenna positions and specular reflection angles.

Path	Transmitter (θ)	Receiving Antenna (θ)	Reflection Angle (deg)
1	1 (-31.4°)	1 (19.7°)	51
2	1 (-31.4°)	2 (32.4°)	61
3	1 (-31.4°)	3 (44.7°)	70
4	2 (-18.6°)	1 (19.7°)	40
5	2 (-18.6°)	2 (32.4°)	51
6	2 (-18.6°)	3 (44.7°)	56

Operation was entirely unmanned and accomplished by means of remote signals from the timing and firing system. The X-ray system was armed at about $T - 15$ min, when personnel were required to evacuate the area. A signal at $T - 5$ min completed arming the X-ray system, which was then activated by another signal at $T - 2$ min. This provided adequate time to ramp the X-ray voltage up to the desired value and stabilize. Data acquisition was started at $T - 0.8192$ s by a third signal. A fiducial signal at T_0 was recorded on one of the data-acquisition channels to establish precise timing. The overall data-acquisition interval was 4.92 s for the X-ray/mmW measurements and 2.46 s for the microwave surface recession measurements.

5.2 EQUIPMENT AND EXPERIMENT PROBLEMS.

Several problems were discovered during the first set (21 and 22 August 1985) tests at the 6-ft shock tube. The most serious of these were (1) difficulty in maintaining phase lock with the mmW system; (2) noise spikes in the X-ray detector signal; (3) overheating of the X-band surface-recession equipment that led to a loss of phase lock; and, (4) rf leakage of the surface recession signal apparently around the shock tube surface. Modifications and repairs made between the first set of

tests and the second set (25 and 26 September 1985) produced considerable improvement. Cooler weather in September also helped to alleviate the overheating problem.

Although the rf systems would occasionally lose phase lock spontaneously, the mechanical impulses due to firing the shock tube would usually cause a loss of lock. As this would occur after the leading edge of the shock front was well past, the most important part of the data was unaffected. Subsequent to the second set of tests we determined that the phase-locking problem with the mmW gear was due to excessive temperature sensitivity in a phase-locked oscillator that also exhibited two lock points. The oscillator had two tuning curves that overlapped over part of the temperature range and thus exhibited bistable operation.

It was discovered after the second series of tests that the accelerometer data were contaminated with an impulsive 120-Hz signal. This was apparently caused by pickup of leakage from the X-ray power supply, perhaps by means of cross talk from the X-ray voltage and current monitor cables. The accelerometer conditioning amplifiers and the X-ray HV power supply shared the same line power, and the signal cables ran alongside one another for a considerable distance to the data acquisition system. This contamination reduced the usefulness of the accelerometer data, although it was of sufficient quality to permit identification of an important mmW signal feature as being an artifact (cf., Section 5.4.1). Reversing the sign of one of the accelerometer signals by mounting the accelerometer on the opposite side of the antenna support plate would have permitted measurement of the differential motion between antennas and simultaneously suppressing common-mode interference. This change is recommended.

No specific component malfunction has been found in the X-band surface recession system. Our approach has been to increase the flow of cooling air. We believe that better environmental protection of both the mmW and X-band rf equipment from ambient conditions and the

mechanical effects of firing the shock tube are needed to overcome these problems completely.

We believe that the noise spikes in the X-ray detector signal were caused by minute mechanical vibrations of electronic components in the X-ray detector preamplifier feedback loop. This problem was attacked between the first and second series of tests by shock-mounting the circuit within a second box. However, the results from the second set of tests showed that this problem had not been totally eliminated, so a far more rugged version of the input stage of the preamplifier was designed and built. This new unit appears to be free of sensitivity to severe shocks.

The manifestations of the rf leakage problem were fluctuations in phase and amplitude produced when we worked around the antenna cables. rf energy was apparently flowing on or radiating across the outside surface of the shock tube. Attenuation of the signals within the soil were large enough that even such weak signals as those escaping from the shock tube could compete with them. This problem was attacked by adding microwave absorbing material around the outside of the shock tube where the antenna ports had been cut. This was not particularly successful, perhaps because rf energy was leaking from connectors, and the like, outside the shock tube. We believe that this problem can be overcome by electrically sealing the openings into the shock tube, applying the absorbing material more carefully, reducing the number of rf connections, using less lossy soil (sand), and employing more directional antennas. Directional antennas will increase the signal strength along the desired path and improve the geometry of the experiment by concentrating more rf energy in a smaller area.

5.3 TEST SUMMARIES.

During the months of August and September 1985, SRI conducted a fairly successful series of eight shots in the 6-ft shock tube at the Civil Engineering Research Facility/New Mexico Engineering Research Institute (CERF/NMERI) Shock-Tube Facility at Kirtland Air Force Base.

The shots were designed to produce 30-psi incident pressure levels at our installation station. These events included both precursed, with a helium layer, and nonprecursed shots. Although the primary objective of this testing was to develop the experimental equipment and technique, the important secondary objective was to obtain some data concerning the dusty flow. The 6-ft shock-tube test series are summarized below. The MINOR SCALE installation and results are described in Appendix B.

HST 130 (21 August 1985)--This was a nonprecursed test. For this first shot, the data-acquisition system received several false triggers including one at T - 90 s. This did not allow enough time for the system to record the data from the digitizer and reset itself before the actual shot. Consequently, no data were recorded. This problem was worked out with the cooperation of CERF/NMERI personnel and was satisfactorily resolved.

HST 131 (21 August 1985)--The triggering was correct for this second, nonprecursed shot. Reasonably good data were obtained overall with the X-ray system, which was operated at 80 kV. However, there were a large number of noise spikes in the X-ray detector signal. In addition, some drop-outs occurred in the mmW system after the beginning of the shock wave, which were apparently caused by microphonics. Good data were recorded on 13 of the 14 surface-recession system channels. The data on the 14th channel were partly clipped; this appeared to be a digitizer problem. For this shot, the soil above the surface recession raypaths was loosely in place, and permanent local upward displacement of a few centimeters of soil was observed on reentry into the shock tube. Our initial impression from the data was that they are consistent with an initial recession/compression followed by the disappearance of a discrete surface. Several such episodes of this phenomenon occurred during the test.

HST 132 (22 August 1985)--The third, nonprecursed test, produced mixed results. The X-ray system was operated again at 80 kV. The X-ray data were partly saturated owing to an error in setting the signal level in the digitizer because, when it was started that morning, the voltage

output of the generator supplying the power to the X-ray system had been set higher than it had been the day before. Still, a large part of the trace was visible and essentially repeated the waveform noted on shot HST 131. The problems with microphonics recurred on the mmW equipment at an even earlier relative time. Reasonably good data were obtained on all channels of the surface recession experiment, although the signals were relatively weak. For this test, the soil from HST 131 had been replaced with moister material, which had been compacted to match the rest of the floor of the shock tube. Considerably more signal attenuation resulted from the moisture in the material. After the test, the surface over the ray paths did not appear much different from the surrounding material. The soil was expected to dry out and be representative of the rest of the dirt in the shock tube.

HST 133 (22 August 1985)--During this fourth, nonprecursed shot, the X-ray system was operated with much softer spectra (40-kV accelerating voltage). A trace similar to the previous shots was obtained; however, it contained a number of noise spikes that came from the detector. Once again, the mmW equipment had problems with microphonics. The surface-recession system apparently overheated between the time of personnel evacuation and the shot and had lost lock by shot time. The higher ambient air temperatures that day may have been responsible for this problem.

HST 141 (25 September 1985)--This was a precursed test with a helium bag. The X-ray system operated at 80 kV. A few microphonic noise spikes were observed in the X-ray data, which was otherwise quite good. The mmW system had no problems this time because the equipment was better isolated from the shock wave. Even though the air flow through the equipment was improved, only fair surface recession data were obtained owing to an instability caused by overheating. However, because the surface recession equipment was better protected from the external shock wave this time, the system maintained lock.

HST 142 (25 September 1985)--This was a nonprecursed test with the X-ray system again operated at 80 kV. As before, several noise spikes

were seen in the X-ray data. Good mmW data were obtained up until the system lost lock at about T + 150 ms. The surface-recession system overheated and lost lock between the personnel evacuation time at T - 15 m and the shot.

HST 143 (26 September 1985)--This was a precursed test using the helium bag. We operated the X-ray system at 40 kV, which produces a different ratio of air/dust absorption. Again, some noise spikes occurred. Good mmW data were obtained as with HST 142. The mmW/X-ray results were essentially the same as with the previous precursed test, HST 141. We made further improvements in cooling the surface-recession equipment and experienced no problems; good data were obtained.

HST 144 (26 September 1985)--The last 6-ft shock-tube test conducted on this project was another nonprecursed test. The X-ray system was again operated at 40 kV. The mmW/X-ray results were essentially the same as for HST 142. Good surface recession data were again obtained.

5.4 EXAMPLES OF DATA.

The intent of this section is to present typical examples of the experimental data.

5.4.1 X Ray/mmW.

5.4.1.1 No Helium (Precursor) Layer Tests--Figure 24 presents a complete time series of the X-ray detection signal for HST 142, for which the X-ray voltage was 80 kV. Power-supply ripple is responsible for most of the apparent noise in the signal. This ripple is more apparent in Figure 25, where the noise spikes are also resolved. These spikes typically consist of one and one-half cycles of damped sinusoids centered about 2 kHz. Maximum X-ray absorption was reached at about T + 200 ms, and recovery to baseline level occurred at about T + 2.5 s. There was no significant X-ray baseline shift for this test.

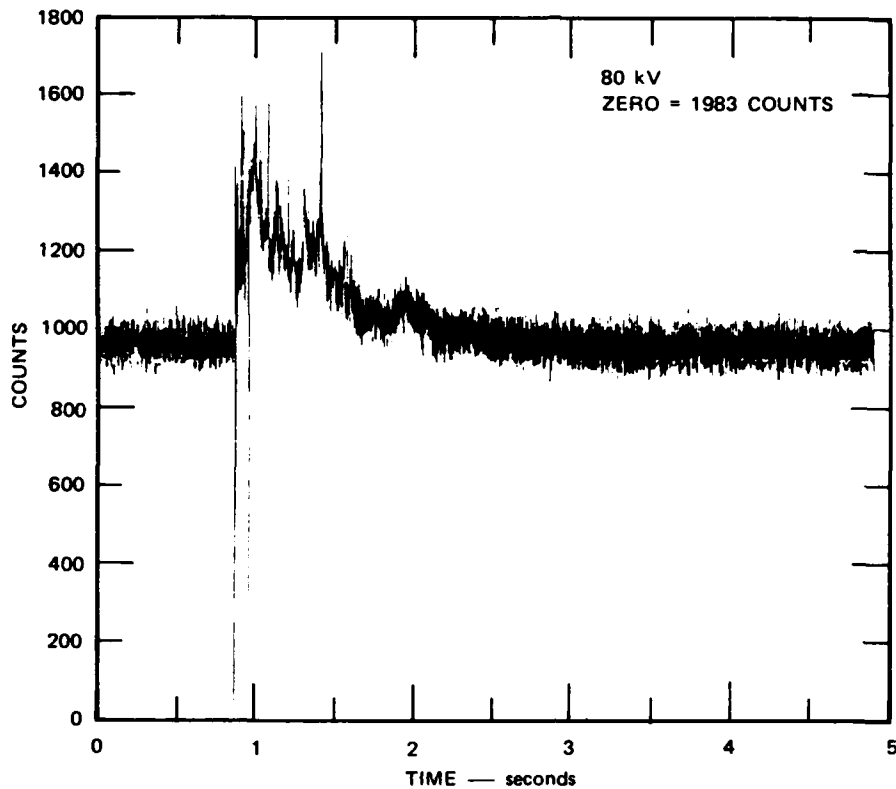


Figure 24. X-ray digitizer output vs time for HST 142.

Most of the artifacts in the X-ray data can be removed by means of simple filtering. Figure 26 shows the HST 142 time series of the logarithm of X-ray absorption after the following processing steps were applied:

- (1) Smoothing with a 2.1-ms-running average to reduce the noise spikes.
- (2) Zero-level subtraction and conversion to logarithmic form.
- (3) Bandstop filtering (center frequency = 120 Hz, bandwidth = 30 Hz) to reduce ripple.
- (4) Normalization to pre-event baseline intensity.

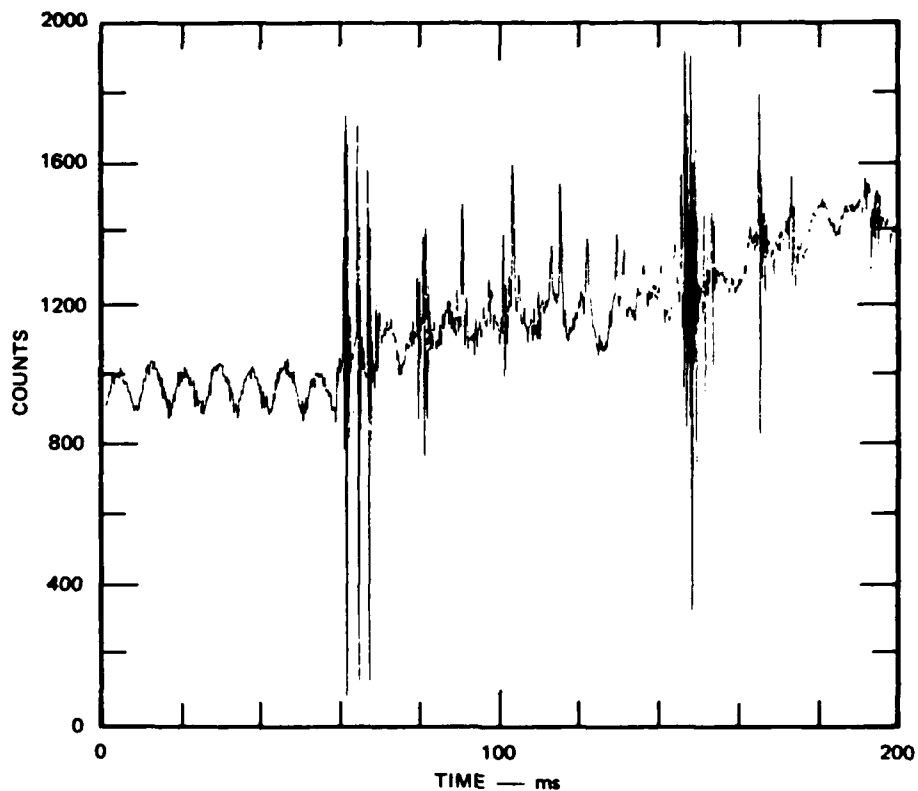


Figure 25. X-ray digitizer output vs time after T_0 for HST 142.

Unprocessed data from T_0 to $T + 200$ ms for HST 142 are shown in Figure 27. Phase lock was lost at $T + 140$ ms, but the mmW data were unaffected before that time (lock was reacquired at $T + 320$ ms). The phase-time series is clearly very different from the X-ray data. The mmW amplitude data are noteworthy because they were initially unaffected by the shock-wave passage. This is evidence that multipath was negligible because there was 90-deg phase shift of the direct signal during that time.

Similar X ray and mmW-phase behaviors were recorded on other nonprecursed tests. The complete HST 131 X-ray time series appears in Figure 28, and the T_0 to $t + 200$ ms processed X-ray signal

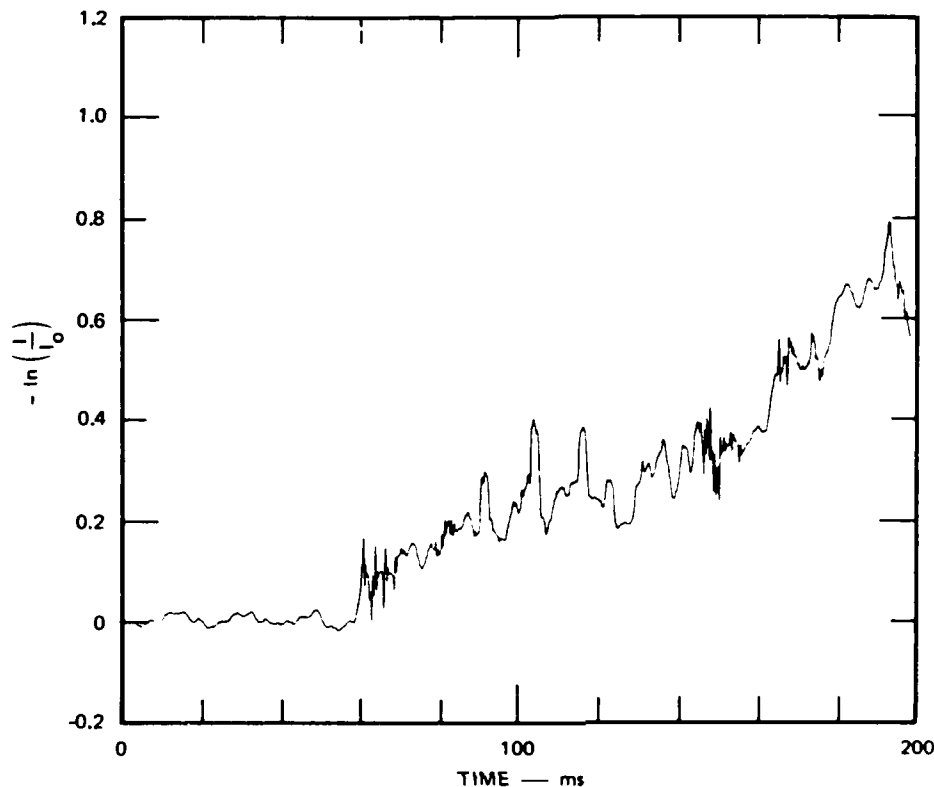


Figure 26. Processed X-ray data (absorption) vs time after T_0 for HST 142.

and mmW phase are shown in Figure 29. Figures 30 and 31 present the equivalent data from HST 144, for which the X-ray voltage was set to 40 kV.

These data reveal several problems. First, there was apparently a slight X-ray baseline shift for HST 131 between the pre-event level to that of postshot recovery. In addition, there were a large number of noise spikes in the X-ray detector output on that test, which was the first one on which data were acquired. A particularly severe group of spikes occurred at or possibly before the leading edge of the shock wave, which produced the artifact visible in Figure 28. Loss of mmW phase lock occurred on all three of these tests. Although lock was reestablished within the 200-ms ranges plotted in Figures 29

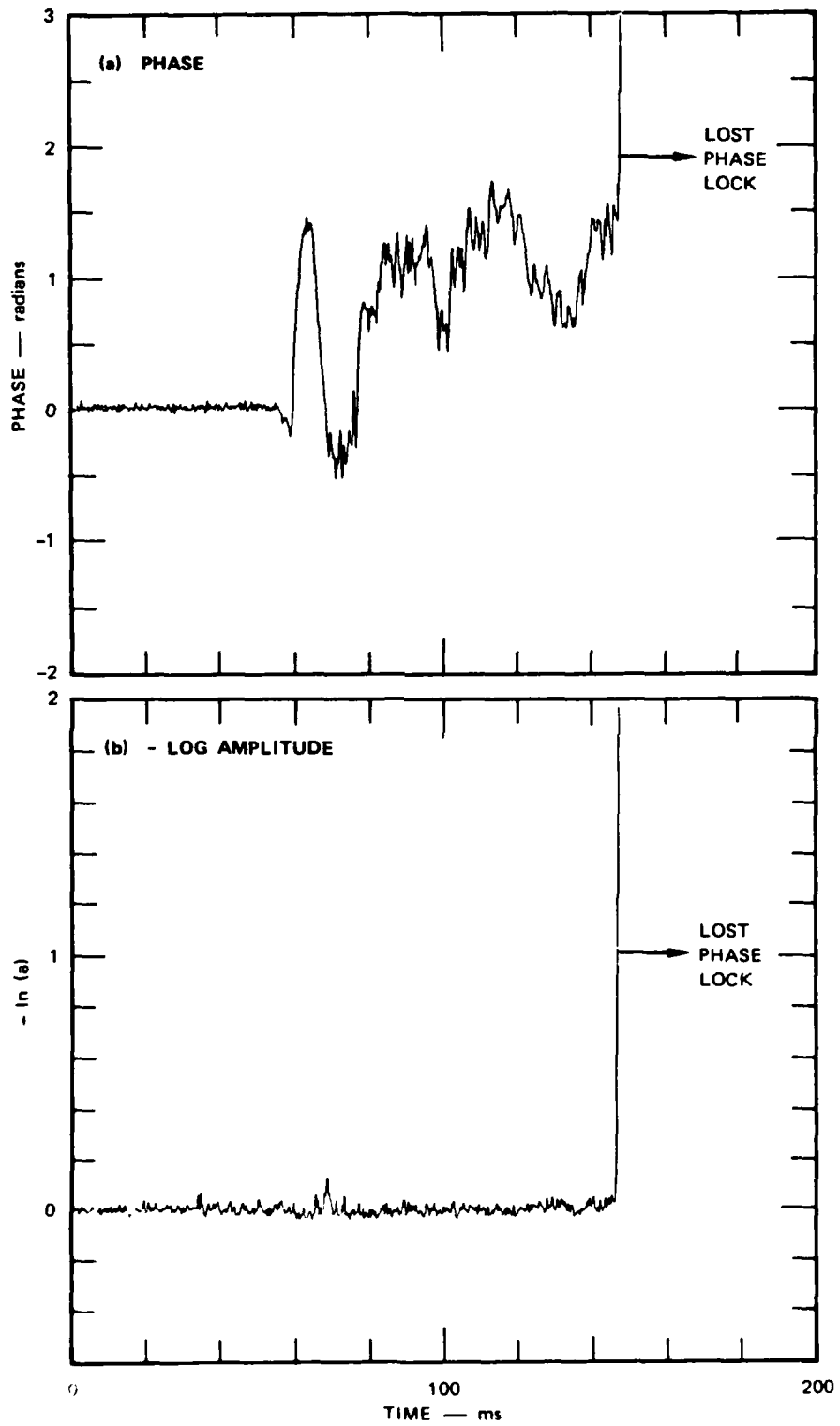


Figure 27 mmW phase and amplitude vs time after T_0 for HST 142.

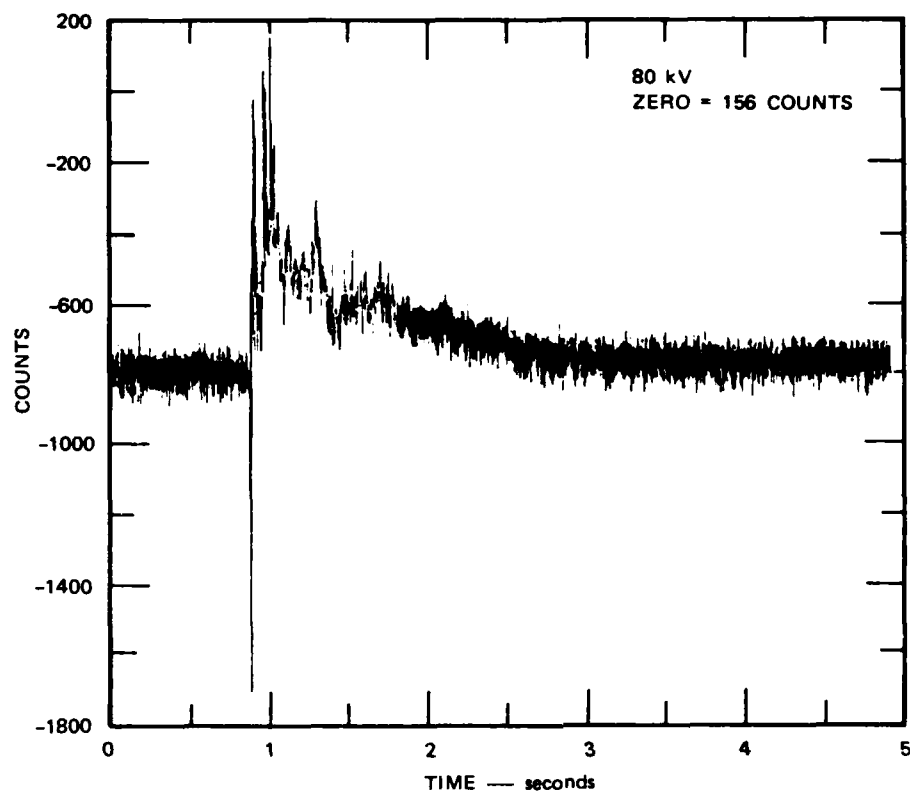


Figure 28. X-ray digitizer output vs time for HST 131.

and 31, the phase may not return to the same reference point because of the multiplicity of possible lock points resulting from the frequency division in the equipment. Finally, the amount of X-ray absorption for HST 144 exceeded the dynamic range of the measurement. The data plotted in Figure 31 are consequently invalid beyond $T + 150$ ms. We conclude that operation at 80 kV is superior to 40 kV for X-ray dust measurements for path lengths on the order of 1 to 2 m.

The mmW phase signals from these three nonprecursed tests exhibited consistent behavior: (1) an initial negative shift; (2) a positive impulse; (3) a continued negative trend; followed by (4), a positive trend with substantial fluctuations. Positive phase shift corresponds to increased density in the signal path or an increase in

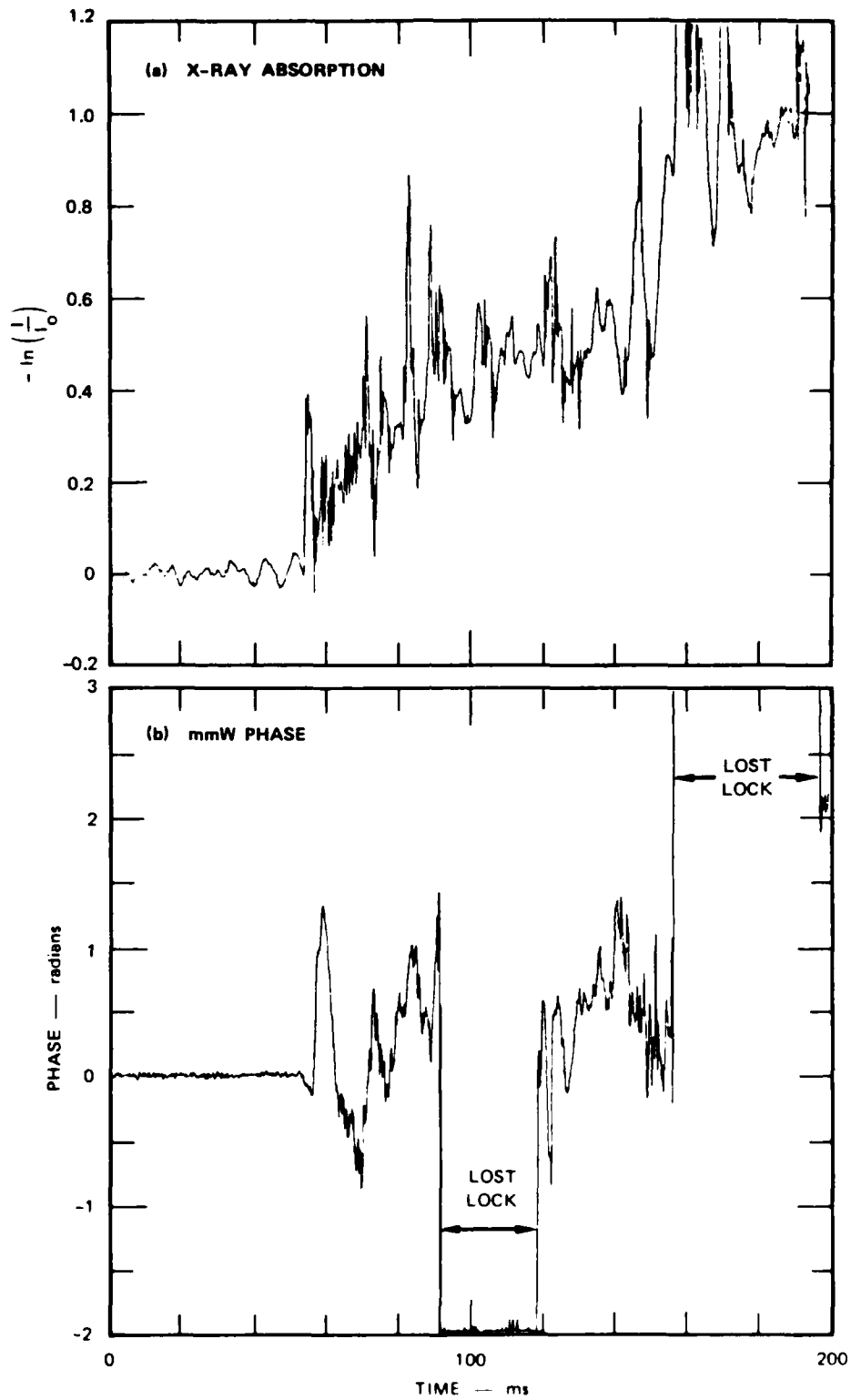


Figure 29. X-ray absorption and mmW phase vs time after T_0 for HST 131.

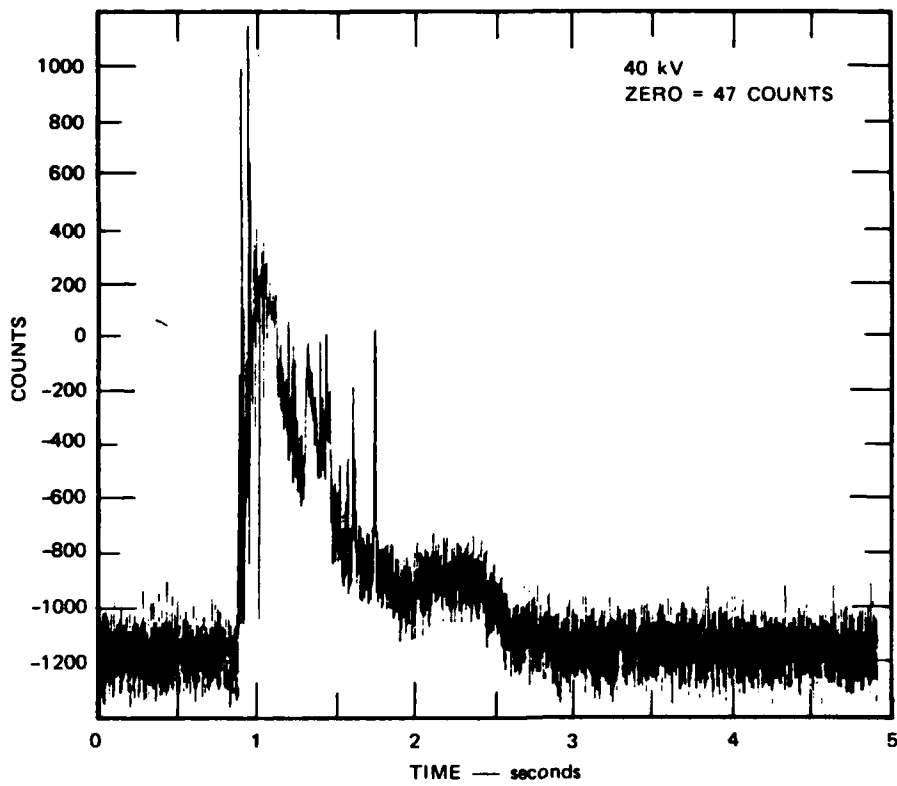


Figure 30. X-ray digitizer output vs time for HST 144.

the separation between antennas. The consistent initial negative phase shift corresponds to a shortening of the antenna spacing or a decrease in density and is apparently an artifact because it precedes any change in the X-ray signal. Because the phase shift computed for ambient conditions is approximately 0.3 radians, it is theoretically impossible to have more than a 0.3-radian negative phase shift in the negative phase of the shock wave. Thus at least part of the negative phase shift after the positive impulse appears to be an artifact as well. It may be a continuation of the initial negative trend, which appears to be due to some kind of outrunning wave motion in the shock-tube wall that squeezed the antennas together. The amount of squeezing required is about 1 mm, which is within the elastic strain limit.

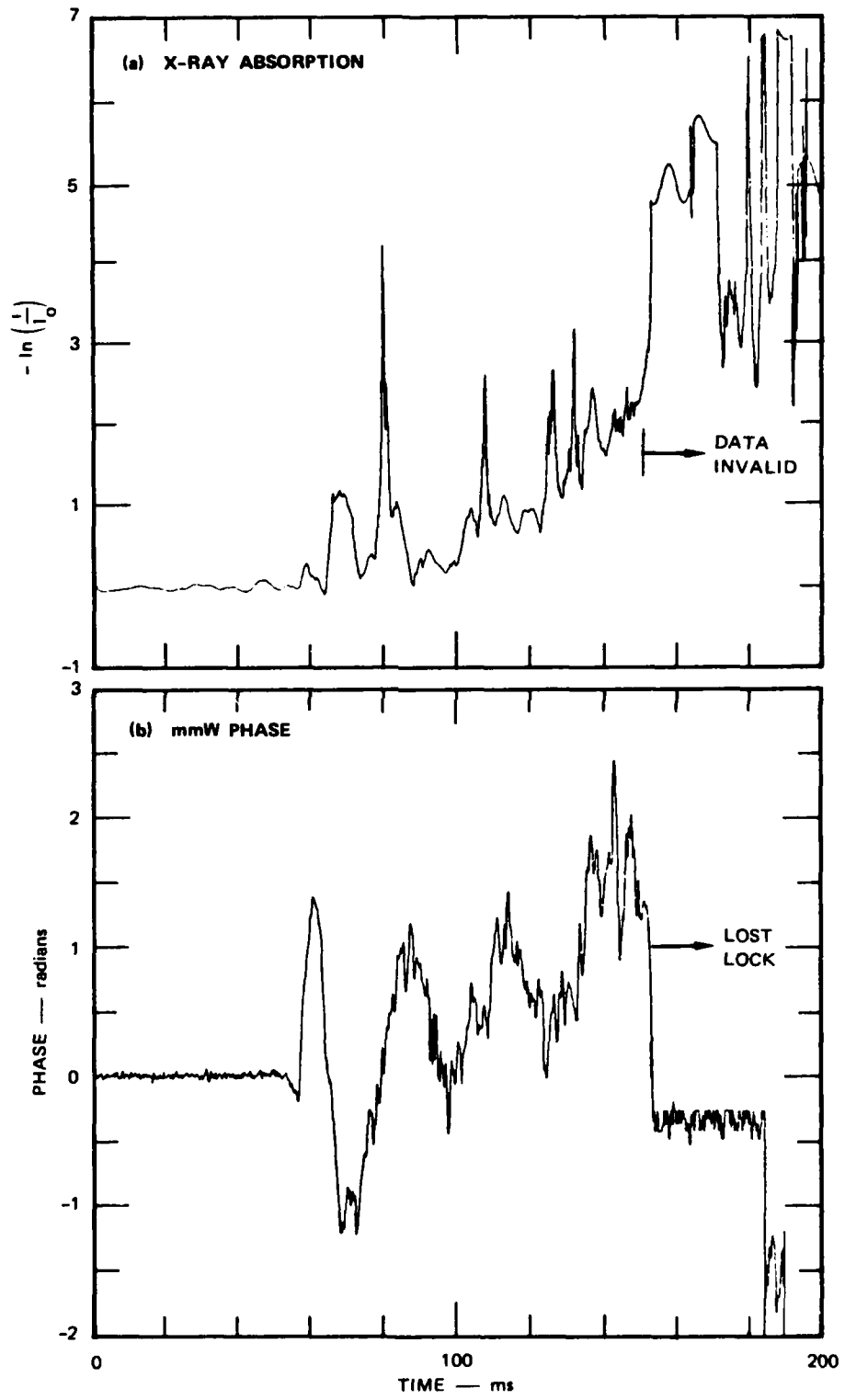


Figure 31. X-ray absorption and mmW phase vs time after T_0 for HST 144.

The accelerometer data provide strong evidence that at least the initial impulses seen in the phase data are artifacts caused by motion of the antennas. Figure 32 shows a typical accelerometer record, which, as described above, is contaminated by crosstalk

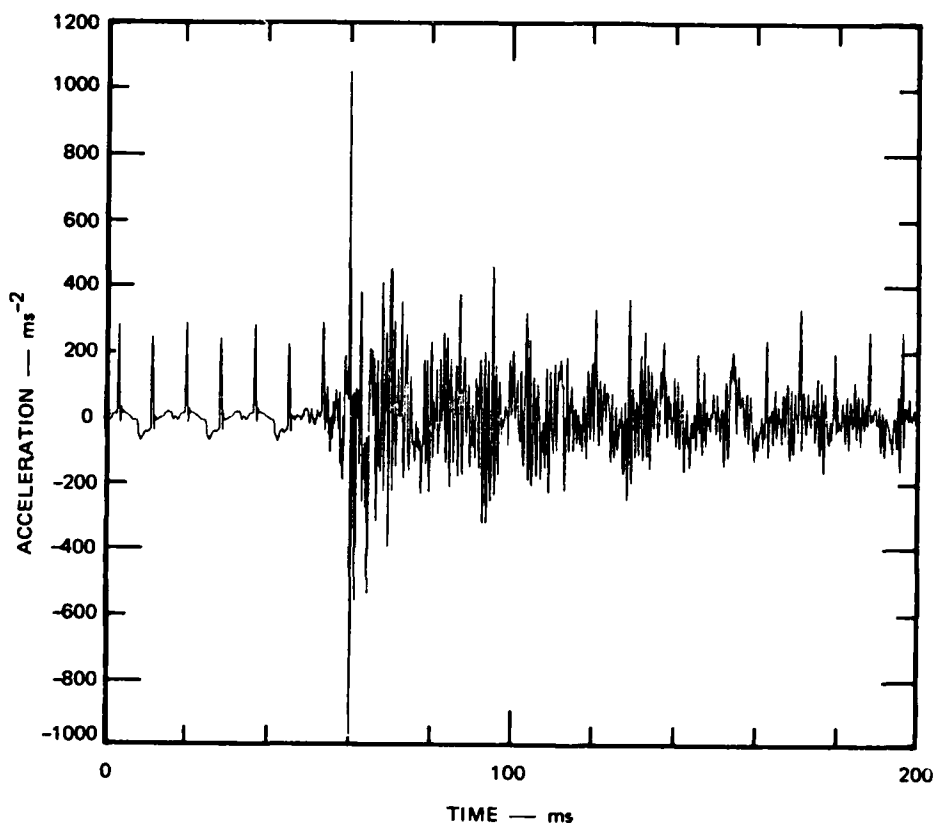


Figure 32. Receiver accelerometer data for HST 142.

apparently from the X-ray voltage and current monitors. The dominant feature in the accelerometer time series is the bipolar spike. Most of the acceleration appears to consist of high-frequency noise that would not be associated with much displacement of the antennas. By numerically integrating the accelerometer data twice, we can obtain a description of the antenna motion, which can be compared to the mmW phase. Because of the crosstalk and an apparently related irregularly varying offset from the dc zero level, a reasonably stable result from the numerical integration can be achieved only for short periods. Figure 33 presents the results from numerically integrating the

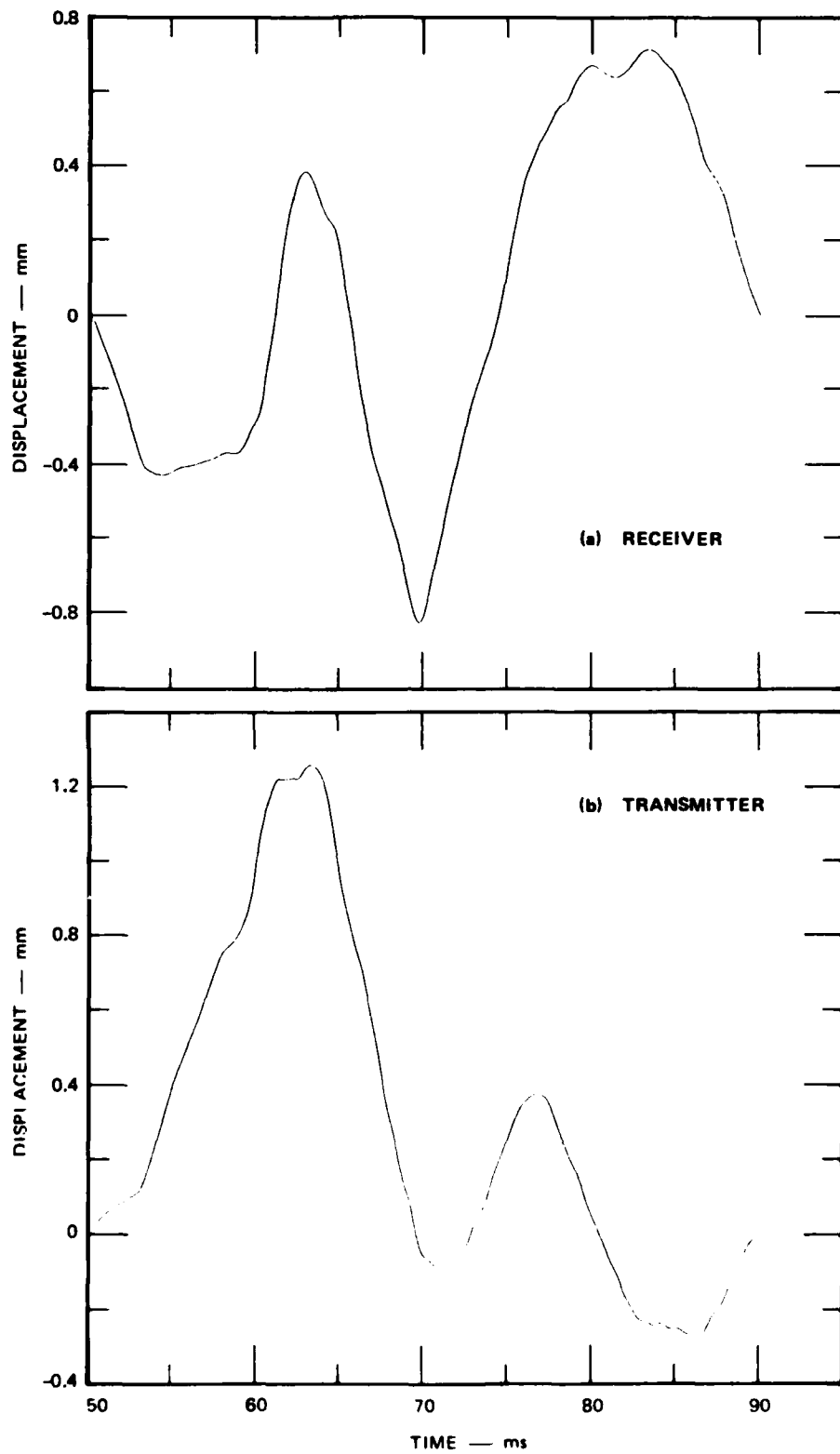


Figure 33. Doubly integrated accelerometer data from HST 142.

accelerometer data from HST 142 over a 40-ms interval (the mean values of both the acceleration and the velocity were set to zero over this interval before each step of the numerical integration). This may be compared to the phase shift record for the same time (Figure 34). It is clear that the timing and shape of initial impulse is the phase data mimicked in the integrated accelerometer data.

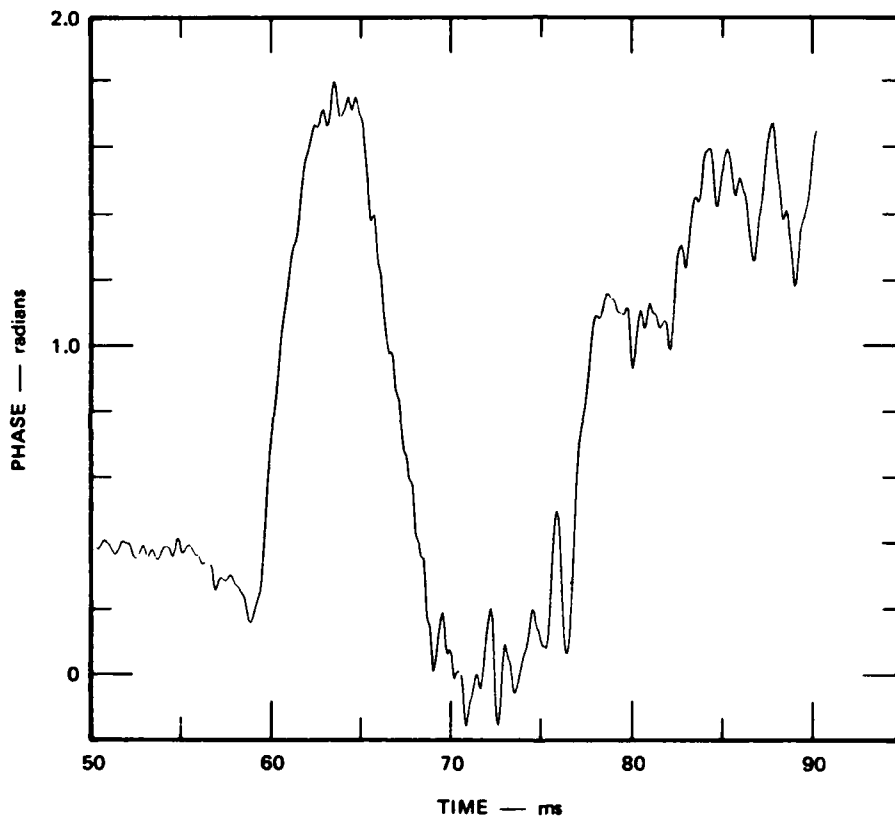


Figure 34. Phase vs time for HST 142.

The total rf signal path increase between the antennas can be obtained by adding the two antenna displacements of Figure 33. The peak value of path increase at $T + 62$ ms is 0.8 mm + 1.2 mm = 2.0 mm. This distance corresponds to a phase shift of 1.4 radians, which agrees fairly closely to the observed peak phase shift of 1.7

radians. Thus the initial impulse in the phase data agrees in all respects with that expected from measuring the motion of the antennas.

This impulse because of antenna motion appears to be the most significant artifact in the mmW phase data. It usually occurred before the X-ray system registered any increase in mass density, which is consistent with outrunning motion in the wall of the shock tube. Figure 35 shows the calculated displacement of one of the

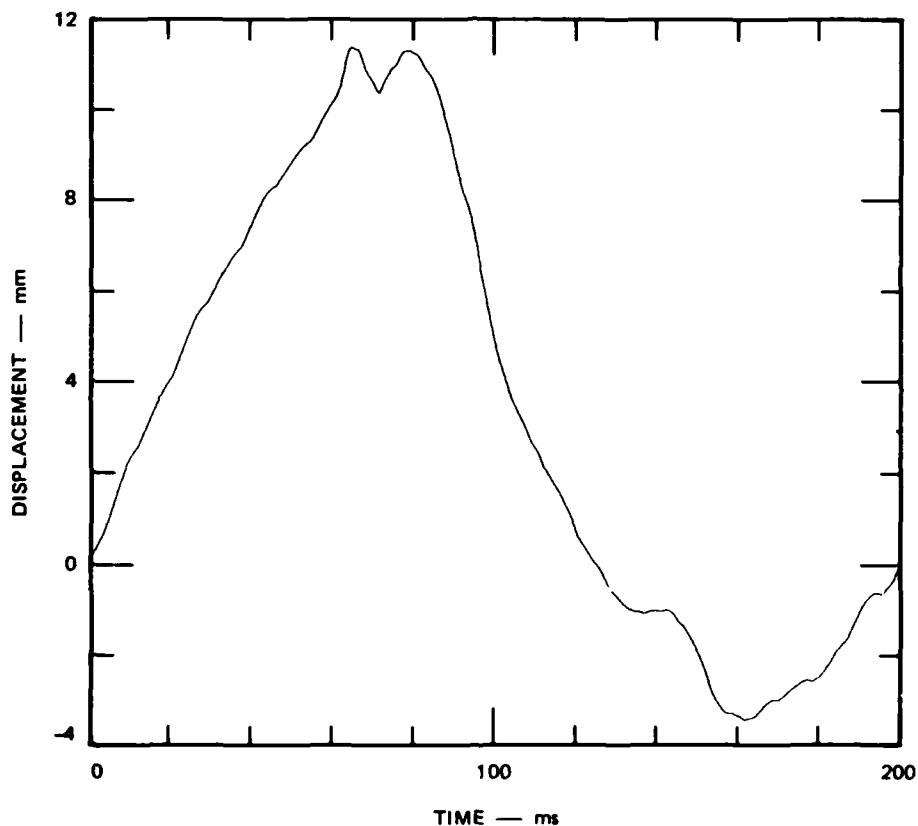


Figure 35. HST 142 receiver antenna displacement computed from accelerator data.

antennas over a longer, 200-ms period. Although this record is dominated by the slowly varying contaminating signal, it is apparent that there may have been further displacements comparable to the initial impulse.

The choice of mounting the mmW antennas to the shock tube is in retrospect a poor one. Expansion of the tube was 50 times greater than expected (i.e., 2 mm versus 0.04 mm). The solution is to mount the antennas on supports that do not contact the wall of the shock tube. We note that this effect was not observed during the MINOR SCALE test, where the mmW antennas were mounted securely in supports anchored in concrete.

5.4.1.2 Tests with a Helium Layer (Precursed)--Two tests (HST 141 and HST 143) were done with a helium layer, which was 5 in. deep so that the X-ray and mmW line of sight passed about 2.5 cm below the top of the layer. Results from these two tests are presented in Figures 36, 37, 38, and 39.

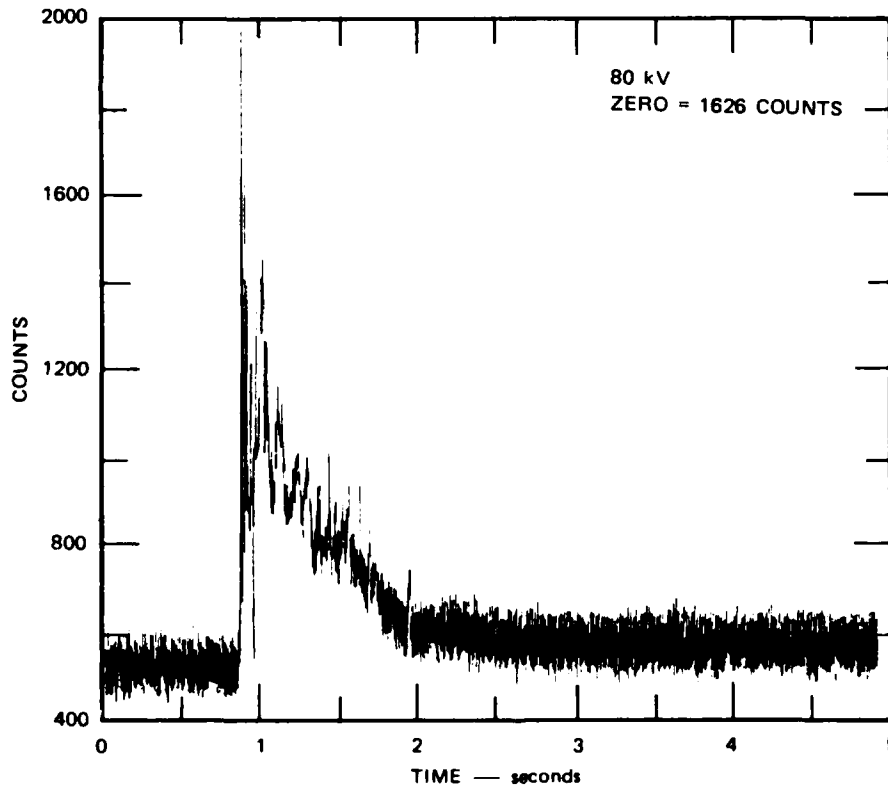


Figure 36. X-ray digitizer output vs time for HST 141.

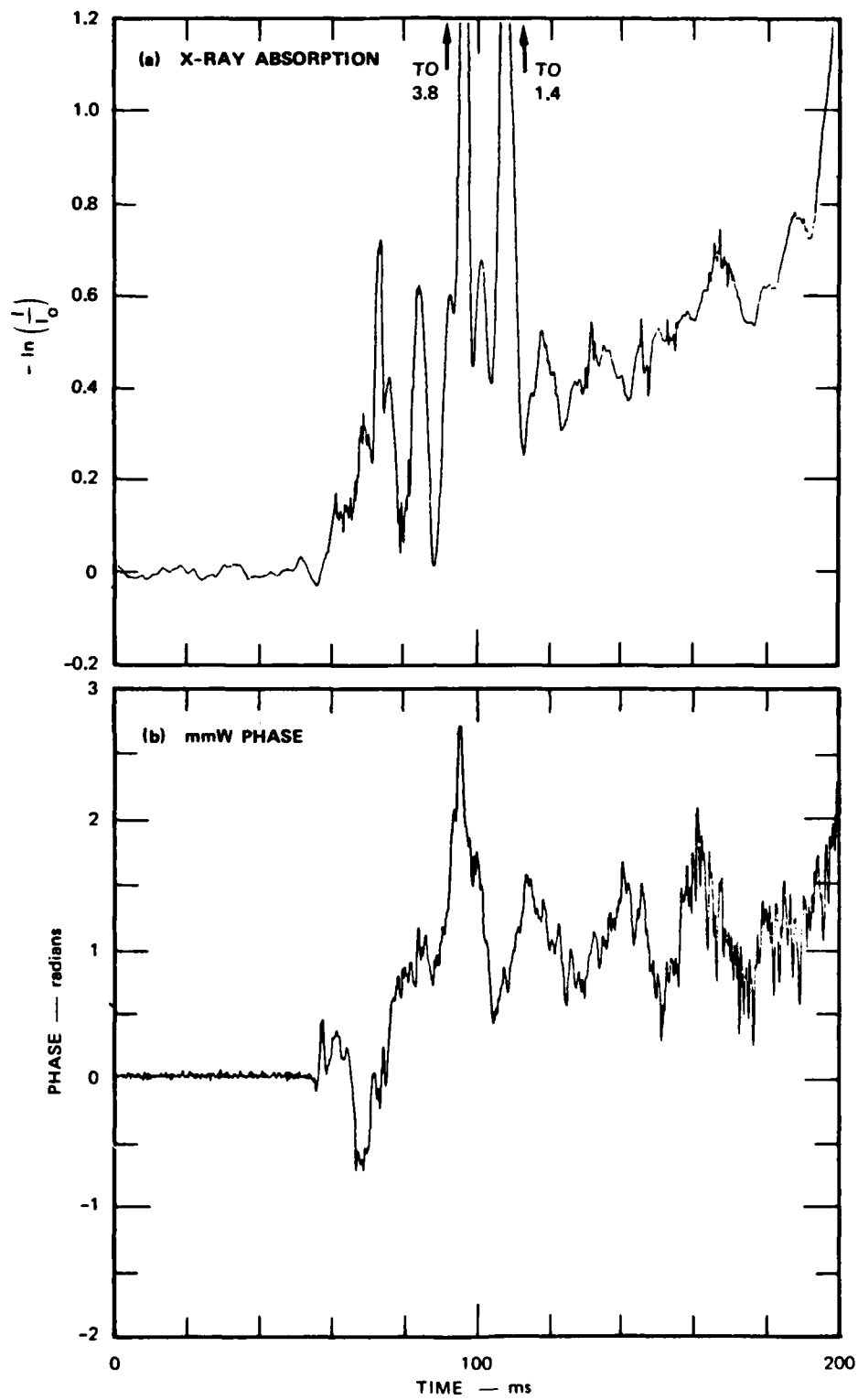


Figure 37. X-ray absorption and mmW phase vs time for HST 141.

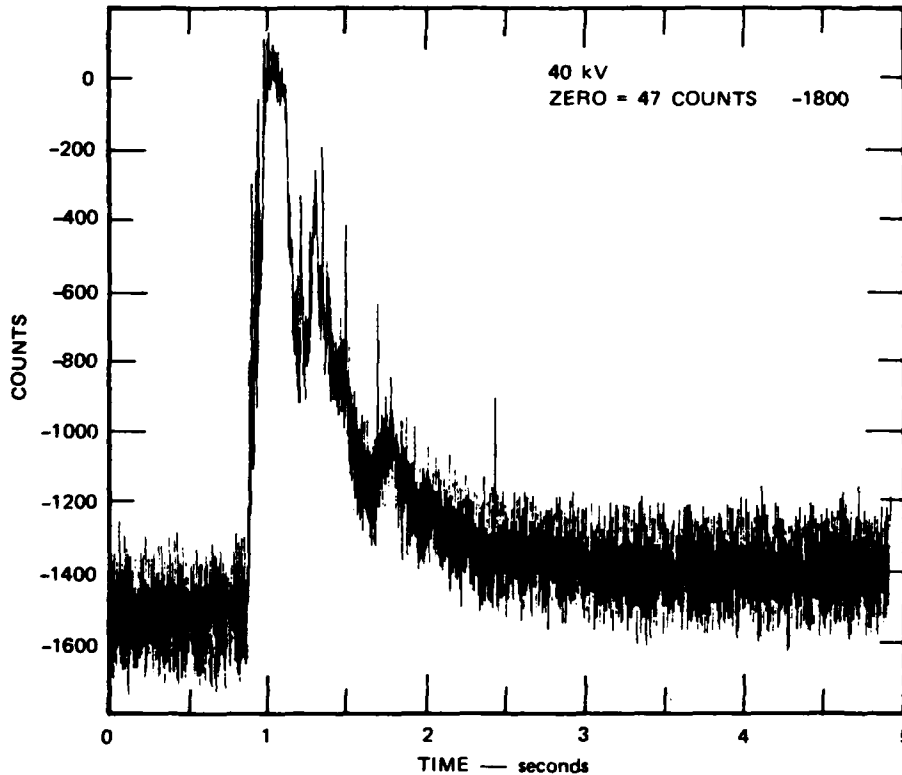


Figure 38. X-ray digitizer output vs time for HST 143.

The apparent baseline shifts between the pre- and post-shot X-ray detector signals are not necessarily artifacts because an increase in X-ray absorption is to be expected after the test, when air replaces the helium/air mixture. However, the change in absorption from a helium/air mixture to air and possible baseline shifts may mask one another. Although, there were no perceptible changes in the X-ray voltage and current monitors for either test. In Table 5, we compare the inputted change in absorption from the data. In developing this table, we have assumed no baseline shift to the theoretically computed absorption assuming a 90-percent helium mass fraction, which was the target value for the precursed tests. The inputted values of absorption are 27-percent higher than computed for 80 kV and 53-percent higher at 40 kV. Several factors may contribute to this discrepancy:

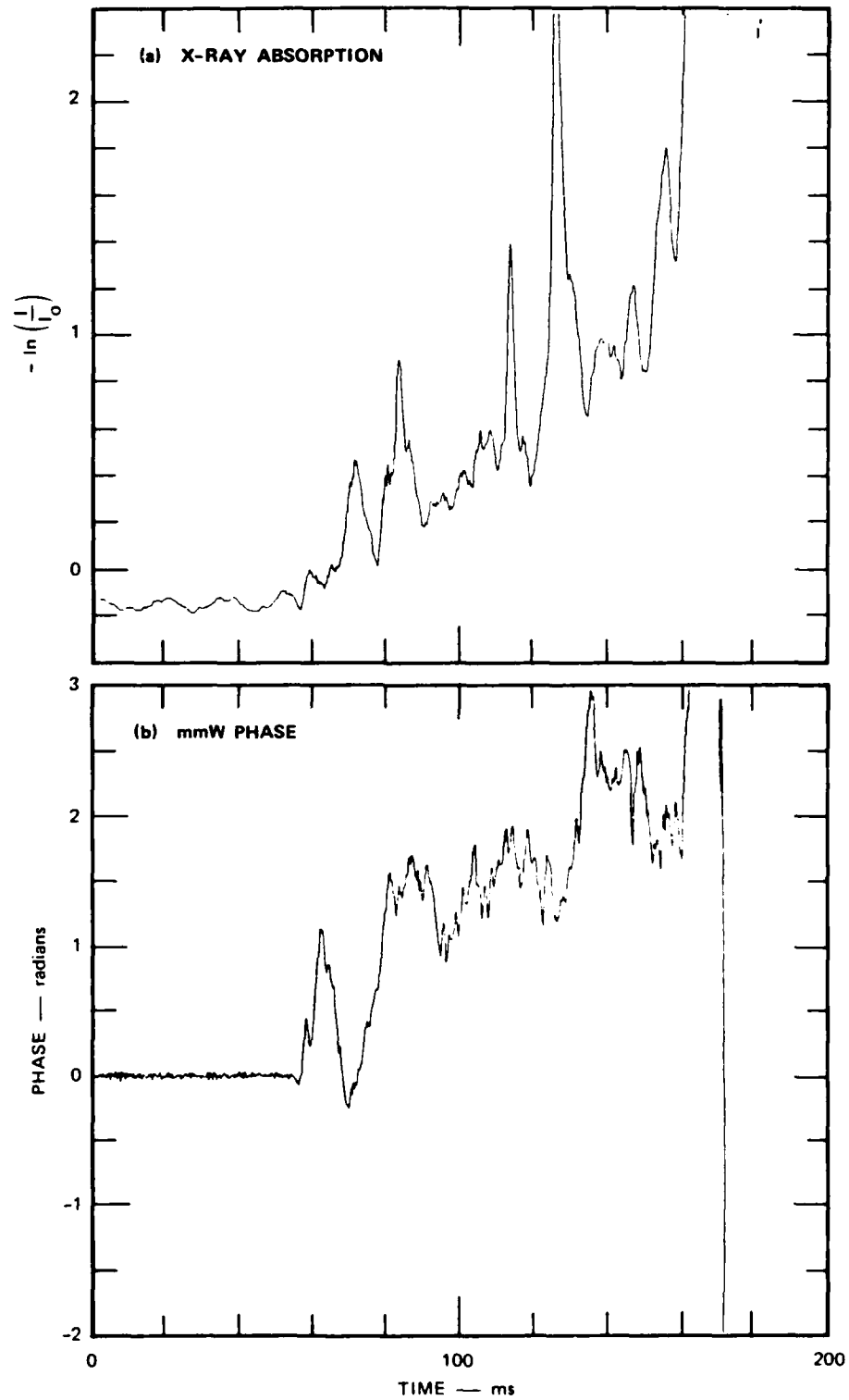


Figure 39. X-ray absorption and mmW phase vs time after T_0 for HST 143.

Table 5. Analysis of pre- to post-shot X-ray absorption changes for tests with a helium precursor.

Test	X-Ray Voltage (kV)	X-Ray Detection Output-Counts			X-Ray Absorption	
		Preshot	Postshot	Zero	Inputed	Computed
HST 141	80	527	577	1626	0.047	0.037
HST 143	40	-1513	-1391	47	0.081	0.053

- (1) Softer X-ray spectra for the tests, especially at 40 kV, leading to higher absorption coefficients than were obtained from calibration runs.
- (2) Longer effective path lengths caused by helium leaking into and filling the spaces between the X-ray tube and detector and the wall of the shock tube. This would increase the effective path length from 163 cm to 193 to 208 cm, or by 18 to 28 percent.
- (3) Subtle shifts in X-ray voltage and current that could not be detected in the monitored signals (no voltage or current shifts could be seen in the HST 131 records, for example, even though there was a baseline shift).
- (4) Higher helium concentrations than the 90-percent target.

The precursed results differ from the nonprecursed ones in two primary ways. First, the precursed X-ray absorption increased more rapidly and attained greater values than the nonprecursed. It also rose in closer time coincidence than for the nonprecursed tests, in which X-ray absorption tends to lag the mmW phase shift by the duration of the initial positive phase impulse. Because the X-ray absorption is relatively more sensitive to dust than air, than is the mmW phase shift, this suggests that dust was entrained in the leading edge of the precursed shock wave and that more dust was indeed present in the precursor layer. The second difference is that the X-ray absorption

AD-A182 628

FLOW-FIELD INSTRUMENTATION DEVELOPMENT(U) SRI
INTERNATIONAL MENLO PARK CA A A BURNS 30 AUG 86
DNA-TR-86-389 DNA001-84-C-8439

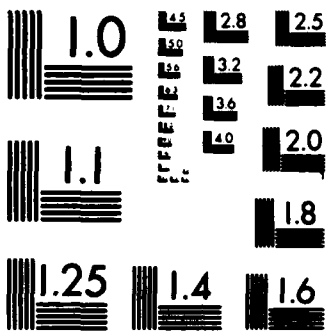
2/2

UNCLASSIFIED

F/G 28/4

ML

						END							
						B-87							
						D TIC							



MICROCOPY RESOLUTION TEST CHART
NATIONAL BUREAU OF STANDARDS-1963-A

the mmW phase shift was attenuated in the precursed shock wave. This result is especially apparent for HST 141 (Figure 37). It appears that increased dust loading or changes in the shock wave because of the presence of the helium layer reduced the severity of the mechanical effects.

5.4.1.3 Late-Time Behavior--After the mean air density has returned to its ambient value during the recovery phase, the mmW phase and log X-ray signal should respond only to changes in dust density and therefore track one another. This expectation is confirmed by the test results, examples of which are shown in Figures 40 and 41. These data are useful for verifying the dust calibration values, as discussed above.

5.4.1.4 Air- and Dust-Density Estimation--The artifacts introduced into both the mmW phase and the X-ray absorption data by mechanical effects experienced during this first set of system tests make it impossible to separate them accurately and reliably into mean dust and air density values. Figure 42 presents an example of the results of attempting this, for the HST 142 data. This separation is based on the following set of calibration factors:

$$f = 0.240 \text{ cm}^3/\text{g}, F = 0.25 \text{ cm}^2/\text{g}$$

$$g = 0.44 \text{ cm}^3/\text{g}, G = 1.036 \text{ cm}^2/\text{g} \quad .$$

The value for G is the revised value obtained by modifying that presented in Table 3 to force the mean air density at late times to match the ambient value (or at least to remain constant).

For comparison, Figure 43 shows the record obtained from a nearby, slightly upstream static pressure gauge. mmW and X-ray data were obtained during the positive phase of the shock wave before

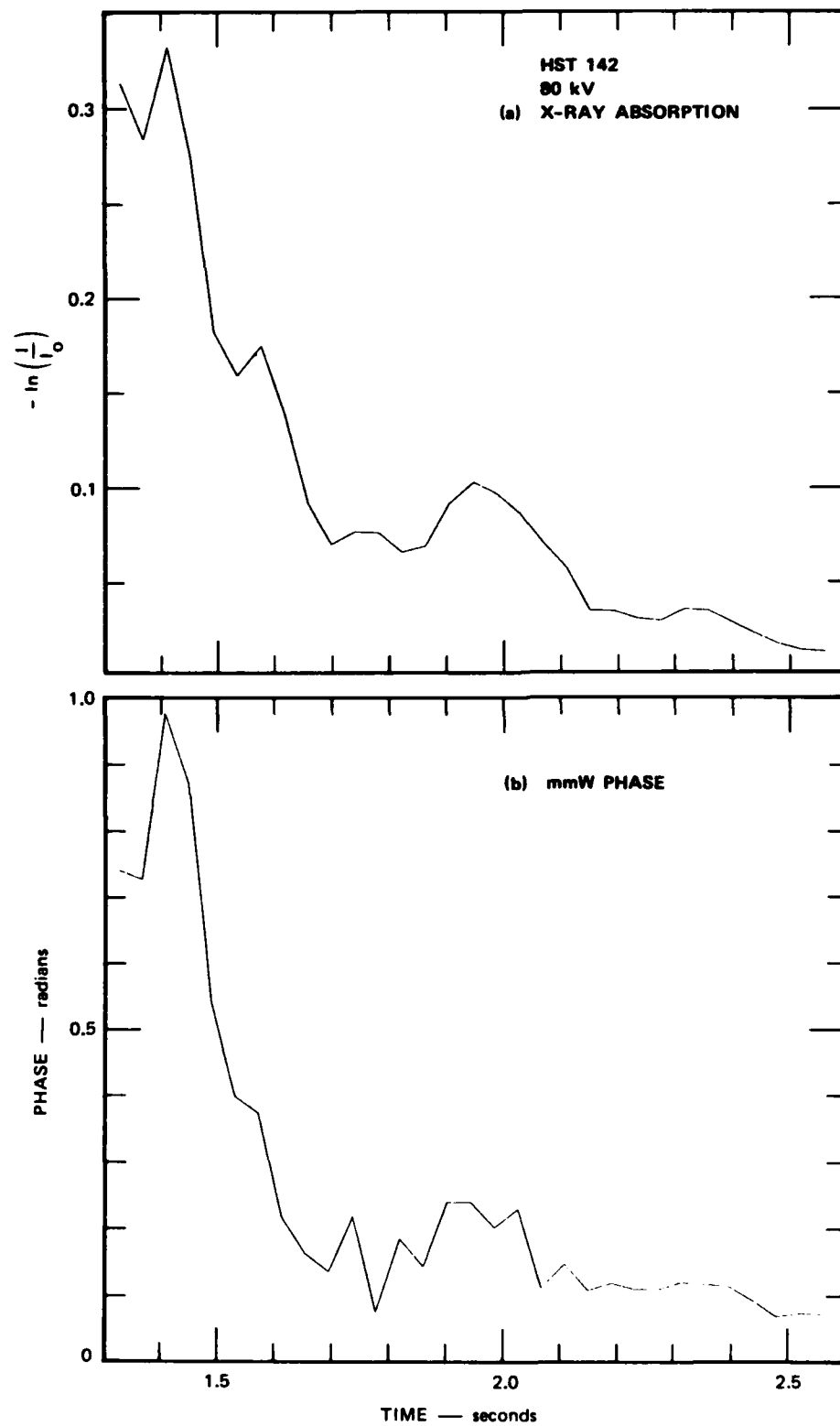


Figure 40. Late-time X-ray absorption for HST 142. These data have been smoothed with a 42-ms running average.

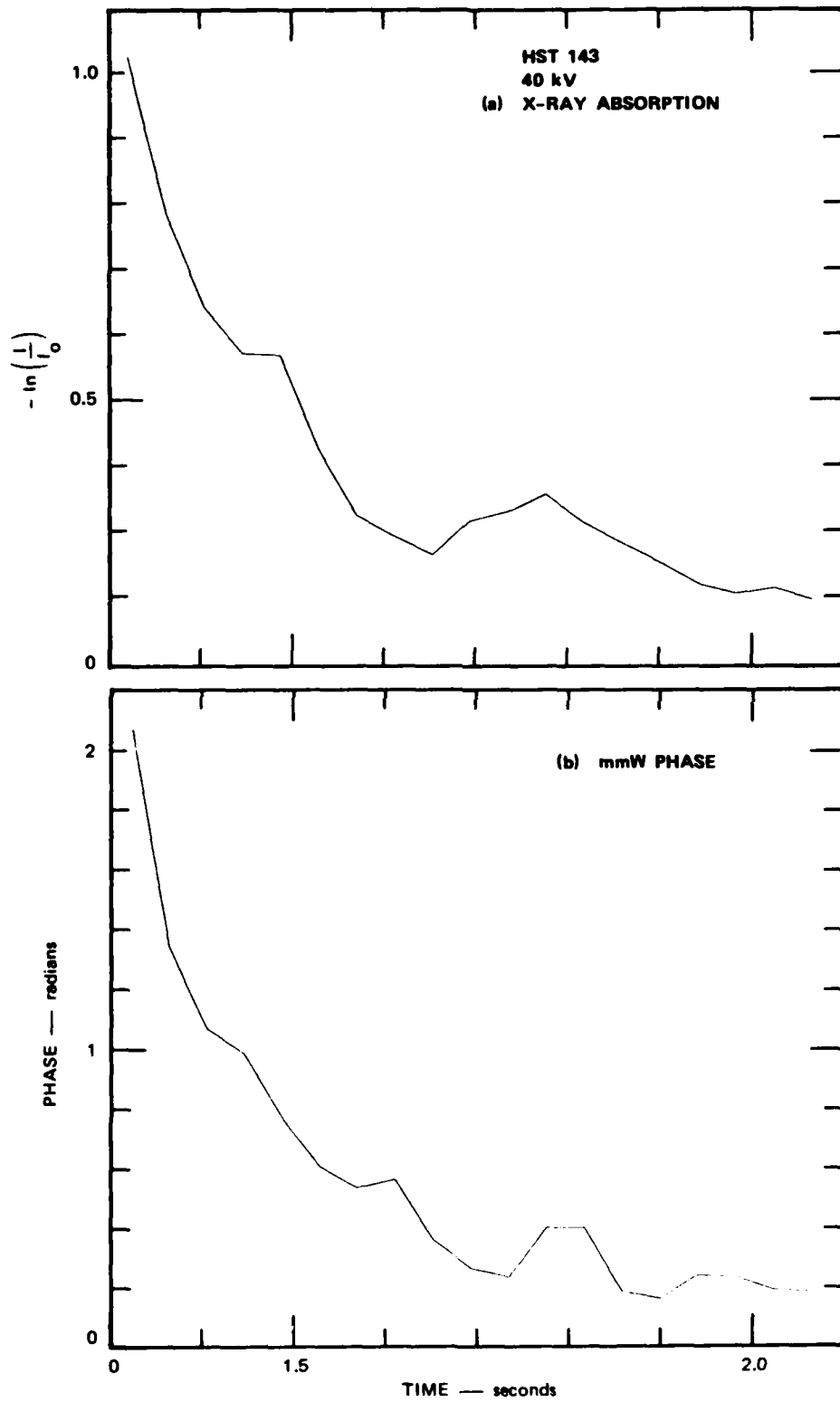


Figure 41. Late-time X-ray absorption for HST 143. These data have been smoothed with a 42-ms running average.

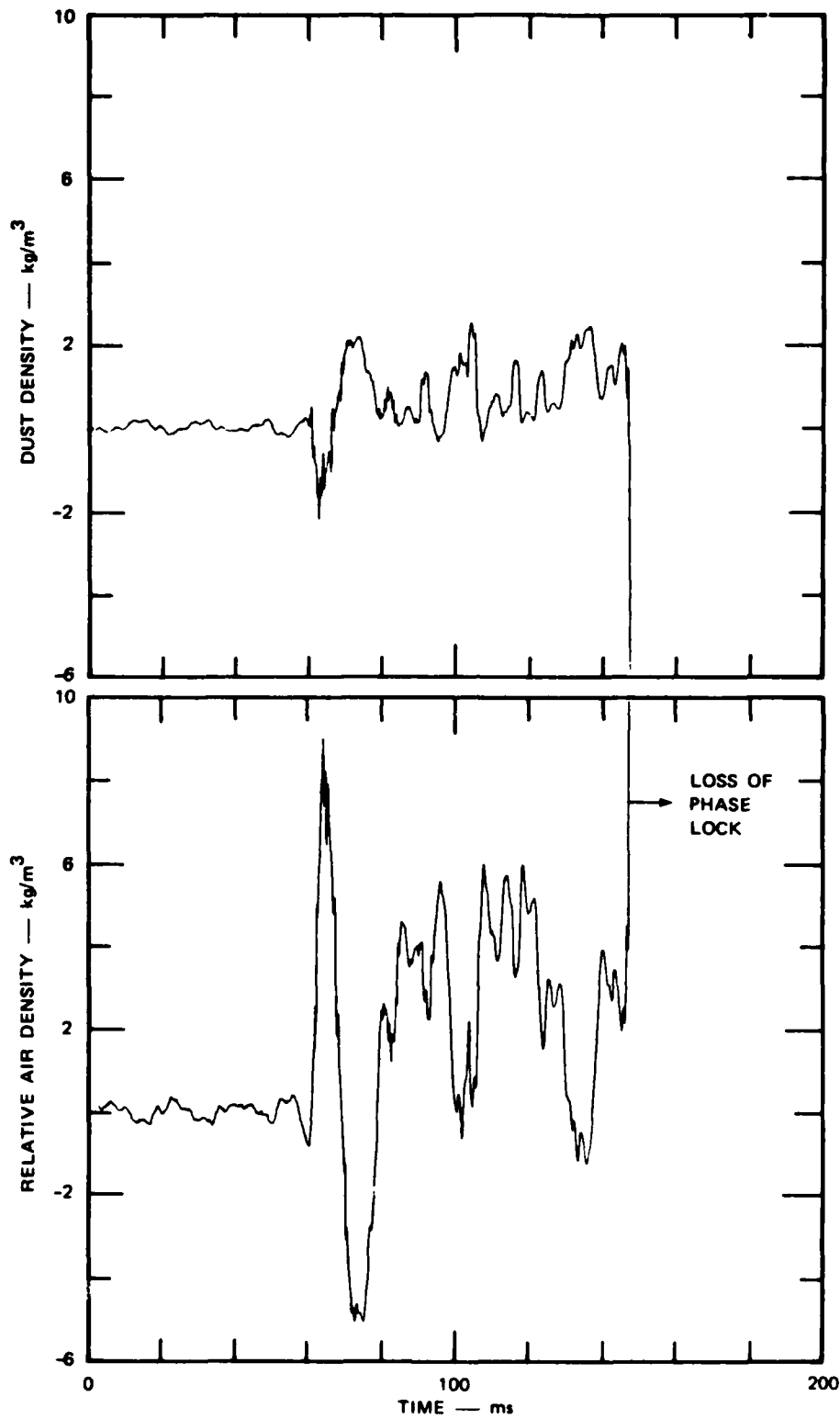


Figure 42. Relative estimates of air and dust densities for HST 142.

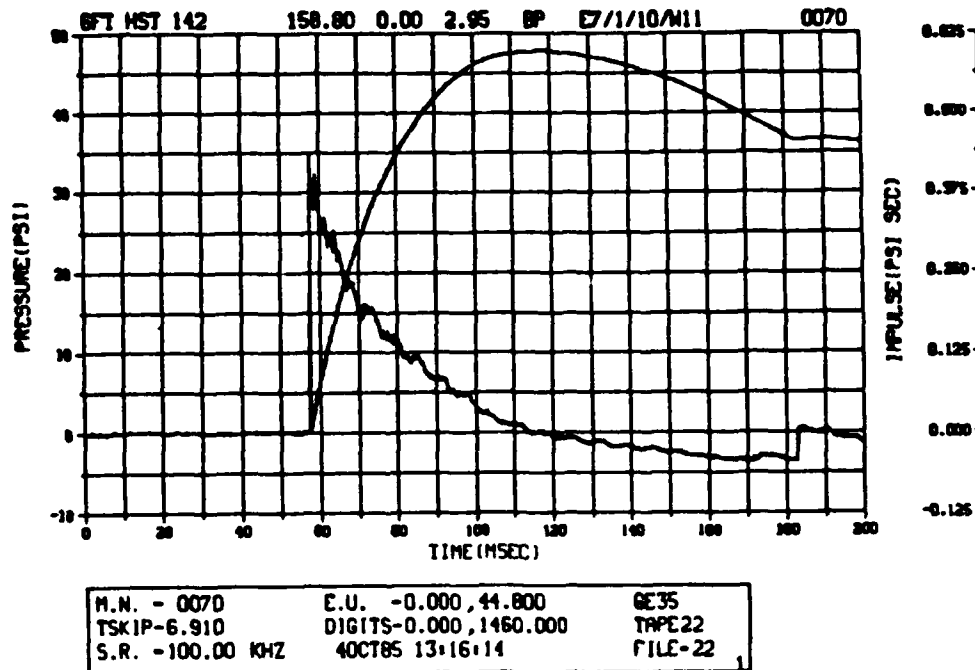


Figure 43. Static overpressure measured at HST 142.

the mmW lost phase lock. It is apparent that artifacts in the mmW phase data swamped the true air density variation, which should have behaved more or less as the pressure. These artifacts also masked the dust density variations, although the trend toward greater dust loading, as expected from the X-ray absorption data above (Figure 26) is preserved. The general trend in the air density estimate appears, subjectively, to be falling.

Artifacts in the mmW phase data tend to have a greater effect on the air-density estimate than on that for dust because the relationships between phase shift owing to air and dust are more nearly equal than are the equivalent ones for X-ray absorption. It appears that there were two components to the mmW phase artifacts because of antenna motion: a general outward bulge and an approximately 36-ms period oscillation.

The sum of the estimates for air and dust densities estimates is shown in Figure 44. This quantity is less sensitive to

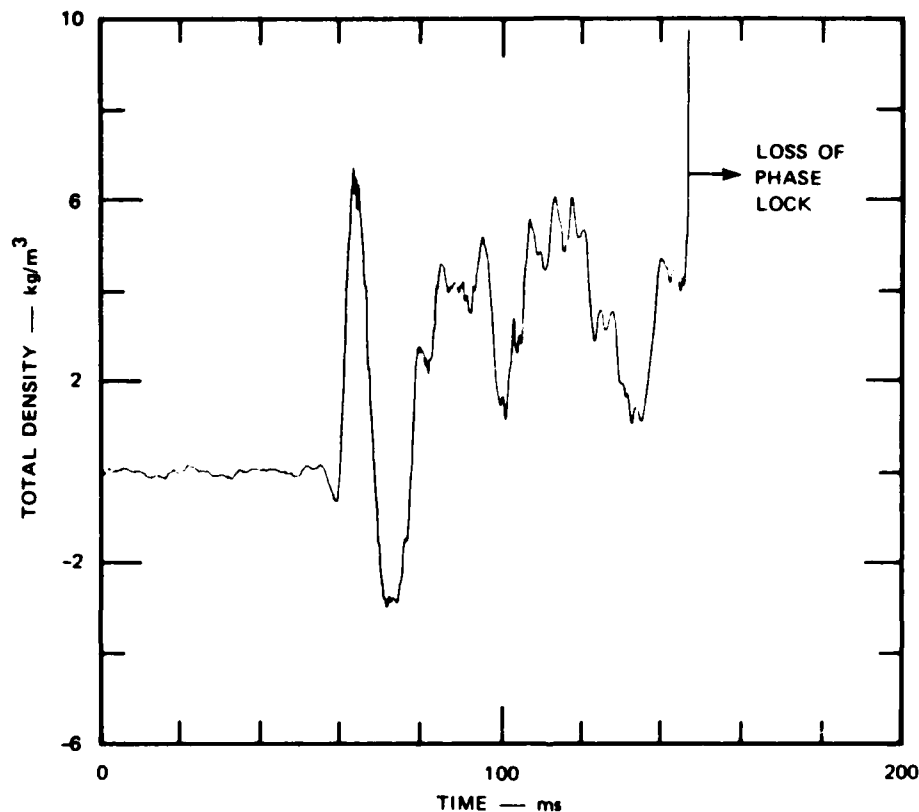


Figure 44. Sum of relative estimates of air and dust densities for HST 142.

relative errors in the calibration factors for phase shifts and X-ray absorption than are either the air or the dust density component alone-- an overestimate in one component is partly compensated by an underestimate in the other one.

Assuming that the actual relative change in air density was zero at $T + 120$ ms, all of the X-ray absorption should be due to dust. The measured X-ray absorption of $\ln(I/I_0) = -0.6$ at $T + 120$ ms for HST 142 corresponds to a dust density of $(0.6)/(163 \times 1.036) = 3.6 \times$

10^{-3} g/cm^3 . This is slightly below the estimate of the total density presented in Figure 44.

5.4.2 Surface Recession.

Figures 45 and 46 present examples of complete data sets for tests with (HST 143) and without (HST 144) a helium layer. These results were calculated, according to Eqs. (29a) and (29b), from the in-phase and quadrature signal pairs, which are the digitized quantities. The phases were also processed using an algorithm that attempts to remove the 360-deg jumps that occur when the arguments of the arc-tangent function cross the negative in-phase component axis. Especially when both amplitudes of the quadrature components are weak, the algorithm occasionally misses a 2π jump or inserts an extra one. Some of the phase records in Figures 45 and 46 exhibit this phenomenon.

A negative phase shift corresponds to a shortening of the electrical path length, which may be produced by either a reduction in the geometrical path length or a decrease in the dielectric constant of the soil. Most of the data exhibit an initial decrease in path length followed by an increase, which is interpreted as being caused by recession of the surface followed by a rebound to a higher level. Figure 47 shows the details of this process, which may be compared to the pressure record shown in Figure 43 (the HST 142 pressure record of Figure 43 is essentially the same as for HST 144). There was an initial 0.5-cm recession of the surface followed by a slow recovery as the positive overpressure decayed. The surface quickly rebounded to a level 1.9 cm higher than the original one at the onset of the negative phase. These height change values and the scale on the right-hand side of the Figure 47 phase record are based on a soil refractive index of 1.95 and a 51-deg incidence angle in Eq. (33). This refractive index corresponds to a soil density of 1.65 g/cm^3 for shock-tube material and application of the Rayleigh Mixing Rule. In the long term, the surface in this example returned to an eventual level of 1.3 cm [Figure 45(c)].

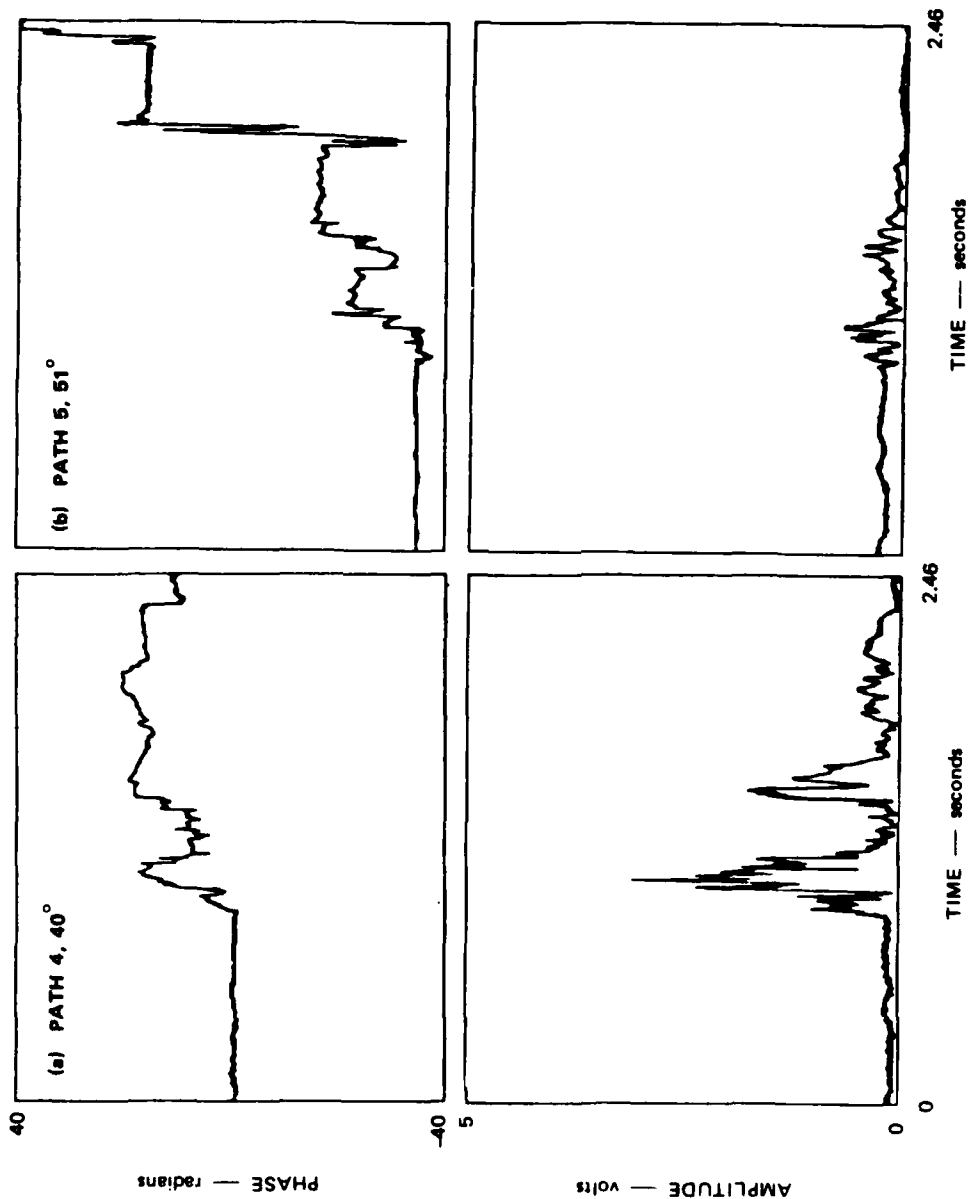


Figure 45. HST 143 amplitude and pulse records.

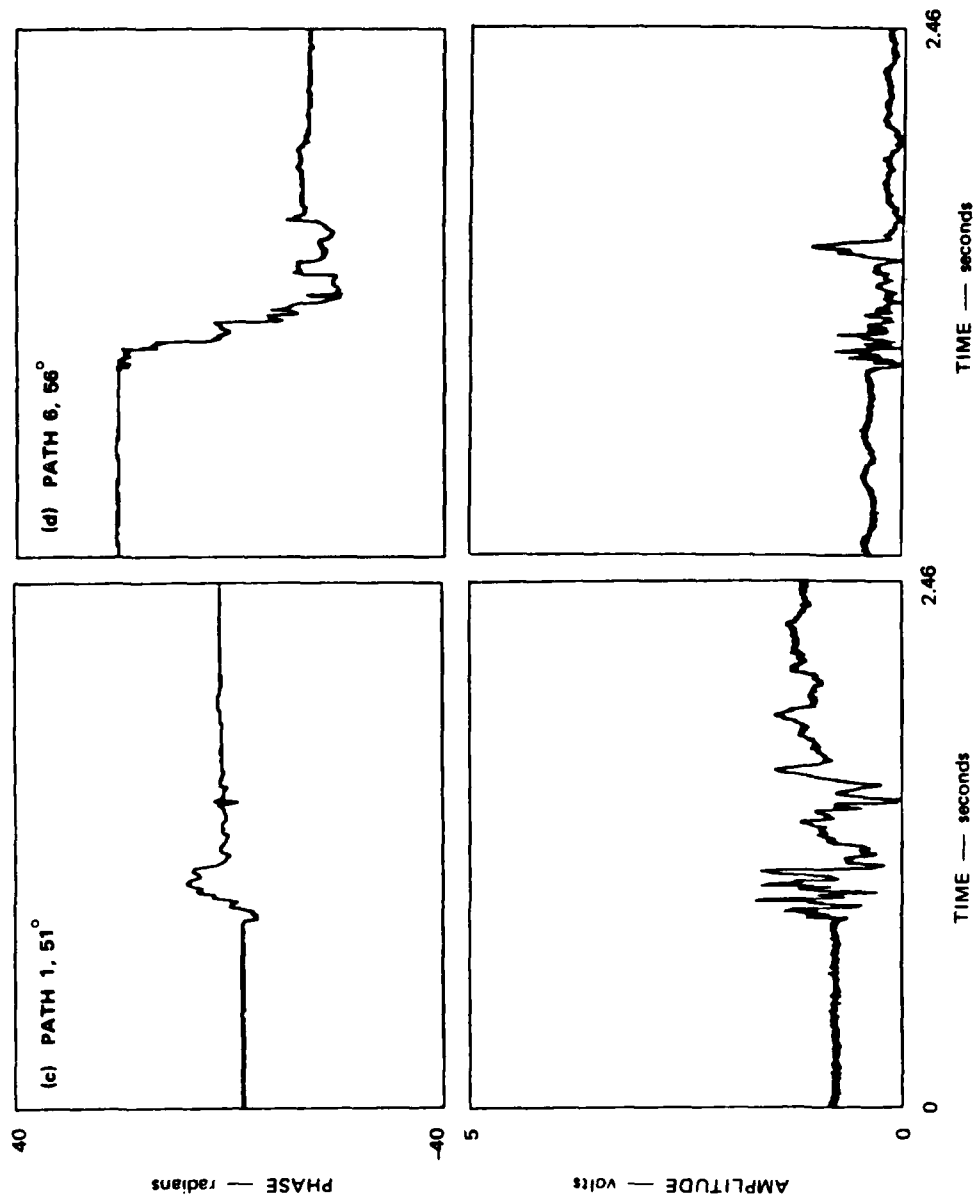


Figure 45. HST 143 amplitude and pulse records (Continued).

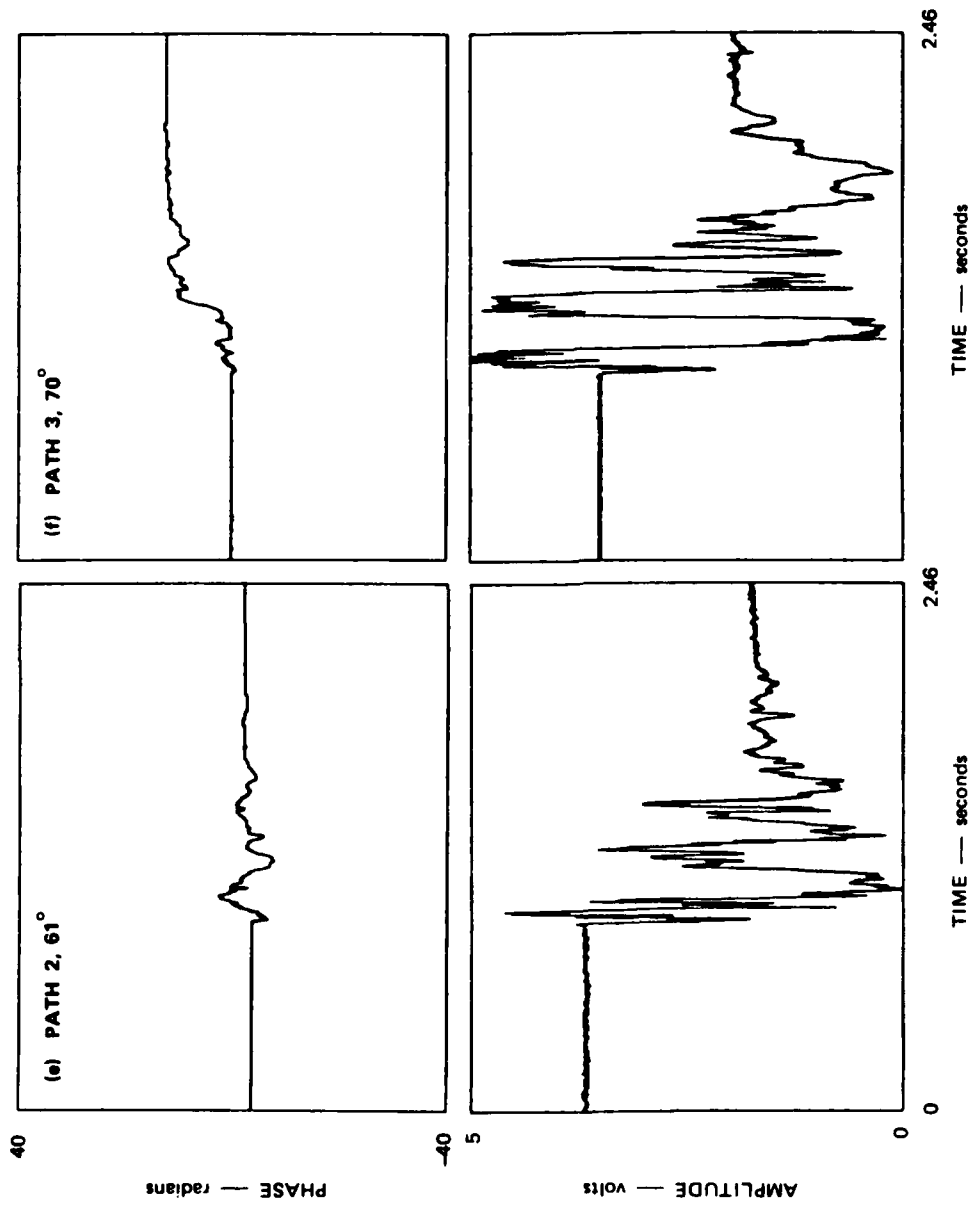


Figure 45. HST 143 amplitude and pulse records (Concluded).

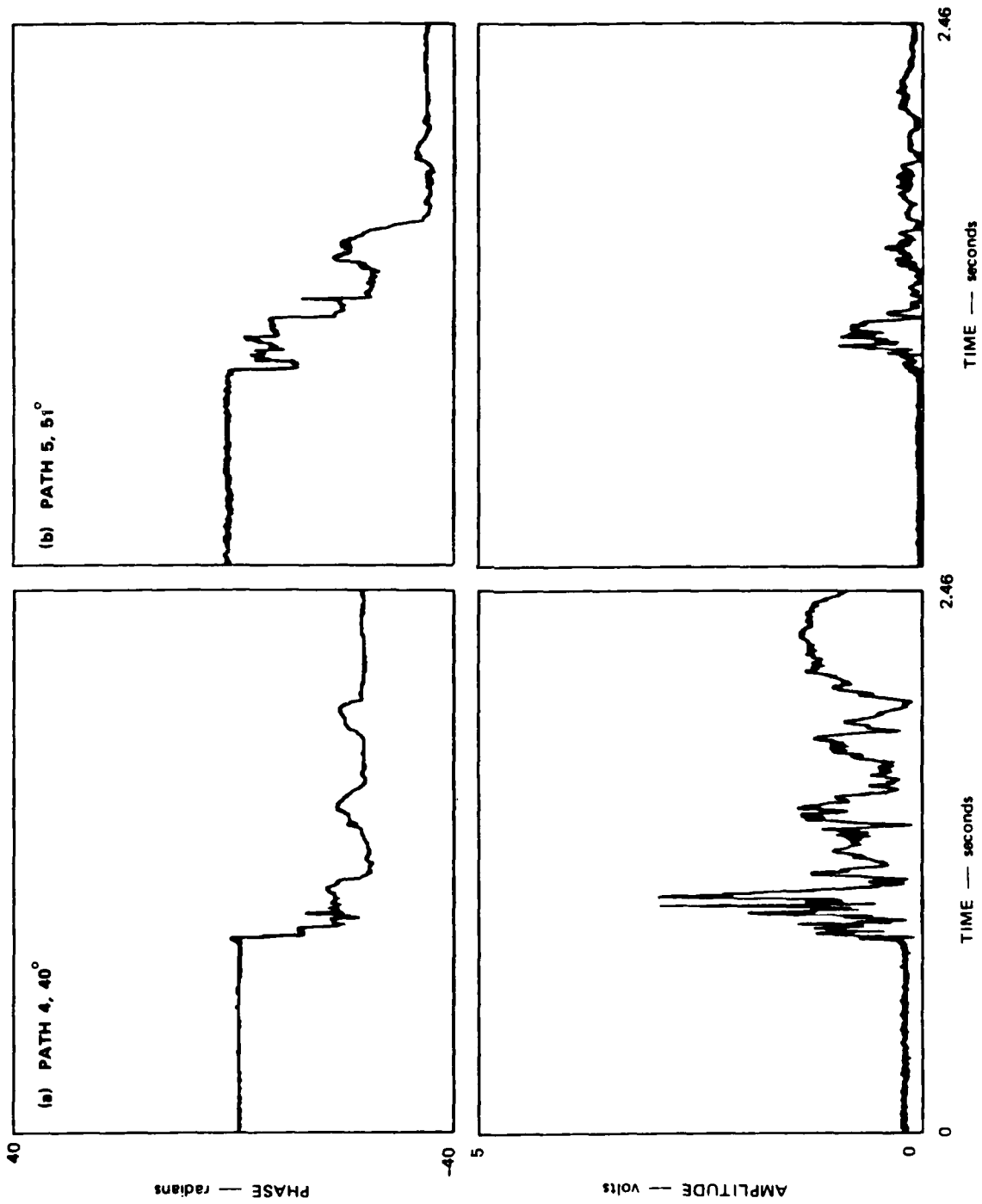


Figure 46. HST 144 amplitude and phase records.

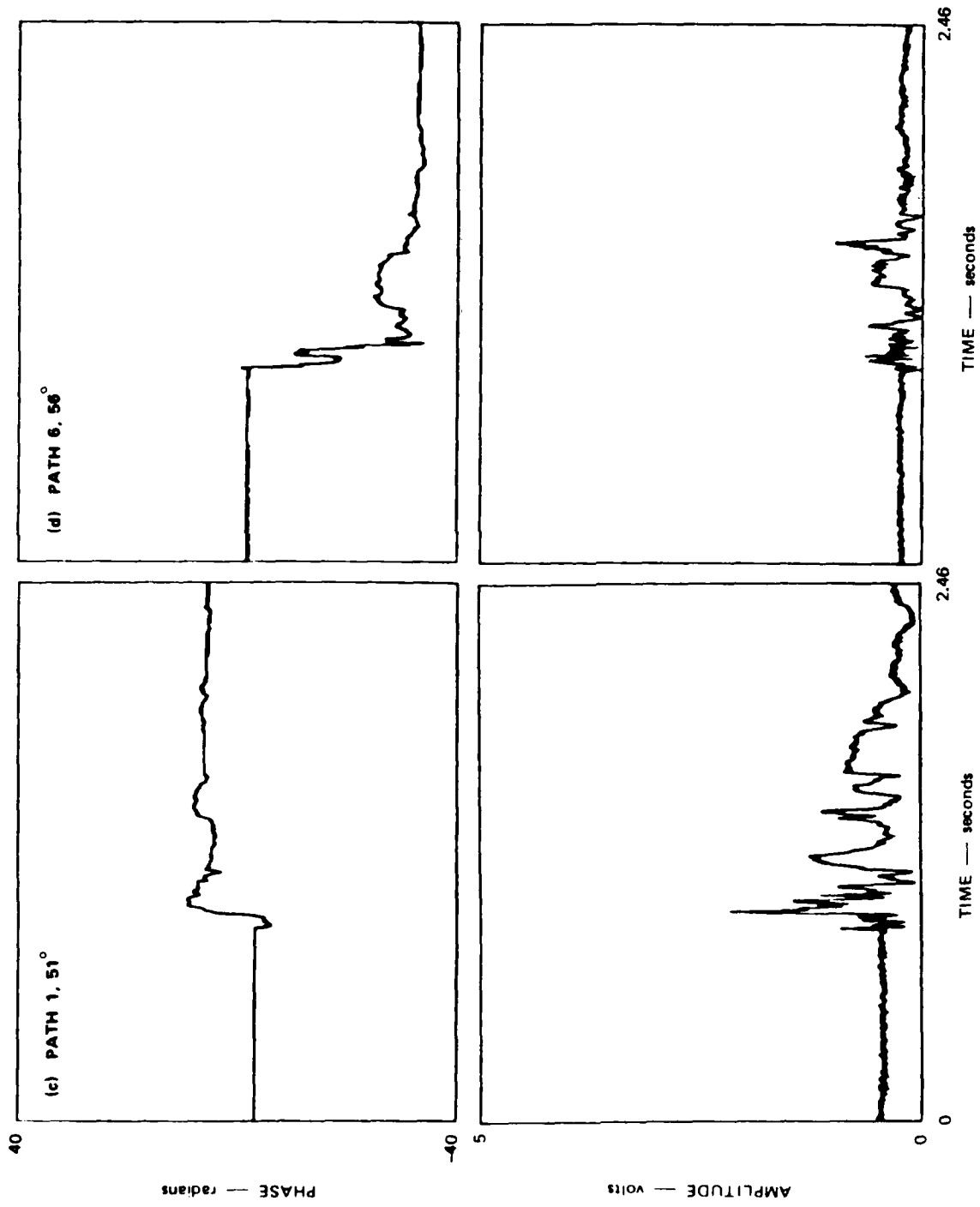


Figure 46. HST 144 amplitude and phase records (Continued).

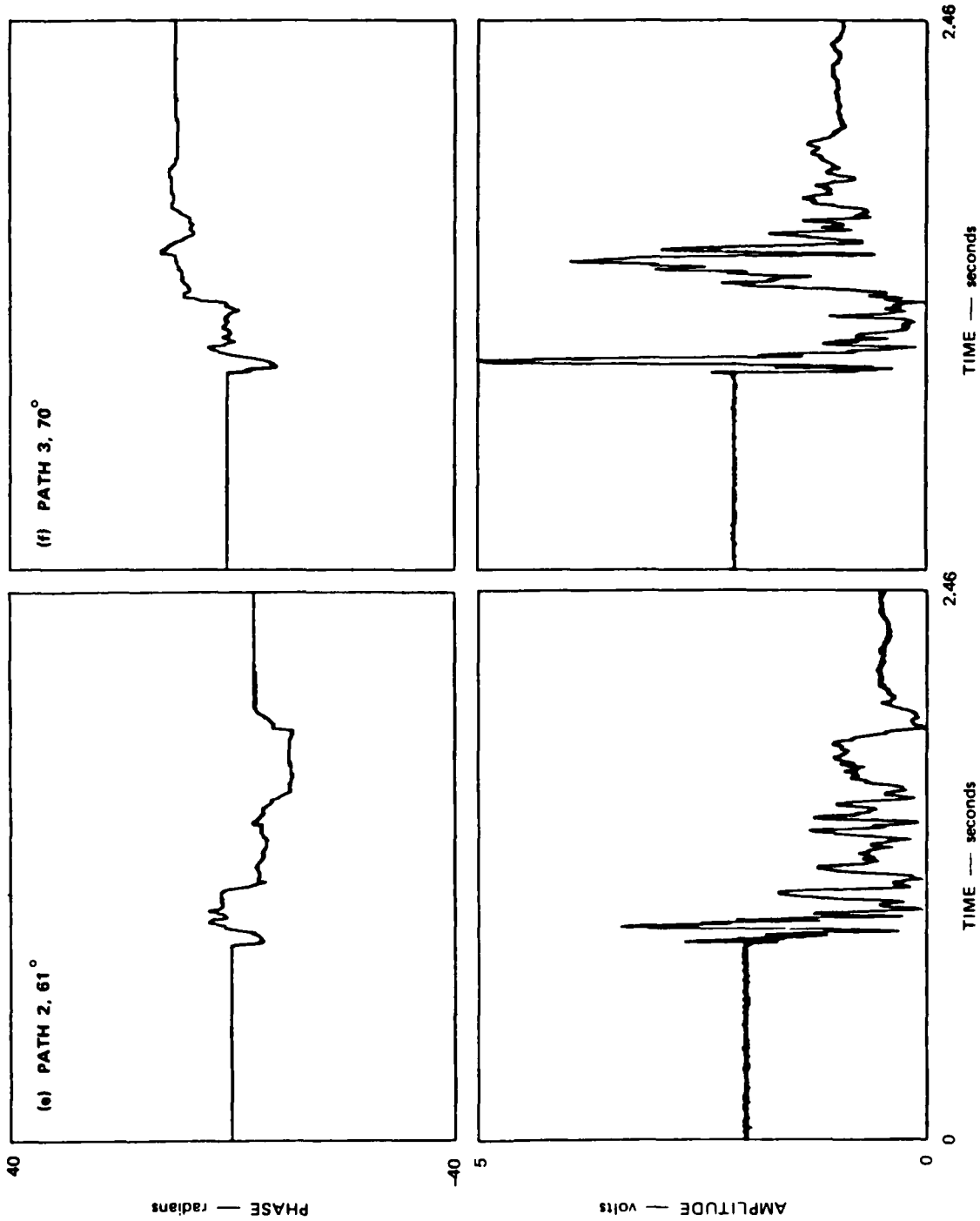


Figure 46. HST 144 amplitude and phase records (Concluded).

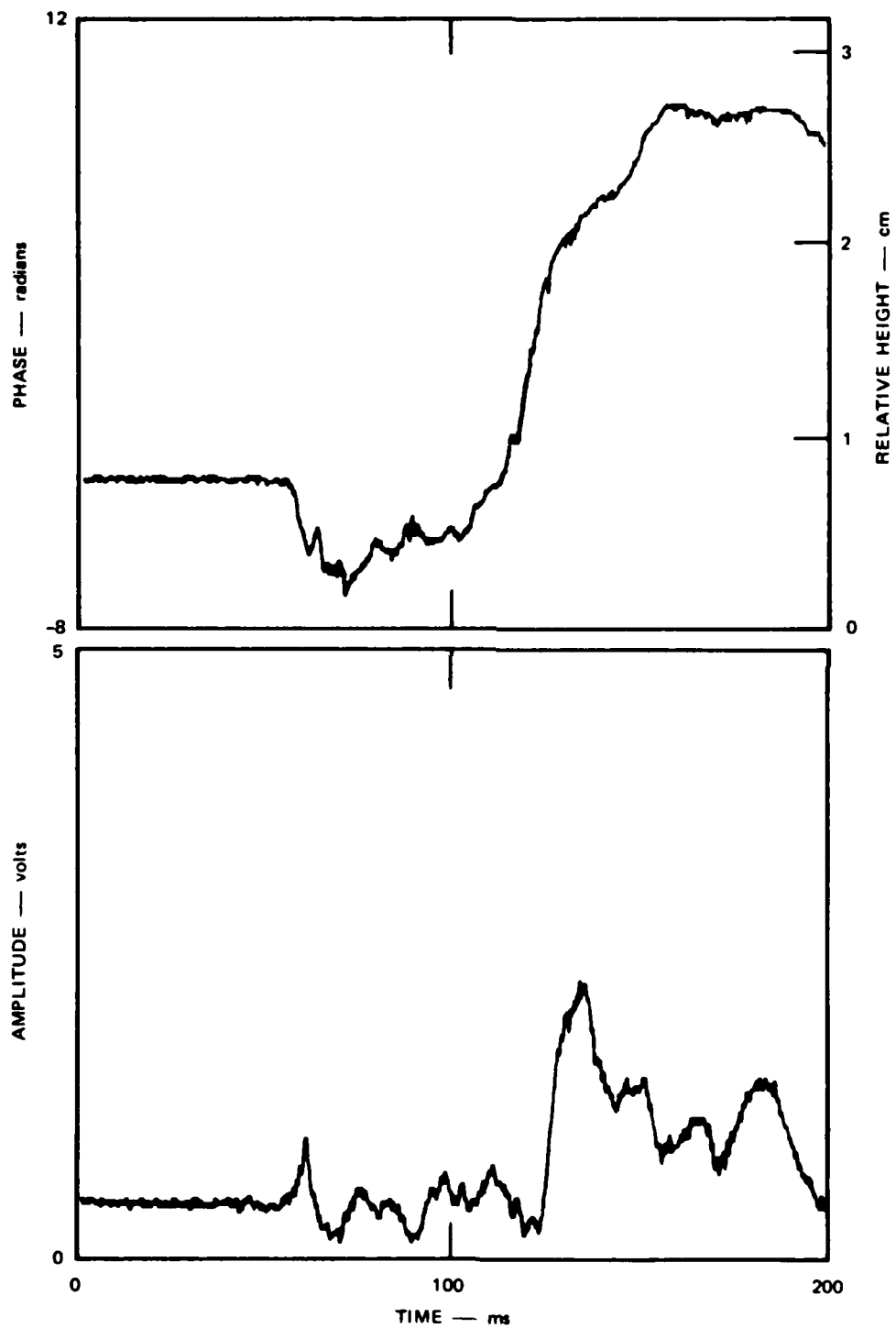


Figure 47. HST 144 Path 1 phase and amplitude records.

Although this example produced plausible results in terms of order of magnitude, the actual numerical values cannot be considered to be particularly accurate. The results from paths with the same angle of incidence are not consistent with each other, although this may be a result of the weaker signal on Path 5 than Path 1, an artifact caused by the signal leakage problem, or a difference caused by the different point of geometrical reflection. In addition, for the paths with strong signals, the trend toward greater initial negative phase changes during the positive phase with increasing angle of incidence is opposite to that expected on the basis of Eq. (33). This reverse trend may also be an artifact from leakage, and it is possible, although there is no other evidence for it, that the paths are misidentified. A more intensive analysis involving changes in soil refractivity with density is needed to obtain the surface height variations accurately, but could not be successfully accomplished with these data because of the leakage problem.

The paths with the lowest angles of incidence tended to have the weakest signals. This is consistent with the expectation of better reflection near grazing incidence. In addition, the signals for the lowest incidence angle (40 deg) showed substantial increases during shock-wave passage. This is evidently due to transition to total internal reflection resulting from an increase in the dielectric constant of the uppermost layer from compression and scouring of loose material.

Note that the best data from these sets come from the antennas having the largest separations. In particular, Transmit Antenna 1 produced significantly better signals than did Antenna 2. This is attributed to less leakage from Antenna 1. An effect of leakage is to reduce the amount of phase change measured relative to the amount that actually occurred along the signal path. This is consistent with the observed increase in phase shift magnitude during the positive phase of shock-wave passage.

Qualitatively correct results were thus obtained from the surface recession tests in the 6-ft shock tube. However, because of the leakage of rf energy outside the tube and the small amount of space available to mount antennas below the soil surface, these trials did not afford a good test of this technique.

SECTION 6

CONCLUSIONS AND RECOMMENDATIONS

Instrumentation was assembled so that we could measure mean air and dust densities and surface recession. Two series of shakedown tests have been conducted which comprised a total of nine shots in the CERF/NMERI 6-ft shock tube. A number of problems were encountered, which were primarily caused by mechanical effects from firing the shock tube. The most important of these were motion of the mmW antennas caused by the dynamic expansion of the shock tube, impulse noise induced in the X-ray detector preamplifier, a tendency of the rf equipment emplaced near the shock tube to lose phase lock, and cross-talk between some data channels.

A number of corrective actions have either been accomplished or identified. Improvements of the packaging and shock mounting of the X-ray preamplifier that were made between the two series of tests reduced the impulse noise substantially but did not entirely eliminate it. The preamplifier now has been completely repackaged to eliminate any motion of internal components and is now nonmicrophonic. A temperature-sensitive instability in a phase-locked oscillator within the mmW system was identified as being the source of that system's tendency to lose lock; this has been remedied but not field tested. Other instability problems caused by mechanical shocks and high environmental temperatures can be overcome by using better physical protection, such as shelters for the exposed equipment.

Although the two series of shakedown tests produced semiquantitative data because of the instrumentation problems and, particularly for the surface recession measurements, difficulties with using the 6-ft shock tube as a test bed, the fundamental bases for the measurements were demonstrated. Plausible results of the proper magnitude were obtained

for both types of measurement. Specific recommendations for improvements in equipment, procedures, and installation have been developed from the results of these tests.

For the mmW/X-ray measurements, these are

- (1) Isolate the mmW antennas from shock-tube motion. The antennas should be supported so as to minimize differential motion between them. We recommend mounting on concrete piers, not in physical contact with the tube.
- (2) Mount the accelerometers on the mmW antenna support plates so that the difference between accelerometer signals corresponds to differential motion. This will minimize the effect of any residual carrier-mode crosstalk or interference and permit using the accelerometer data to reduce any motion effects.
- (3) Use a more monochromatic X-ray beam to reduce further spectral hardening effects.
- (4) Recalibrate the X-ray air and soil absorption using the more monochromatic X-ray beam. There is a need for more soil calibration data at lower values of dust loading.
- (5) Use the late-time (recovery) data as the basis per shot for calibrating the ratio of mmW phase shift to X-ray absorption for soil.
- (6) Improve the filtering to reduce ac X-ray ripple on the high-voltage power supply.
- (7) Provide better environmental protection for the mmW equipment during tests.

Specific recommendations for the surface recession measurements are

- (1) Avoid testing or use in small facilities such as the 6-ft shock tube, where the subsurface volume is limited and signal leakage paths can exist outside the tube.

- (2) Use more directional, higher-gain antennas, such as the horn antenna prototype designed and built for operation underground.
- (3) Provide better environmental protection (this would be accomplished automatically by an entirely subsurface installation) for the equipment.

The basic instrumentation is complete. With these incremental improvements and changes these novel experimental approaches will be entirely operational.

SECTION 7

LIST OF REFERENCES

1. George Ullrich, DNA (private communication).
2. A. A. Burns and K. R. Sweeney, "DIRECT COURSE Microwave-Transmission Experiment," Technical Report, Contract DNA 001-83-0203, SRI Project 5673, SRI International, Menlo Park, CA (November 1985).
3. A. A. Burns and P. L. Crowley, "DICE THROW UHF/SHF Transmission Experiment: Volume III--Final Data Reduction and Interpretation," Topical Report, Contract DNA 001-75-C-0206, DNA 4216T-3, SRI Project 3972, SRI International, Menlo Park, CA (August 1979).
4. A. A. Burns and E. E. Martin, "MISERS BLUFF Electromagnetic Propagation Experiments: Volume III--Final Analysis of the UHF-SHF Radar-Scattering and Coherent-Transmission Experiment Data," Final Report, Contract DNA 001-79-C-0181, DNA 4806T-5, SRI Project 8279, SRI International, Menlo Park, CA (September 1983).
5. A. Ishimaru, Wave Propagation and Scattering in Random Media, Vol. 2 (Academic Press, New York, NY, 1978).
6. M. J. Campbell, J. Ullricks, and B. W. Hapke, "The Electrical Properties of Rocks and Their Significance for Lunar Radar Observations," CRSR333, Center for Radio Physics and Space Research, Cornell University, Ithaca, NY (February 1969).
7. C.J.F. Bottcher, Theory of Electric Polarization, p. 415 (Elsevier Publishing Company, Amsterdam, 1952).
8. D. Wobschall, "A Theory of Complex Dielectric Permittivity of Soil Containing Water: The Semidisperse Model," IEEE Trans. Geosci. Electron., Vol. GE-15, No. 1, pp. 49-58 (January 1977).

Appendix A
TRUE-HEIGHT ANALYSIS

Appendix A

TRUE-HEIGHT ANALYSIS

In order to solve the vertical profile of particular density profile $\rho(z)$ or the corresponding refractive index profile $n(z)$, it is convenient to decompose the integral of Eq. (32) for the electrical path length into the horizontal component (x coordinate) and the vertical component (h coordinate) by using the following:

$$ds = dx \sin \theta + dh \cos \theta \quad . \quad (A-1)$$

The electric path length in Eq. (7) then reduces to

$$P_e = \int_T^{R_e} n \sin \theta \, dx + 2 \int_T^{h_R} n \cos \theta \, dh \quad (A-2)$$

where T is the position of the transmitter, R_e is the position of the receiver assumed at the same horizontal level as T, and h_R is the height of the reflecting point R. The assumption of horizontal stratification makes the ray symmetric around the vertical axis through R.

By using the Snell's law, the first integral of Eq. (A-2) reduces to the constant $n_o D \sin \theta_o$ where D is the horizontal separation between transmitter and receiver. Also by using the Snell's law, the following expression can be written as

$$n \cos \theta = \left(n^2 - n_o^2 \sin^2 \theta_o \right)^{1/2} \quad , \quad (A-3)$$

and the electric path length can be written as

$$P_e = n_o D \sin \theta_o + 2 \int_T^{h_R} \left(n^2 - n_o^2 \sin^2 \theta_o \right)^{1/2} dh \quad (A-4)$$

where n and, therefore, the quantity under the radical are functions of h , and the value h_R is solved by the condition:

$$n_R = n(h_R) = n_o \sin \theta \quad (A-5)$$

Experimentally, P_e will be the parameter directly measured, however, $n_o D \sin \theta_o$ can be calculated so a measured virtual height, h' , can be defined:

$$h' = 2(P_e - n_o D \sin \theta_o) \quad (A-6)$$

The problem is then reduced to the more familiar form of solving $n(h)$ or $n^2(h)$:

$$h' = \int_T^{h_R} \left(n^2 - n_R^2 \right)^{1/2} dh \quad (A-7)$$

If N values of n_R are measured the functional dependence of n as a function of h can be solved. Equation (A-7) can be written as

$$h' = \int_{n_o}^{n_R} \left(n^2 - n_R^2 \right)^{1/2} \frac{dh}{d(n^2)} d(n^2) \quad (A-8)$$

Let us assume now that the N experimental configurations are chosen so that

$$\begin{aligned} \theta_{o_1} &> \theta_{o_2} > \theta_{o_3} \dots > \theta_{o_N} \\ n_{R_1} &> n_{R_2} > n_{R_3} \dots > n_{R_N} \end{aligned} \quad (A-9)$$

Then we can divide the space in N slabs: the first slab between n_0 and n_{R_1} , the second between n_{R_1} and n_{R_2} , and so on. Furthermore, the assumption of constant gradient between the break points can be made. Then

$$h'_M = \sum_{j=1}^M \left. \frac{dh}{d(n^2)} \right|_j A_{Mj} \quad (A-10)$$

for $M = 1, 2 \dots N$

where the constants A_{Mj} are calculated independently from the functional dependence of n on h :

$$A_{Mj} = \int_{n_{R_j}^2}^{n_{R_{j+1}}^2} \left(n^2 - n_{R_M}^2 \right)^{1/2} d(n^2) \quad (A-11)$$

Equation (A-10) forms a linear system of N equations where the derivatives $\left. \frac{dh}{d(n^2)} \right|_j$ for each slab can be easily solved and the solutions would give n as a function of h .

A second iteration can be made by calculating the second order correction $\Delta\theta_0$ to the angles of incidence θ_{0N} and then reiterating the procedure. Ray tracing can be used to refine the results.

The practical problem that the procedure sketched above may encounter in practice is the delimitation of the plane at which n_0 starts changing, but we assume it can be solved. A more serious limitation is that an implicit assumption that the index of refraction decreases monotonically with height. Valleys of higher values of n may not be adequately described, and if there is a reason to believe they exist, a ray-tracing technique to adjust the parameters of the gradient may be used.

Appendix B
MINOR SCALE FIELDING

Appendix B

MINOR SCALE FIELDING

1. INTRODUCTION.

The mmW/X-ray system was fielded for the MINOR SCALE test, which occurred on 27 June 1985. It was installed at the 30-psi overpressure level completely underneath the helium bag in the precursor region. Figure 48 depicts the installation, which spanned the center of the precursed radial immediately behind the other installations at 30 psi overpressure. There were several important differences between the details of that system and the one used for the 6-ft shock-tube tests:

- (1) A 60-ft path length was used versus 6 ft.
- (2) The mmW/X-ray beam centers were 17 in. above the surface.
- (3) The X-ray detector used a 7-in. versus a 2-in. scintillator.
- (4) The above-ground parts of the system (the X-ray tube and detector and the mmW antennas) were housed in 12-in. diameter steel pipes cast into massive concrete bases.
- (5) Greater protection from blast effects was afforded because the equipment was buried in vaults.
- (6) Long coaxial cable runs were used to send signals from the installation in the test bed to the recording system.
- (7) Storage batteries were used to provide electrical power to the X-ray tube HV power supply through a 1.5-kW inverter.

It was not possible to test this equipment in the field before the MINOR SCALE event. In consequence, none of the problems revealed by the later developmental tests in the 6-ft shock tube were known. However, because of the differences between the MINOR SCALE installation and that

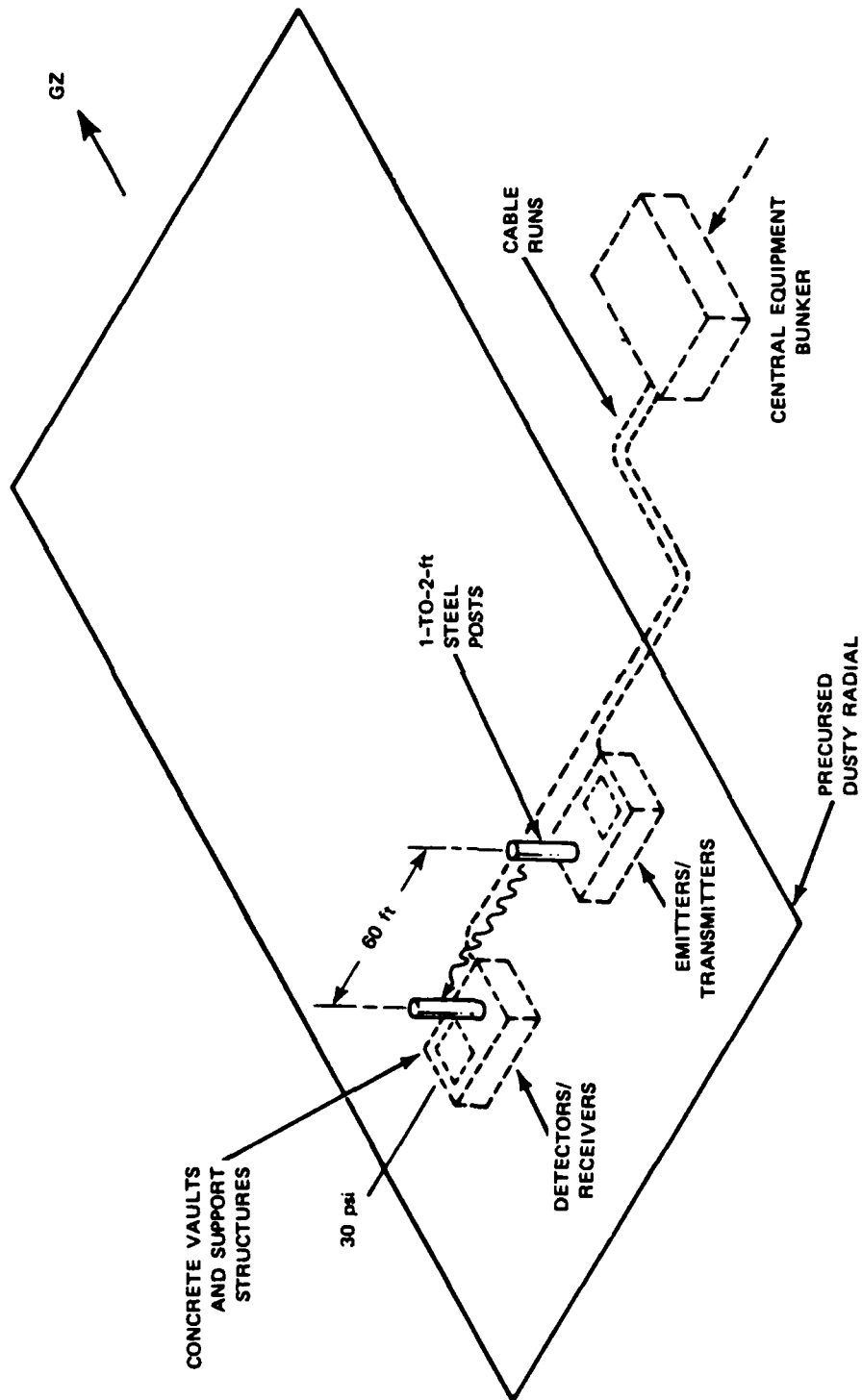


Figure 48. mmW/X-ray transmission experiment for MINOR SCALE.

for the 6-ft shock-tube tests and the greater protection provided for the equipment, a somewhat different set of experimental problems occurred during MINOR SCALE. The most serious problem was a large, long time constant transient in the X-ray detector signal. Although the X-ray system subsequently recovered, this produced a complete loss of data during the most important part of the event. On the other hand, the mmW system apparently suffered no problems; there was no loss of phase lock and no apparent antenna motion effects.

Because of the longer path length, there was measurable mmW wave absorption during MINOR SCALE. This was sufficient to permit a separation of mmW phase and amplitude data into air and dust density estimates. In effect, the mmW absorption took on the role of the X-ray absorption measurement.

2. MINOR SCALE RESULTS.

2.1 mmW Results.

Figure 49 presents the mmW phase and amplitude records. The phase and absorption tend to track each other, which, because air produces no appreciable absorption over this short a path length, means that most of the phase shift change is due to dust loading. Because there was no significant phase shift associated with the brief increase in attenuation at about $T + 1$ s, it was presumably caused by a large opaque object (or swarm of objects comparable to the rf wavelength in circumference) passing through the mmW beam. This did not affect the measurements.

Figure 50 shows the long term mmW phase and attenuation results. There were several more-or-less discrete events or episodes that have been identified as being reduced by crater ejecta falling through the beam. A simple analysis can be made involving the time of flight of ejecta particles, which can be measured directly from Figure B-3, plus assumptions concerning the drag coefficient of particles large enough in terms of wavelength to produce a low ratio of phase

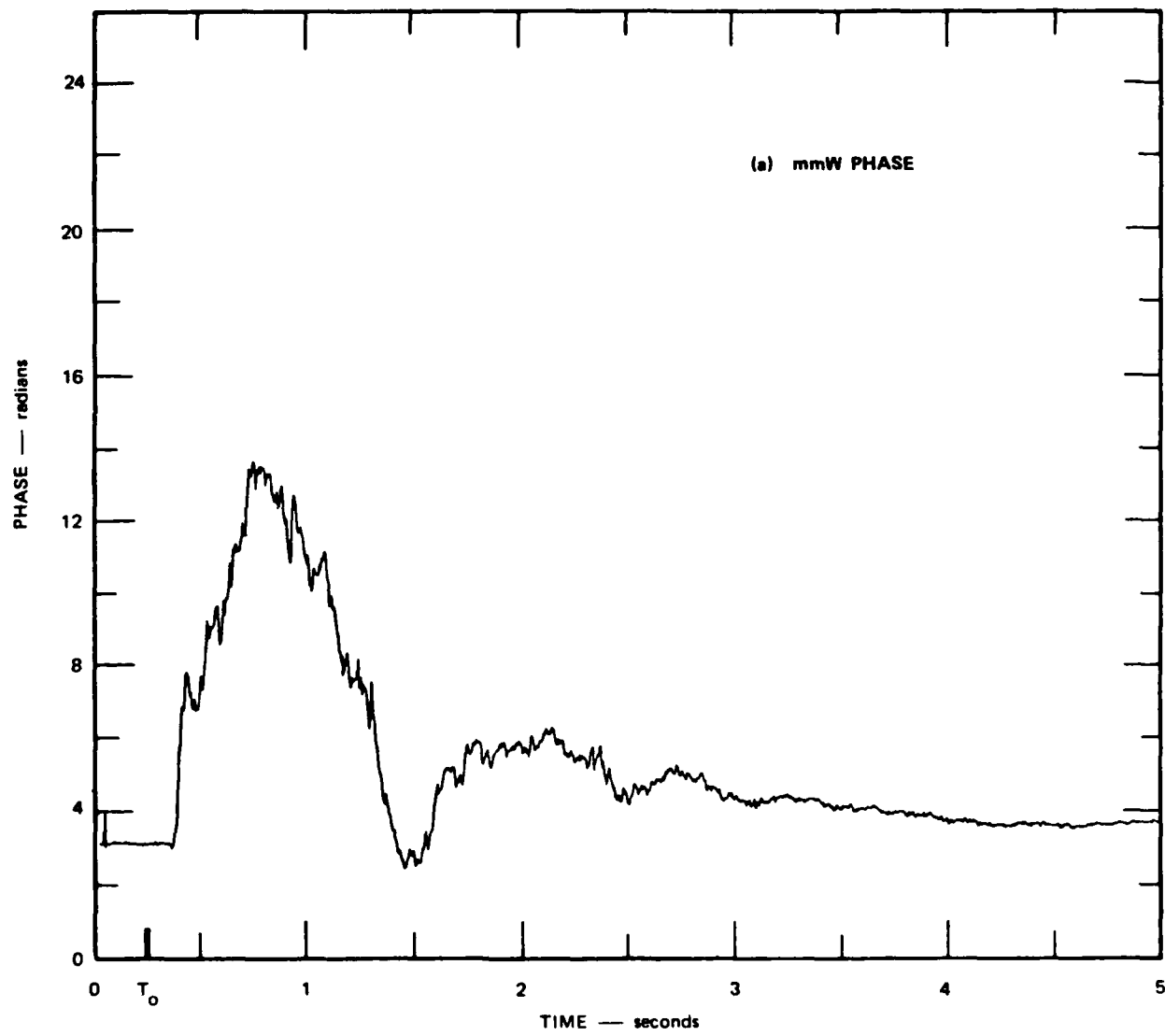


Figure 49. MINOR SCALE mmW phase and amplitude records.

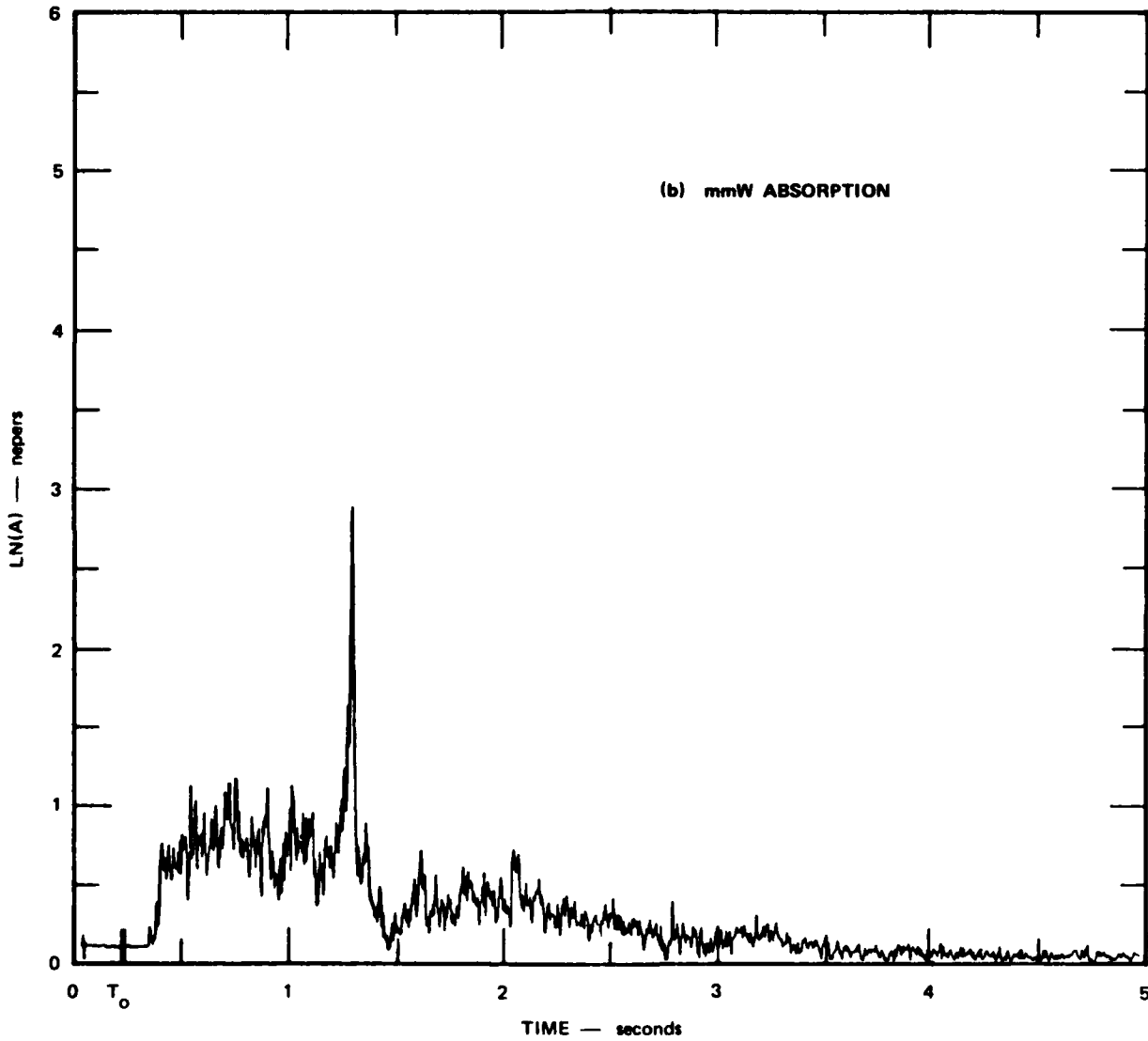


Figure 49. MINOR SCALE mmW phase and amplitude records (Concluded).

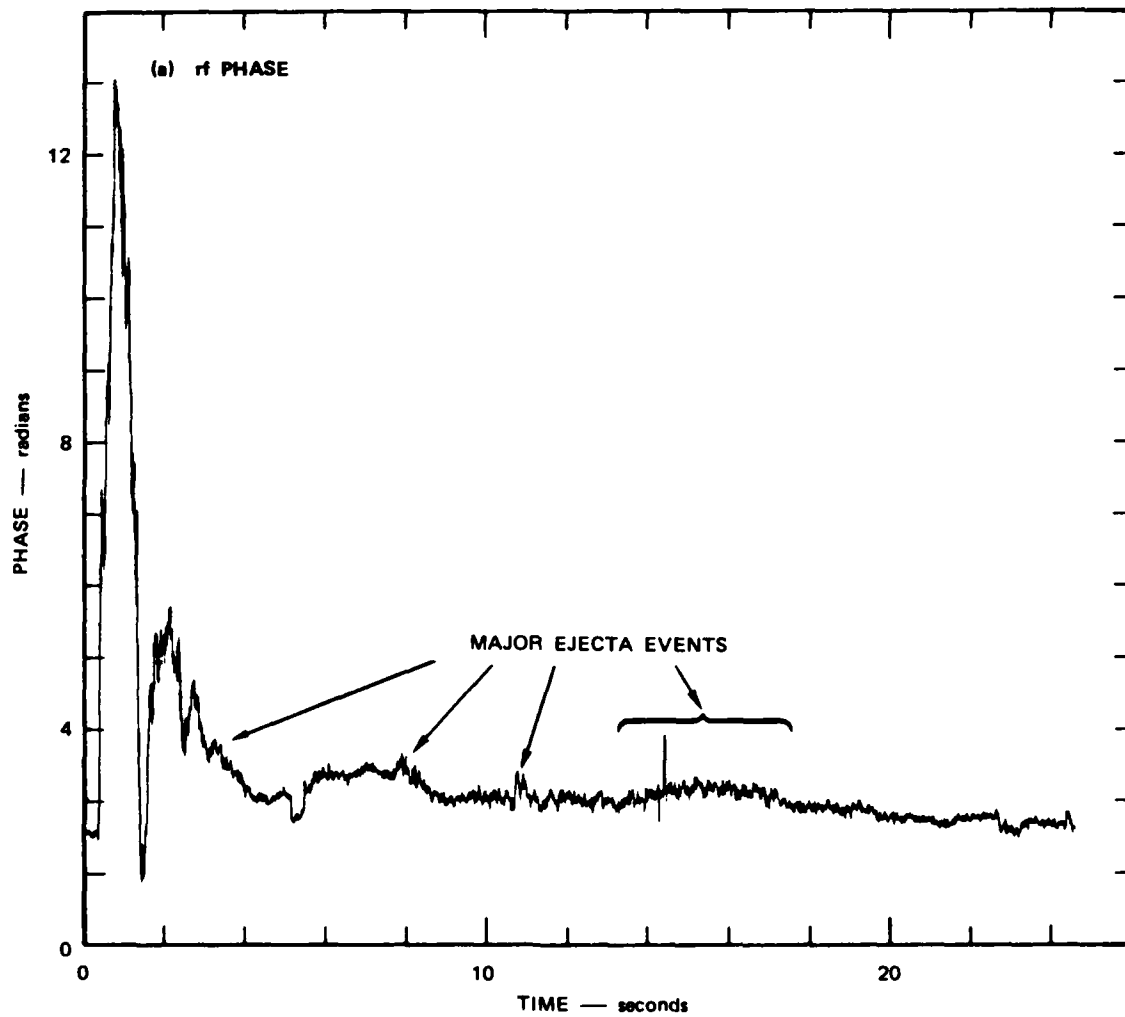


Figure 50. Long-term mmW phase and amplitude records.

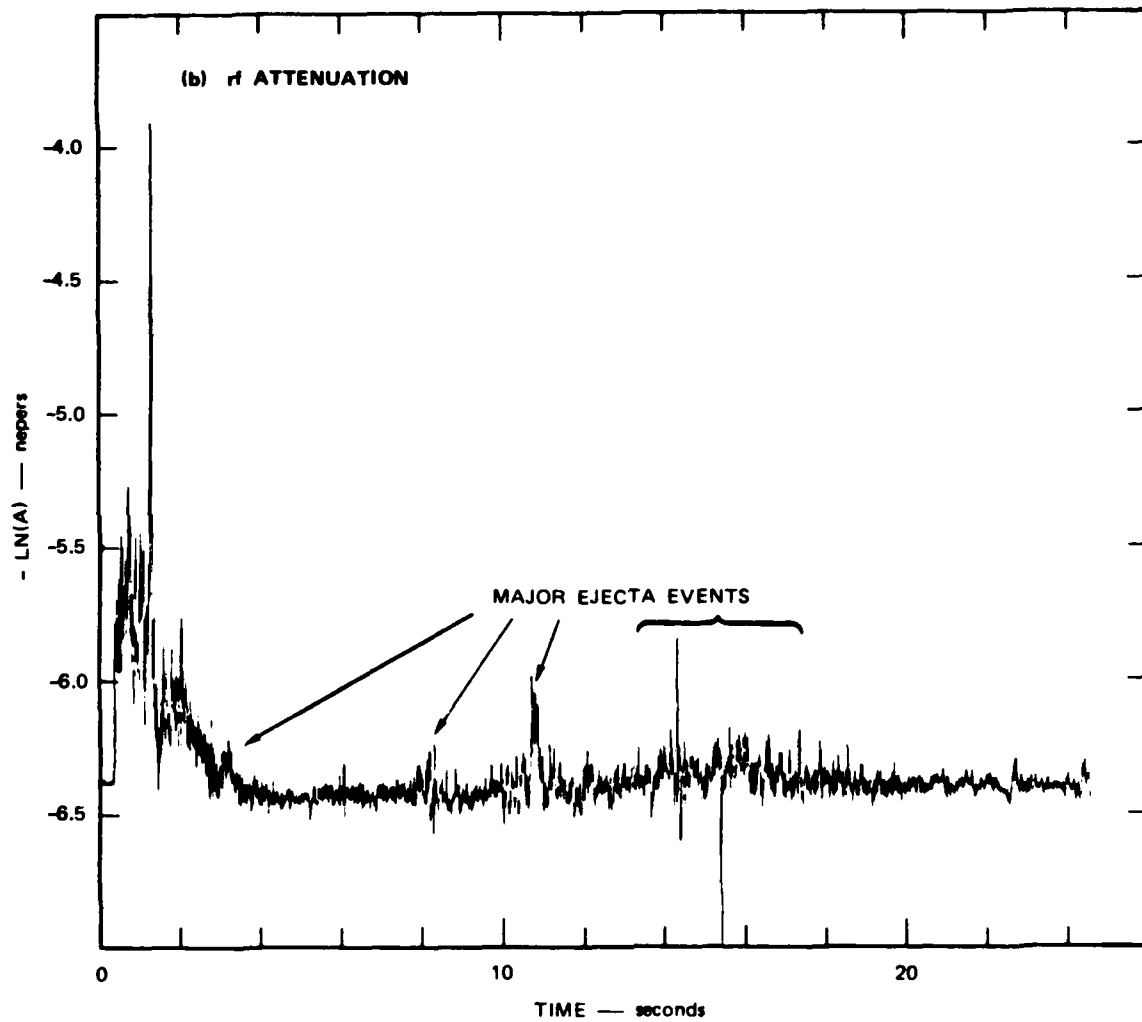


Figure 50. Long-term mmW phase and amplitude records (Concluded).

shift to attenuation. The results of this analysis are consistent with 0.5- to 3-cm diameter ejecta particles having ejection velocities and angles in the range of 100 to 250 m/s and 16 to 61 deg.

The increased fluctuation levels of phase and amplitude at late times compared to the pre-event level shows that fluctuations in air/dust density caused by turbulence and irregularities in the flow and by fallout continued throughout the recording interval up to $T + 25$ s. However, the mean level of dust loading fell to a small fraction of the air density as the phase shift approached its baseline value. For the ambient conditions at shot time, the calculated baseline phase shift is 3.69 radians. Because of the low density of the helium-air mixture in the bag, the preshot phase shift should have been about 20 percent of this value, and there should have been a shift of about 3 radians from the pre-event value to the late-time postevent level. However, the observed shift was close to zero radians. This discrepancy is probably caused by water vapor that had been released from the soil by solar heating and trapped under the bag.

As noted in the main text, water vapor has a strong effect on phase shift because water vapor molecules are easily polarized. At 1000 hours, 2 hours 20 min before T_0 , the temperature and relative humidity in the bag were reported to be 120°F (48.9°C) and 20 percent. Somewhat earlier they were 110°F (43.3°C) and 30 percent, respectively. Both readings correspond to a vapor pressure of about 27 mbar compared to 10.2 mbar for the ambient air (Table 1 in the main text).

The amount of water vapor required to make up 3.7-radians phase shift can be calculated using Eqs. (14) and (28). At 149°F (65°C), the required vapor pressure is $e = 71$ mbar, which corresponds to a relative humidity of $r = 39$ percent. An unverified report stated that all the temperature sensors in the bag had exceeded their maximum recording level of 147°F (63.9°C) and that the temperature in the bag could have reached 160°F (71°C). At that temperature, the required values of e and r are 79 mbar and 22 percent, respectively. We conclude

that sufficient water vapor was present to account for the lack of a baseline shift.

2.2 X-Ray Results.

The X-ray detector was seriously affected by the blast and no useful data were obtained. Figure 51 presents the X-ray detector signal as recorded. It was not possible for safety reasons to operate the X-ray system after the bag deployment began, so the higher X-ray signal level with helium present had to be estimated a priori. Although the pre-event level was set slightly too high into the digitizer, leading to the clipping seen before T_0 in Figure 51(a), this would not have affected the measurement. The long-term data shown in Figure 51(b) were not affected by the high gain setting because they were obtained from a backup analog recorder.

The serious problem was the transient that occurred just after shock wave arrival, during which the X-ray detector signal first went negative and then followed a long-time constant quasi-exponential decay. Note that the X-ray system continued to operate during this transient, as evidenced by the 120-Hz ripple from the X-ray source. Attempts to recover data from the leading edge of the shock wave and from after about $T + 1.5$ s, when the signal came out of negative saturation, were not successful.

At about $T + 14$ s the detector abruptly resumed normal operation, far too late for meaningful measurements. We were not able to find a cause for this failure, and the X-ray system operated correctly during postevent calibrations done the next morning. No anomalies were seen on the X-ray tube voltage and current monitor signals, so that potential source of the problem was eliminated. In addition, we were not able to reproduce this problem by interrupting the power supplies to the detector preamplifier, and the like, nor did it recur during testing in the 6-ft shock tube. The later arrival time of

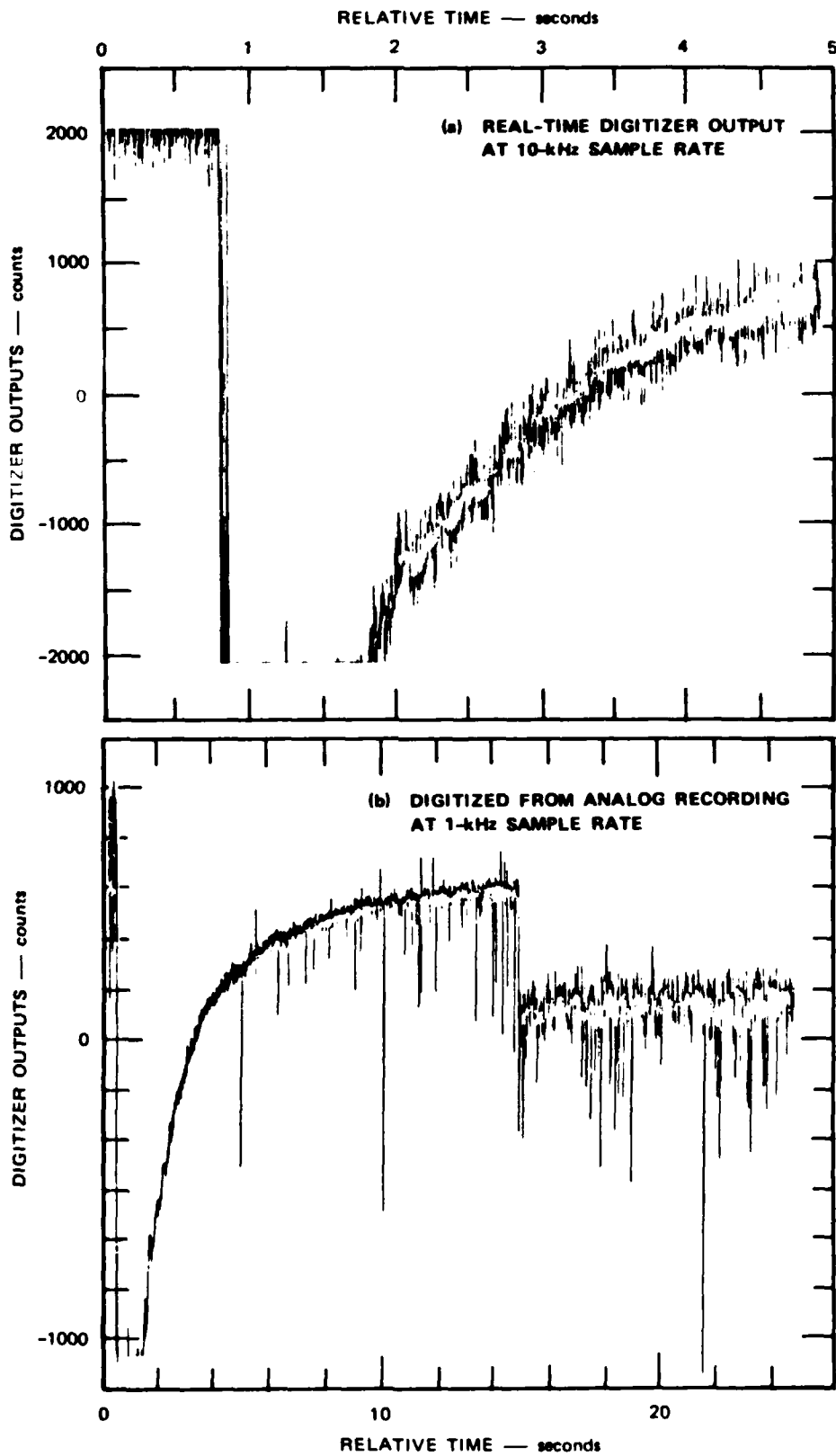


Figure 51. X-ray detector output.

the shock wave at the bunker eliminated the data-acquisition system as a possible source.

The probable source of the problem was discovered later during the air-absorption calibration runs. We believe the cause was an intermittent connection between the photodiode and its preamplifier owing to a defective coaxial connector. Disconnecting the diode from the preamplifier produced transients similar to that observed during the test. This problem has been repaired.

2.3 Air- and Dust-Density Estimates.

The relatively large amount of mmW absorption (which is a result of the long measurement path used for MINOR SCALE) makes it possible to separate the data into mean air- and dust-density estimates. However, this requires knowledge of the absorption coefficient of dust, which is virtually impossible to obtain accurately through independent calibration because of its sensitivity to moisture content. The loss-tangent factor in Eq. (18), which relates absorption to dust density, is the sensitive term. Note that unlike the X-ray situation, the dust density is proportional to mmW absorption alone. Thus the accuracy of the dust density estimate is determined by only one calibration factor by itself, rather than the two required for the X-ray approach. Estimating air density does require two factors, but one of them (phase shift because of air) is well known, which improves the overall accuracy. Although use of mmW data alone reduces sensitivity to calibration errors, the smaller magnitude of the mmW absorption compared to X ray tends to decrease overall accuracy.

Calibration of the mmW absorption factor was obtained from the test data themselves. At late times, the air density should have returned to near its ambient value, so any changes in mmW amplitude and phase should track one another, as indeed they do as noted above. Thus a regression analysis similar to that used to verify the ratio of X-ray absorption to mmW phase (Section 2.5.5) can be applied to obtain the relationship between mmW absorption and phase. Then the calibration

factors relating air and dust densities to phase shift (Section 2.5) are used in the final step. The result of a regression analysis between mmW attenuation and phase appears in Figure 52. A value of 12.8 radians/neper for the slope was calculated, which corresponds to a loss tangent of about 0.002 for this material. These are reasonable values and were used to estimate the mean dust and air densities.

Figure 53 presents the final results of this analysis. As described above, there is no significance to the pre-event air density estimate because of the effect of the helium/air/water vapor mixture on mmW phase shift. In Figure B-6(b) the mean air density in the T + 300- to T + 400-ms interval has been set to its ambient value of about $1 \times 10^{-3} \text{ g/cm}^3$. The positive phase of the shock wave ended at about T + 400 ms. The mean dust density was $0.3 \times 10^3 \text{ g/cm}^3$ initially, and then rose to $1.5 \times 10^{-3} \text{ g/cm}^3$. The peak mean air density was $1.5 \times 10^{-3} \text{ g/cm}^3$ above ambient.

These results could be affected by the anomalies in the detonation that produced a shock wave normal pointing 10 deg away from the axis of the precursed radial. The experiment was designed under the assumption that the shock wave normal would be perpendicular to the measurement path in order to maximize spatial resolution. However, the combination of a long path (19.5 m) and the large angle (10 deg) means that there was about a 4-m-length component of the path normal to the shock front.

The measured mean air or dust density in the shock wave can be expressed as a convolution of the actual density and a rectangular waveform. Let $\rho(t,x) = \rho(t - x/c)$ be true actual mean density, where x = distance along shock front normal and c = shock front velocity. Then the measured density along a path of Length L inclined at an Angle α to the shock front will be

$$\bar{\rho}(t) = \frac{1}{L} \int_0^L \rho \left(t - \frac{x}{c} \right) dl$$

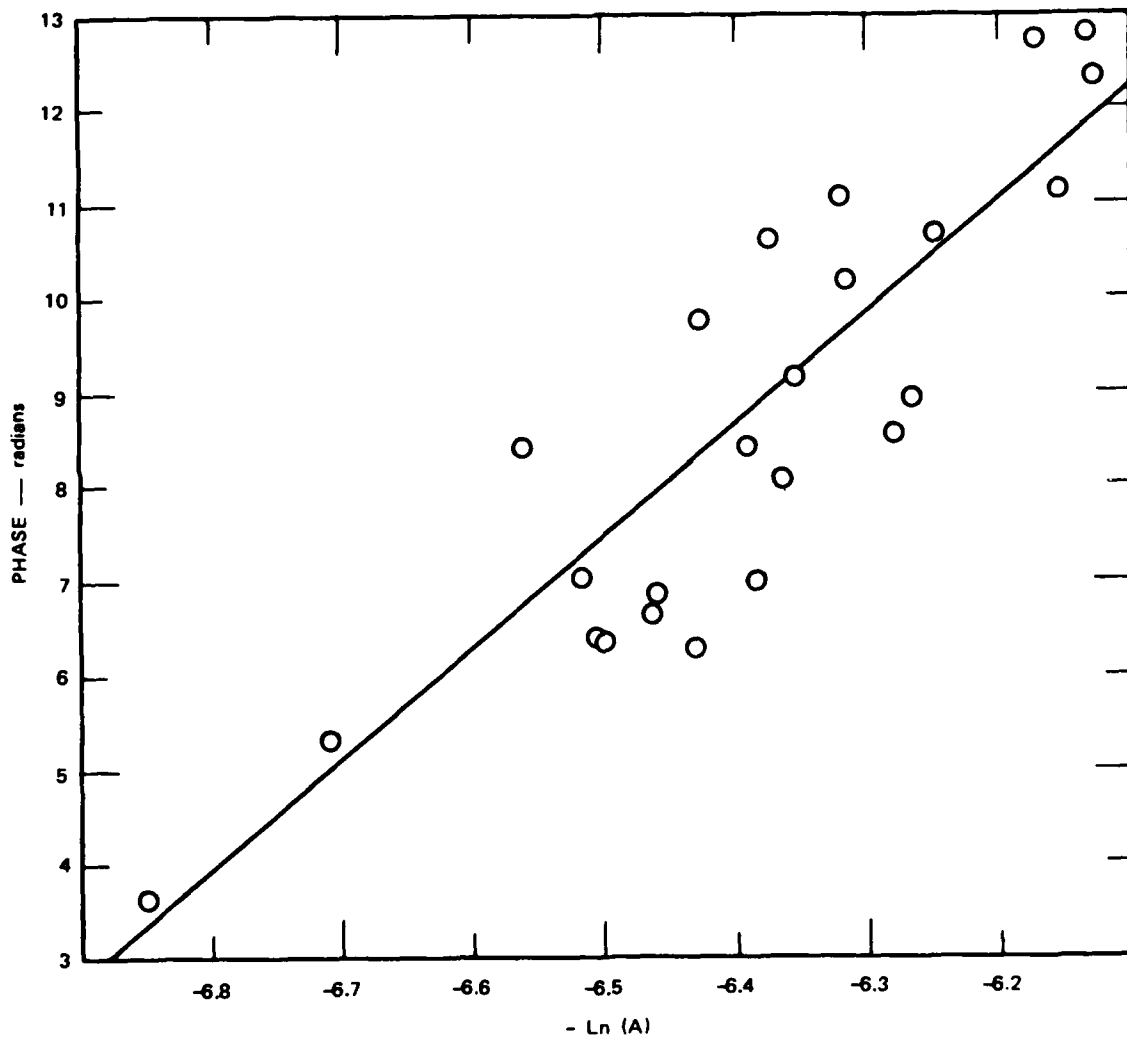


Figure 52. Regression analysis of phase vs. amplitude.

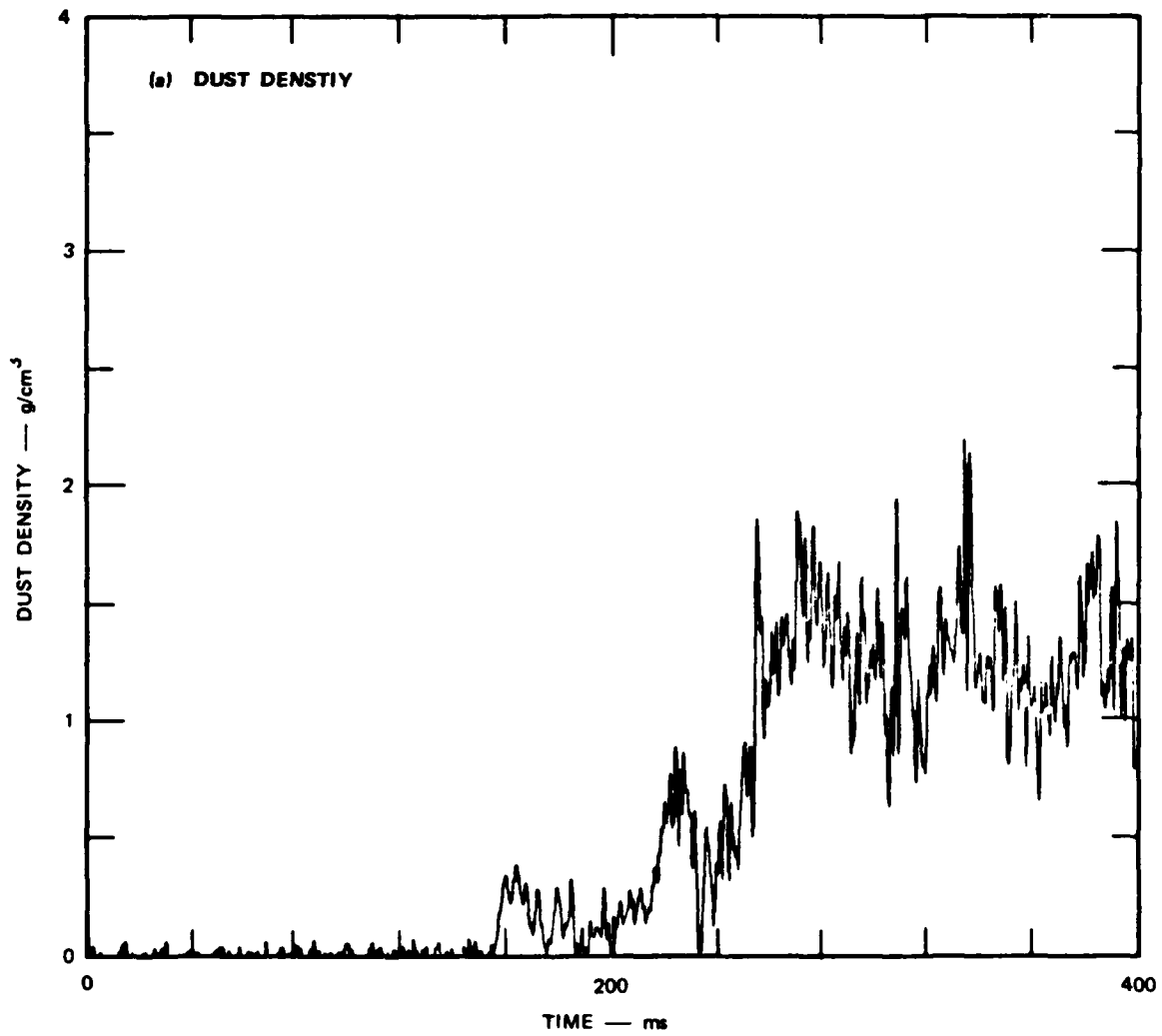


Figure 53. Dust and relative air-density estimates.

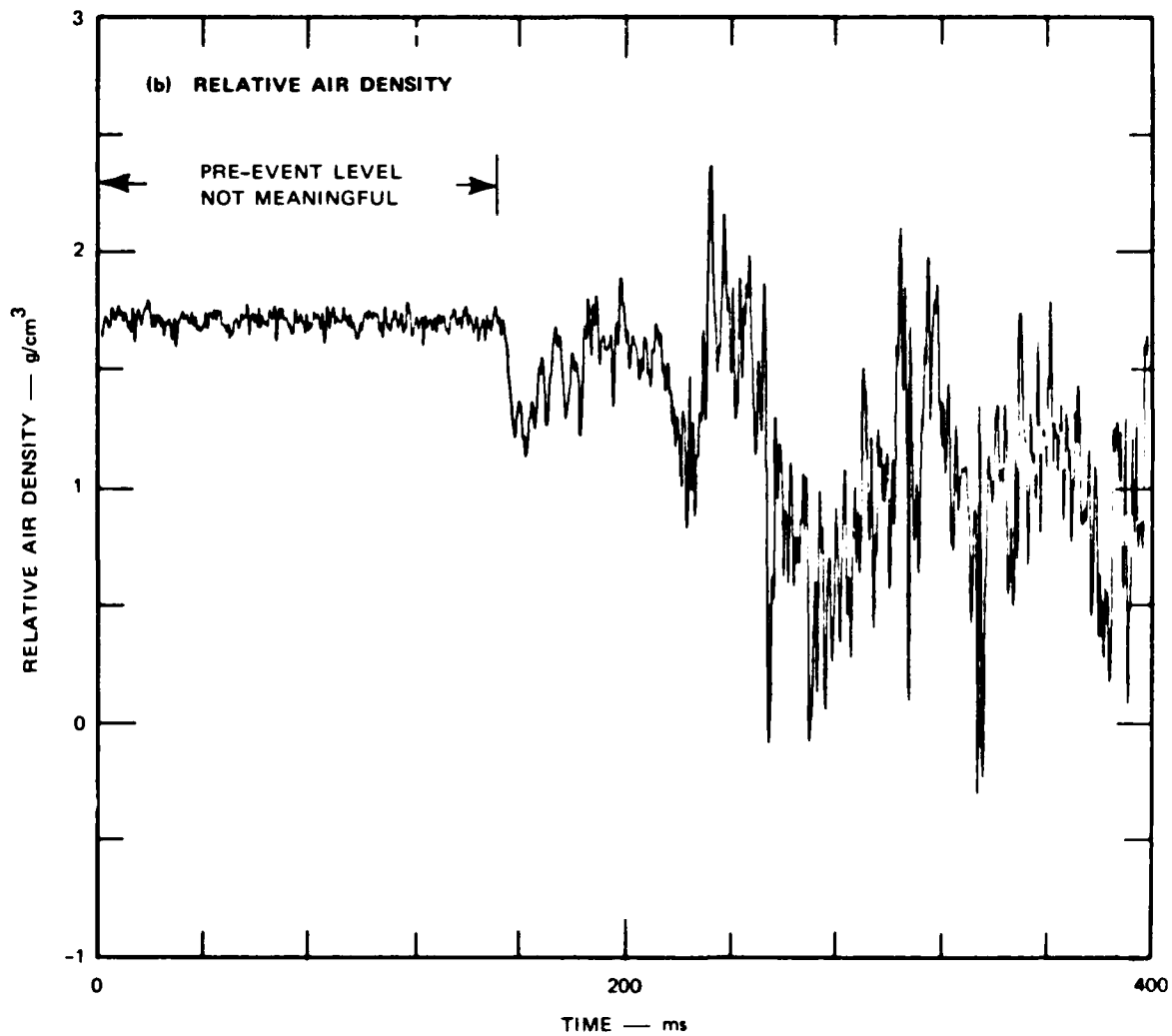


Figure 53. Dust and relative air-density estimates (Concluded).

$$\begin{aligned}
&= \frac{c}{L \sin \chi} \int_0^{\frac{L \sin \chi}{c}} \rho(t-\tau) d\tau \\
&= \int_{-\infty}^{\infty} \rho(t-\tau) u(\tau) d\tau \qquad (B-1)
\end{aligned}$$

where

$$u(\tau) = \begin{cases} \frac{c}{L \sin \chi} & 0 \leq \tau \leq L \sin \frac{\chi}{c} \\ 0 & \text{otherwise} \end{cases} .$$

The duration of the rectangular function, which in the limit $\chi \rightarrow 0$ becomes a δ function, is $T = L \sin \chi / c$. For MINOR SCALE in the precursed radial at 30 psi, $L = 19.5$ m, $\chi = 10$ deg, and $c = 640$ m/s, so $T = 5$ ms. This is not an appreciable length of time compared to the duration of the shock wave, whose pressure waveform somewhat resembles a sharp-fronted exponential decay with a time constant of about 90 ms. However, details shorter than 5 ms (3.4 m) will be smeared out by the convolution.

In theory, it is possible to deconvolve these data to recover $\rho(t)$. In practice, even small amounts of noise and experimental errors tend to thwart attempts at deconvolution. We note that use of a shorter path length (2 m, say) would have essentially eliminated this effect while still providing enough phase shift for accurate measurement (but not enough for mmW absorption--X-ray absorption measurements would be needed).

2.4 Conclusions.

In spite of loss of X-ray data because of equipment malfunction, it was possible to obtain estimates of mean air and dust densities from the mmW data alone. Good mmW data were recorded on MINOR SCALE. The dust loading in the leading edge of the shock wave, which arrived at $T + 153$ ms, was about 0.3×10^{-3} g/cm³. In the interval

between T + 153 ms and T + 230 ms, the air density stayed relatively constant in the range of about 1 to 1.5×10^{-3} g/cm³, after which it rose above 2×10^{-3} g/cm³ and then fell to its ambient value. At about T + 250 ms the dust density rose to about 1.5×10^{-3} g/cm³.

Corrective actions have been taken to solve the problems encountered on this test. It is recommended that future installations of this experiment utilize a significantly shorter path length (i.e., 1 to 2 m). The installation in the test bed can be greatly reduced in size as well, and use of long cable runs should be avoided.

DISTRIBUTION LIST

DEPARTMENT OF DEFENSE

AFSOUTH

ATTN: U S DOCUMENTS OFFICER

ASSISTANT TO THE SECRETARY OF DEFENSE ATOMIC ENERGY

ATTN: EXECUTIVE ASSISTANT

DEF RSCH & ENGRG

ATTN: STRAT & SPACE SYS (OS)
ATTN: STRAT & THTR NUC FOR J THOMPSON
ATTN: STRAT & THEATER NUC FORCES

DEFENSE INTELLIGENCE AGENCY

ATTN: DT-2
ATTN: RTS
ATTN: RTS-2B

DEFENSE NUCLEAR AGENCY

ATTN: OPNS
ATTN: SPAS
4 CYS ATTN: TITL

DEFENSE TECHNICAL INFORMATION CENTER 12 CYS ATTN: DD

FIELD COMMAND DEFENSE NUCLEAR AGENCY

ATTN: FCPR
ATTN: FCT COL J BOYCE
ATTN: FCTT W SUMMA
ATTN: FCTXE

FIELD COMMAND DNA DET 2 LAWRENCE LIVERMORE NATIONAL LAB ATTN: FC-1

JOINT CHIEFS OF STAFF

ATTN: J-5 NUCLEAR & CHEMICAL DIV

JOINT STRAT TGT PLANNING STAFF

ATTN: JK (ATTN: DNA REP)
ATTN: JKCS
ATTN: JPEP
ATTN: JPPFM

DEPARTMENT OF THE ARMY

DEP CH OF STAFF FOR OPS & PLANS ATTN: DAMO-NCZ

HARRY DIAMOND LABORATORIES ATTN: SLCHD-NW-RH

U S ARMY MATERIAL COMMAND ATTN: AMCCN

U S ARMY MATERIAL TECHNOLOGY LABORATORY ATTN: DRXMR-HH

U S ARMY STRATEGIC DEFENSE CMD ATTN: DASD-DP

U S ARMY STRATEGIC DEFENSE COMMAND ATTN: ATC-D (WATTS)

DEPARTMENT OF THE NAVY

NAVAL RESEARCH LABORATORY ATTN: CODE 2627 (TECH LIB) ATTN: CODE 4040 D BOOK

NAVAL SEA SYSTEMS COMMAND ATTN: SEA-0351

NAVAL SURFACE WEAPONS CENTER ATTN: CODE K82 ATTN: CODE R44 H GLAZ

OFC OF THE DEPUTY CHIEF OF NAVAL OPS ATTN: OP 654(STRAT EVAL & ANAL BR)

STRATEGIC SYSTEMS PROGRAM OFFICE (PM-1) ATTN: SP-272

DEPARTMENT OF THE AIR FORCE

AIR FORCE SYSTEMS COMMAND ATTN: DLW

AIR FORCE WEAPONS LABORATORY, NTAAB ATTN: NTED J RENICK ATTN: NTED LT KITCH ATTN: NTED R HENNY ATTN: NTEDA ATTN: NTES ATTN: SUL

AIR FORCE WRIGHT AERONAUTICAL LAB ATTN: FIBC ATTN: FIMG

AIR FORCE WRIGHT AERONAUTICAL LAB ATTN: AFWAL/MLP ATTN: AFWAL/MLTM

AIR UNIVERSITY LIBRARY ATTN: AUL-LSE

BALLISTIC MISSILE OFFICE/DAA ATTN: CAPT T KING (MGEN) ATTN: CC/MAJ GEN CASEY ATTN: ENSR

DEPUTY CHIEF OF STAFF/AF-RDQM ATTN: AF/RDQI

DEPUTY CHIEF OF STAFF/AFRDS ATTN: AFRDS (SPACE SYS & C3 DIR)

DNA-TR-86-309 (DL CONTINUED)

STRATEGIC AIR COMMAND/NRI-STINFO
ATTN: NRI/STINFO

STRATEGIC AIR COMMAND/XPQ
ATTN: XPQ

161 ARG ARIZONA ANG
ATTN: LTCOL SHERER

DEPARTMENT OF ENERGY

LAWRENCE LIVERMORE NATIONAL LAB
ATTN: D BURTON
ATTN: L-10 J CAROTHERS
ATTN: L-122 G GOUDREAU
ATTN: L-122 S SACKETT
ATTN: L-203 T BUTKOVICH
ATTN: L-22 D CLARK
ATTN: L-8 P CHRZANOWSKI
ATTN: L-84 H KRUGER

LOS ALAMOS NATIONAL LABORATORY
ATTN: A112 MS R SELDEN
ATTN: M T SANDFORD
ATTN: R WHITAKER

SANDIA NATIONAL LABORATORIES
ATTN: D J RIGALI 1650
ATTN: ORG 7112 A CHABAI
ATTN: R G CLEM 1600

OTHER GOVERNMENT

CENTRAL INTELLIGENCE AGENCY
ATTN: OSWR/NED

DEPARTMENT OF THE INTERIOR
ATTN: D RODDY

DEPARTMENT OF DEFENSE CONTRACTORS

ACUREX CORP
ATTN: C WOLF

AEROSPACE CORP
ATTN: H MIRELS

APPLIED RESEARCH ASSOCIATES, INC
ATTN: N HIGGINS

APPLIED RESEARCH ASSOCIATES, INC
ATTN: S BLOUIN

APPLIED RESEARCH ASSOCIATES, INC
ATTN: D PIEPENBURG

CALIFORNIA RESEARCH & TECHNOLOGY, INC
ATTN: K KREYENHAGEN
ATTN: M ROSENBLATT

CALIFORNIA RESEARCH & TECHNOLOGY, INC
ATTN: F SAUER

H-TECH LABS, INC
ATTN: B HARTENBAUM

INFORMATION SCIENCE, INC
ATTN: W DUDZIAK

KAMAN SCIENCES CORP
ATTN: L MENTE
ATTN: R RUETENIK
ATTN: W LEE

KAMAN TEMPO
ATTN: DASIAC

KAMAN TEMPO
ATTN: DASIAC

MAXWELL LABORATORIES, INC
ATTN: J MURPHY

MERRITT CASES, INC
ATTN: J MERRITT

PACIFIC-SIERRA RESEARCH CORP
ATTN: H BRODE, CHAIRMAN SAGE

R & D ASSOCIATES
ATTN: A KUHL
ATTN: C K B LEE
ATTN: J LEWIS
ATTN: P RAUSCH

R & D ASSOCIATES
ATTN: P MOSTELLER

S-CUBED
ATTN: A WILSON

S-CUBED
ATTN: C NEEDHAM

SCIENCE APPLICATIONS INTL CORP
ATTN: H WILSON

SCIENCE APPLICATIONS INTL CORP
ATTN: J COCKAYNE
ATTN: W LAYSON

SCIENCE APPLICATIONS INTL CORP
ATTN: A MARTELUCCI

SCIENCE APPLICATIONS INTL CORP
ATTN: G BINNINGER

SRI INTERNATIONAL
2 CYS ATTN: A BURNS

DNA-TR-86-309 (DL CONTINUED)

TEXTRON, INC
ATTN: C TILYOU

TRW ELECTRONICS & DEFENSE SECTOR
ATTN: G HULCHER

WEIDLINGER ASSOC. CONSULTING ENGRG
ATTN: P WEIDLINGER

END

8-87

DTIC